

**Study of hadronic and electromagnetic  
decays of giant resonances in  $^{12}\text{C}$  using  
 $(p,p'\gamma)$  reaction**



**Reen Mandeep Singh**

Graduate School of Natural Science and Technology  
Okayama University

This dissertation is submitted for the degree of  
*Doctor of Philosophy in Science*



## Abstract

A nucleus can be excited using different probes ranging from photons to electrons and protons and from light nuclei (e.g.,  $\alpha$  particles) to heavy nuclei with each probe emphasizing on the different aspects of nuclear excitation. For excitation up to few MeVs, nucleus responds via simple single particle-hole excitations, but broad resonances appear for energy range between 10 to 30 MeV. These resonances also known as giant resonances characterize the propagation of collective modes of a nuclear system. Many such resonances have been identified since the discovery of first giant dipole resonance in 1947, which was excited by the photo-nuclear reaction. In the present work, we study the structure and decay of the giant resonances in  $^{12}\text{C}$ , which is a typical light nucleus and is even applied in neutrino physics.

This specific isotope ( $^{12}\text{C}$ ) was chosen because it has been used as a target material in the form of organic liquid scintillator in many large-scale neutrino experiments with the application of detection of neutrinos from a core-collapse supernova explosion in our galaxy. The main reaction for the neutrino detection is the charged-current (CC) anti-neutrino reaction with a proton ( $\bar{\nu}_e + p \rightarrow e^+ + n$ ), also known as inverse  $\beta$ -decay reaction (IBD). The special interest is in the neutral-current (NC) neutrino or anti-neutrino inelastic scattering with  $^{12}\text{C}$ , followed by the emission of  $\gamma$  rays which can be observed in the detector. It is of a special interest since the cross section is significant enough to be detected and is independent of the neutrino oscillations. The NC interactions can excite  $^{12}\text{C}$  to its giant resonances, which can further decay via two modes:

1. Hadronic decay:  $^{12}\text{C}^*$  decays to either ground state or excited states of daughter nuclei ( $^{11}\text{B}$ ,  $^{11}\text{C}$ , etc.) by nucleon emission ( $p, n$ , etc.). If these excited states are below the particle emission threshold in  $^{11}\text{B}$  ( $S_p = 11.2$  MeV) or  $^{11}\text{C}$  ( $S_p = 8.7$  MeV), they decay by  $\gamma$ -ray emissions. No  $\gamma$ -ray emissions with  $E_\gamma > 11$  MeV are possible for this decay mode.
2. Electromagnetic decay:  $^{12}\text{C}^*$  can also decay directly to its ground state with high energy  $\gamma$ -ray emissions with  $E_\gamma > 16$  MeV.

Although the electromagnetic decay width is much smaller than the hadronic decay width ( $\Gamma_{Em}/\Gamma_{Had} \approx \alpha = 1/137$ ), these decays are highly selective and can be used as a powerful

tool to study and discriminate the multi-polarities of giant resonances. Hence, the study of both decay modes is important.

However, there has been no comprehensive study based on experimental measurements for these decay mechanisms. Therefore, we proposed an experiment to measure the  $\gamma$  rays from the giant resonance regions in  $^{12}\text{C}$ . The experiment (E398) to measure the  $\gamma$  rays emitted from giant resonances in  $^{12}\text{C}$  was carried out at Research Center for Nuclear Physics (RCNP), Osaka University using an unpolarized proton beam at 392 MeV. The scattered protons were measured around  $0^\circ$  and were analyzed by the high-resolution magnetic spectrometer Grand Raiden (GR). An array of  $\gamma$ -ray detector consisting of  $5 \times 5 = 25$  NaI detectors ( $2'' \times 2'' \times 6''$  each) was placed at  $\theta_\gamma = 90^\circ$  to detect the  $\gamma$ -rays in coincidence with the scattered protons. Before the beam time, the pulse-height linearity of the  $\gamma$ -ray detectors was checked using different  $\gamma$ -ray sources with  $E_\gamma$  ranging from 0.67 to 33.3 MeV. Furthermore, the calibration of  $\gamma$ -ray detectors and the validation of  $\gamma$ -ray response functions were achieved using in-situ  $\gamma$  rays from  $^{12}\text{C}^*$  (15.11 MeV,  $1^+$ ,  $T = 1$ ) and  $^{16}\text{O}^*$  (6.9 MeV,  $2^+$ ,  $T = 0$ ) states within 5% uncertainty. We have also measured the differential cross section ( $\sigma_{p,p'} = d^2\sigma/d\Omega dE_x$ ) for  $^{12}\text{C}(p,p')$  reaction at 392 MeV and  $0^\circ$  for the energy range  $E_x = 7$ -32 MeV.

The decay of giant resonances in  $^{12}\text{C}$  was studied comprehensively over the entire energy range covering the giant resonances ( $E_x = 16$ -32 MeV) and the results are concluded as follows:

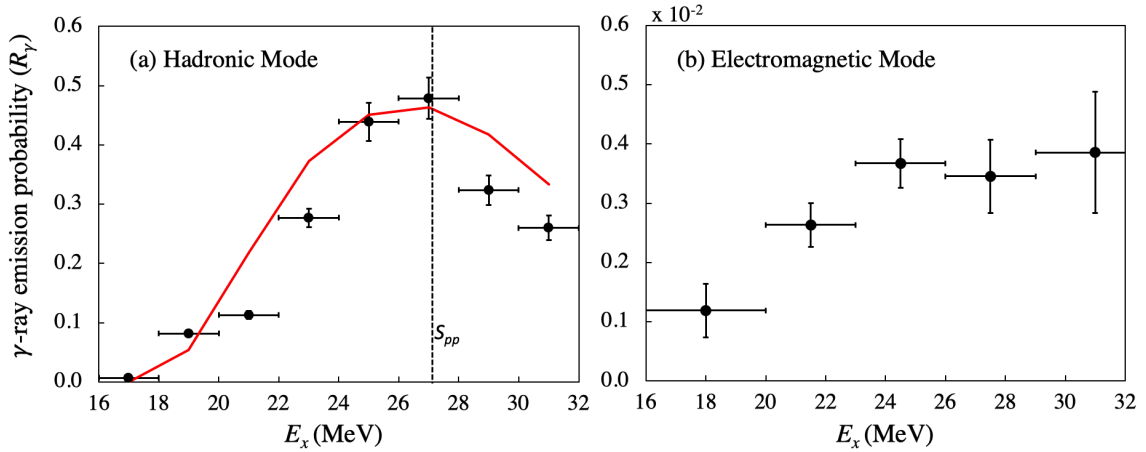


Fig. 1 The  $\gamma$ -ray emission probability ( $R_\gamma$ ) as a function of  $E_x$  for (a) Hadronic decay mode (b) Electromagnetic decay mode of giant resonances in  $^{12}\text{C}$ . The statistical decay model calculations are also shown (red curve).

1. The  $\gamma$ -ray energy spectra and  $\gamma$ -ray emission probability ( $R_\gamma(E_x) = \sigma_{p,p'\gamma}/\sigma_{p,p'}$ ) was measured for the first time as a function of excitation energy for the energy range  $E_x = 16$ -32 MeV.

2. The  $\gamma$ -ray spectra ( $E_\gamma < 11$  MeV) clearly show that the  $\gamma$  rays are emitted from the excited states of daughter nuclei after the particle emission. This is the first observation of  $\gamma$  rays from the hadronic decays of giant resonances in  $^{12}\text{C}$ .
3. It was found that the measured value of ( $R_\gamma(E_x)$ ) for hadronic decay mode starts from zero at  $E_x = 16$  MeV (the threshold for  $p + ^{11}\text{B}$  decay) and increases to  $47.9 \pm 0.5 \pm 3.5\%$  at  $E_x = 27$  MeV and then decreases.
4. The measurements were also compared with the statistical model calculation and smaller  $\gamma$ -ray emission probability by 30-40% was observed than predicted by the calculation.
5. From electromagnetic decay mode ( $16 < E_\gamma < 32$  MeV),  $R_\gamma(E_x)$  increases with excitation energy and reaches the maximum value of  $(0.37 \pm 0.04 \pm 0.04) \times 10^{-2}$  at  $E_x = 24$  MeV. This is the first measurement of  $\gamma$ -ray emission probability from the electromagnetic decays of the giant resonances in  $^{12}\text{C}$ .
6. The trend observed can be explained by  $E1$  transition calculation done using photo-nuclear absorption cross section of  $^{12}\text{C}$ .
7. Using the measured value of ( $R_\gamma(E_x)$ ), the expected number of NC events at large-scale scintillator-based detectors (e.g. JUNO) from the core-collapse supernova were also calculated (Table 5.3).

Reaction	Present work				Laha <i>et al</i> (MB) .
	MB	FD	NK1	NK2	(JUNO collab.)
$p(\bar{\nu}_e, e^+)n$	4933	5378	2194	1974	4857
$^{12}\text{C}(\nu, \nu')^{12}\text{C}^*(15.1 \text{ MeV})$	382	426	169	161	398
$^{12}\text{C}(\nu, \nu')^{12}\text{C}^*(E_x > 16 \text{ MeV})$	144	180	21	20	-

Table 1 Expected number of neutrino events from a core-collapse supernova at 10 kpc to be detected at JUNO(20 kton).

Although the main focus of this thesis is to study the decay of giant resonances, I also estimated the efficiency of the germanium spectrometer of the Accurate Neutron-Nucleus Reaction Measurement Instrument (ANNRI) at the Material and Life Science Experimental Facility (MLF) of the Japan Proton Accelerator Research Complex (J-PARC) at early stage of my Ph.D. The fourteen Ge detectors measure  $\gamma$  rays from the Gd target ( $\text{Gd}_2\text{O}_3$  powder), which is a scattered source. Hence, it was necessary to determine the effect of the target position on the efficiency of each detector. I studied this effect using the  $\gamma$  ray measurements

taken with  $^{22}\text{Na}$  and  $^{60}\text{Co}$  at different target positions and optimized the corresponding parameters in our Monte Carlo. These contributions were fundamental for further analysis and building of the ANNRI-Gd model ( $\text{Gd}(n, \gamma)$  reaction). The results were published in the PTEP journal.

# Table of contents

<b>List of figures</b>	<b>ix</b>
<b>List of tables</b>	<b>xv</b>
<b>1 Introduction</b>	<b>1</b>
1.1 Giant Resonances . . . . .	1
1.1.1 Sum Rule . . . . .	4
1.1.2 Photo-nuclear absorption for $^{12}\text{C}$ . . . . .	6
1.2 Neutrinos from core-collapse Supernova . . . . .	8
1.3 Why Carbon? . . . . .	10
1.4 Decay of Giant resonances . . . . .	11
1.5 Statistical decay model . . . . .	13
1.5.1 Transmission Coefficient . . . . .	13
1.6 Electromagnetic Decays . . . . .	15
1.7 Objectives . . . . .	17
<b>2 Experiment</b>	<b>19</b>
2.1 Beam and target . . . . .	19
2.2 Magnetic Spectrometer . . . . .	20
2.3 $\gamma$ -ray detector . . . . .	24
2.3.1 Detector performance: Off beam . . . . .	25
2.3.2 NewSUBARU: Experiment . . . . .	27
2.4 Trigger and data acquisition system . . . . .	28
2.5 $\gamma$ -ray background subtraction . . . . .	30
2.6 On Beam: Calibration . . . . .	31
<b>3 Analysis and Results</b>	<b>33</b>
3.1 Magnetic Spectrometer Analysis . . . . .	33
3.2 $\gamma$ -ray Analysis . . . . .	35

---

3.3	$\gamma$ rays from the giant resonances . . . . .	38
3.3.1	Hadronic Decays . . . . .	39
3.3.2	Electromagnetic Decays . . . . .	40
<b>4</b>	<b>Discussion</b>	<b>45</b>
4.1	Structure of giant resonances . . . . .	45
4.1.1	DWBA calculations . . . . .	54
4.2	$\gamma$ rays from the giant resonances . . . . .	55
4.2.1	Hadronic Decays . . . . .	55
4.2.2	Statistical model calculations . . . . .	63
4.2.3	Electromagnetic Decays . . . . .	65
4.2.4	$E1$ transition calculation . . . . .	67
<b>5</b>	<b>Estimation of supernova neutrinos</b>	<b>71</b>
5.1	Supernova Neutrino Spectra . . . . .	72
5.2	Inelastic scattering cross section and events estimation . . . . .	73
<b>6</b>	<b>ANNRI Analysis</b>	<b>77</b>
6.1	Efficiency estimation . . . . .	77
<b>7</b>	<b>Summary and Conclusion</b>	<b>81</b>
	<b>References</b>	<b>85</b>

# List of figures

1	The $\gamma$ -ray emission probability ( $R_\gamma$ ) as a function of $E_x$ for (a) Hadronic decay mode (b) Electromagnetic decay mode of giant resonances in $^{12}\text{C}$ . The statistical decay model calculations are also shown (red curve). . . . .	iv
1.1	Response of the nucleus as a function of excitation energy. . . . .	2
1.2	Classification of giant resonances for dipole ( $\Delta L = 1$ ) excitations. . . . .	2
1.3	Schematic representation of multipole transitions between the shell model states. . . . .	3
1.4	Photo-nuclear cross section for $^{12}\text{C}$ . . . . .	7
1.5	Schematic view of KamLAND detector. . . . .	10
1.6	Schematic representation of electric multipole transitions between the shell model states. . . . .	12
1.7	Transmission coefficient as a function of angular momentum from CASCADE and other calculations. . . . .	14
1.8	The ground state $\gamma$ widths of sharp state fully exhausting the appropriate energy weighted sum rule as a function of the excitation energy of the state, relative to the E1 width. . . . .	16
2.1	An overview of the RCNP facility. The experiment was performed in the WS experimental hall, where the Grand Raiden spectrometer is located. . .	20
2.2	Target ladder system (left) and scattering chamber (right). . . . .	21
2.3	Magnetic spectrometer "Grand Raiden" [1]. . . . .	22
2.4	Focal plane detectors of Grand Raiden. . . . .	23
2.5	Wire configuration (up) and structure (down) of MWDC [1]. . . . .	23
2.6	An array of $\gamma$ -ray detector (left) and a NaI(Tl) scintillation counter (right). .	24
2.7	The energy spectra taken by radioactive sources. SE (DE) denotes single (double) escape peak. . . . .	25
2.8	Energy resolution and pulse height response of a NaI counter. . . . .	26

2.9	The measured energy spectra (black) and normalized response function (red). Data/MC shown in the figures is the number of events from the data divided by that from the normalized response function with energy higher than 0.3 MeV for $^{137}\text{Cs}$ and 0.5 MeV for $^{60}\text{Co}$ . . . . .	27
2.10	Experimental setup at NewSUBARU facility. . . . .	28
2.11	NaI(Tl) detector (same used for E398 experiment) used for measuring 33 MeV $\gamma$ -rays at NewSUBARU facility. . . . .	28
2.12	Circuit diagram of the plastic scintillators. . . . .	29
2.13	Circuit diagram of PS Trigger and NaI Trigger. . . . .	29
2.14	Timing chart of signals. . . . .	30
2.15	(a) Time difference between $\gamma$ trigger and PS trigger. (b) $\gamma$ -ray energy spectrum (red) and background spectrum (blue) for 15.11 MeV state ( $1^+$ , $T=1$ ) of $^{12}\text{C}$ . . . . .	31
2.16	(a) In-situ $\gamma$ rays used for calibration of energy response. . . . .	31
3.1	Double differential cross section of the $^{12}\text{C}(p,p')$ reaction at $E_p = 392$ MeV and $\theta = 0^\circ$ . . . . .	33
3.2	(a) Differential cross section of the $^{12}\text{C}(p,p')$ reaction as a function of scattering angle (black data points) and comparison with previous experiment [2] (red data points). Solid and dashed lines are the DWBA calculation results for the transitions to 15.1 MeV state (see text for details). (b) Differential cross section for $^{16}\text{O}(p,p')$ reaction as a function of scattering angle and comparison with previous experiment [3]. . . . .	35
3.3	Geometrical set up in the MC simulation depicting various components and materials (Blue = NaI). . . . .	36
3.4	Cascade $\gamma$ rays from 15.1 MeV state of $^{12}\text{C}$ . . . . .	37
3.5	Measured $\gamma$ -ray spectrum (black) after background subtraction and response function (red line) for the (a) 15.11 MeV state ( $J^\pi = 1^+$ ) of $^{12}\text{C}$ (b) 6.9 MeV state ( $J^\pi = 2^+$ ) of $^{16}\text{O}$ (see text for details). . . . .	38
3.6	Two-dimensional histogram with $E_x$ at y axis and $E$ (deposited $\gamma$ -ray energy) at x axis. . . . .	39
3.7	$\gamma$ -ray energy spectrum (black) and background energy spectrum (red) from hadronic decays at various excitation energies in the giant resonance region of $^{12}\text{C}$ . . . . .	41
3.8	$\gamma$ -ray energy spectrum (blue) and background energy spectrum for the giant resonance energy region ( $E_x > 16$ MeV) of $^{12}\text{C}$ . . . . .	42
3.9	$E_x - E$ spectrum (blue) for for 15.1 MeV after background subtraction. . . .	42

3.10	$E_x - E$ spectrum (blue) and background spectrum (red) for the giant resonance energy region of $^{12}\text{C}$ with $E > 11$ MeV. . . . .	43
3.11	$E_x - E$ spectra (blue) for different $E_x$ regions with background spectra (red line). . . . .	44
4.1	(a) Spin flip component $\Sigma \cdot d^2\sigma/d\Omega dE_x$ (shaded region) compared with $d^2\sigma/d\Omega dE_x$ (black line). The spin flip cross section for $^{12}\text{C}(p,n)^{12}\text{N}$ reaction (blue data points) and the contribution of quasifree process (green curve) to the spin flip cross section obtained from Ref. [4]. The sum of $^{12}\text{C}(p,n)^{12}\text{N}$ spin flip cross section and quasifree contribution is shown by red data points. (b) Non spin flip component $(1 - \Sigma) \cdot d^2\sigma/d\Omega dE_x$ (shaded region) compared with $d^2\sigma/d\Omega dE_x$ (black line). The calculation of Coulomb excitation using the $^{12}\text{C}(\gamma, total)$ photo-absorption cross section (red points). The bin width is 0.2 MeV. . . . .	46
4.2	Energy dependence of the effective nucleon-nucleon interaction for vanishing momentum transfer $q \rightarrow 0$ [5, 6]. . . . .	47
4.3	(a) The comparison of non-spin flip cross section for $^{58}\text{Ni}(p, p')$ (blue) with the calculation of Coulomb excitation using $^{58}\text{Ni}(\gamma, total)$ cross section. . . . .	48
4.4	Double differential cross section for the giant resonance region in $^{12}\text{C}$ fitted with various resonances [7] and a quasifree continuum (green dotted curve). The red curve shows the overall fit obtained from the sum of all contributions. . . . .	50
4.5	Differential cross section as a function of scattering angle at various excitation energies in the giant resonance region of $^{12}\text{C}$ . Dotted and solid black lines show the result of DWBA calculations (see text). (a) A data point (red) from another experiment [8] is also shown. . . . .	53
4.6	The $\gamma$ -ray spectrum (black data points), background spectrum (light blue line), total fit (red line), and $\gamma$ rays from the excited states of daughter nuclei (colored dotted lines) are shown for various $E_x$ regions. . . . .	60
4.7	The total $\gamma$ -ray emission probability ( $R_\gamma$ ) as a function of $E_x$ with systematic errors. . . . .	62
4.8	$\gamma$ -ray emission probability as a function of scattering angle at various excitation energies in the giant resonance region of $^{12}\text{C}$ . . . . .	63

4.9	Comparison between the measured $\gamma$ -ray emission probability (data points) and the statistical model prediction (black dashed line). The red dashed line shows the $\gamma$ -ray emission probability obtained from the fit using Eq. (4.12). The $\gamma$ -ray emission probability from quasifree process (blue line) is also shown. The quantity $S_{pp}$ represents two proton emission threshold (27.2 MeV) for $^{12}\text{C}$ . . . . .	64
4.10	Comparison between the measured ratio ( $\sigma_{^{11}\text{C}(1^{\text{st}})}/\sigma_{^{11}\text{C}(\text{g.s.})}$ ) (black data points) and calculated ratio ( $\tilde{c}_{^{11}\text{C}(1^{\text{st}})}/\tilde{c}_{^{11}\text{C}(\text{g.s.})}$ ) (red line). . . . .	65
4.11	$E_x - E$ spectrum (black) after background subtraction and scaled $E_x - E$ response (red) simulated for the giant resonance energy region of $^{12}\text{C}$ with $E > 11$ MeV . . . . .	66
4.12	Direct $\gamma$ -ray emission probability from the giant resonances of $^{12}\text{C}$ . . . . .	67
4.13	Comparison with $E1$ transition calculations (scaled). . . . .	68
4.14	Direct $\gamma$ -ray emission probability from the giant resonances of $^{12}\text{C}$ and $^{208}\text{Pb}$ and comparison with $E1$ transition calculations (normalized with $^{12}\text{C}$ ). . . . .	69
5.1	(a) Supernova neutrino spectrum folded by Fermi-Dirac and Maxwell-Boltzmann distribution at $T=8$ MeV. (b) Supernova neutrino spectrum obtained using Nakazato et. al. for different neutrino species. . . . .	71
5.2	The inelastic cross sections as a function of excitation energy at $E_\nu = 50$ MeV for (a) $^{12}\text{C}(\nu, \nu')^{12}\text{C}^*(1^-)$ reaction (b) $^{12}\text{C}(\nu, \nu')^{12}\text{C}^*(2^-)$ reaction . . . . .	73
5.3	The inelastic cross section for the $^{12}\text{C}(\nu, \nu')^{12}\text{C}^*(15.1 \text{ MeV}, 1^+, T = 1)$ reaction as function of neutrino energy ( $E_\nu$ ). . . . .	74
5.4	The inelastic cross section for the $^{12}\text{C}(\nu, \nu')^{12}\text{C}^*(E_x > 16 \text{ MeV})$ reaction as function of neutrino energy ( $E_\nu$ ). . . . .	74
6.1	Energy spectra observed by peripheral crystal 6 of the upper cluster in our data (black) and our MC (red) for the calibration sources $^{60}\text{Co}$ (left) and $^{137}\text{Cs}$ (right). . . . .	78
6.2	Energy spectra observed by crystal 6 in the background measurement with an empty target holder (red) and the measurement with the enriched $^{157}\text{Gd}$ sample (black; before background subtraction). The background spectrum was scaled to match the dead-time-corrected live time of the gadolinium measurement. . . . .	79

- 6.3 Ratios of the single photopeak efficiencies from data to single photopeak efficiencies from MC averaged over the 14 crystals at the fixed  $\gamma$ -ray energies (left) and averaged over the 11 data points for the single crystals (right). Linear interpolation between the points from the simulation was used to determine the MC efficiency at intermediate energy. The calculations of the weighted mean values and the weighted sample standard deviations (error bars) take the errors of the data points into account. Outer error bars indicate the extreme values of the ratios in the respective samples. The  $^{35}\text{Cl}(n, \gamma)$  data point at 7414 keV is the reference for the normalization of the other data points of this reaction. It perfectly agrees with a ratio of one since it was normalized with the MC simulation. . . . . 80



# List of tables

1	Expected number of neutrino events from a core-collapse supernova at 10 kpc to be detected at JUNO(20 kton). . . . .	v
1.1	Statistical model calculations for $^{12}\text{C}$ at $E_x = 22$ MeV, $J^\pi = 1^-$ and $T = 1$ . The quantities $T$ and $t_i$ are the total total transmission coefficient and the individual transmission coefficients, respectively. . . . .	15
2.1	Specification of GR . . . . .	21
2.2	Radioactive sources used for the detector performance check. . . . .	24
2.3	Different $\gamma$ ray energies obtained from inverse scattering of different laser photons. . . . .	29
3.1	The number of excitation events for different energy regions and the systematic uncertainty in their estimation. . . . .	34
3.2	Systematic uncertainties in the measurement of differential cross section. . . . .	34
4.1	Contribution from different components to the total cross section of $E_x = 16-32$ MeV . . . . .	48
4.2	Resonance energy ( $E_m$ ), resonance width ( $\Gamma_m$ ), spin-parity, and isospin obtained from Ref. [7], and $\sigma_m$ obtained from fit. * $E_m$ and $\Gamma_m$ were obtained from [9, 10]. **Spin-parity and isospin were obtained from Ref. [11, 2]. . . . .	51
4.3	Optical model parameters used in DWBA calculations taken from Ref. [8]. . . . .	52
4.4	Transition matrix elements used in DWBA calculations. The superscript (a) denotes transition matrix elements from Cohen and Kurath [8] and (b) denotes matrix elements obtained from SFO Hamiltonian [12, 13]. The amplitude for the component $l_i l_j$ represents an excitation from the $l_j$ hole state to the $l_i$ particle state. The subscripts on the single-particle orbitals represent the quantity $2j$ . Here, the $2s_{1/2}$ orbital is designated as $s_1$ . . . . .	52
4.5	$\gamma$ -ray response function from quasifree processes for different excitation energies. . . . .	57

4.6	Energy states of daughter nuclei used for fitting, and cascade $\gamma$ rays emitted from them with their respective emission probabilities (given in parentheses).	59
4.7	The probability ( $r_i$ ) obtained from the fit and the total $\gamma$ -ray emission probability ( $R_\gamma$ ). Numbers in parentheses represent the error in the least significant digit. . . . .	61
4.8	Contributions from the 2-body decay, 3-body decay and quasifree process along with calculated $\gamma$ -ray emission probability. . . . .	64
4.9	$\gamma$ -ray emission probability from the electromagnetic decay mode. . . . .	66
4.10	Mean energy of the $1^-$ giant resonance and integrated total photo-nuclear cross section for $^{12}\text{C}$ and $^{208}\text{Pb}$ . . . . .	68
5.1	Mean energies of the neutrinos from supernova explosion. . . . .	72
5.2	Expected number of neutrino events from a core-collapse supernova at 10 kpc to be detected at KamLAND (1kton). . . . .	75
5.3	Expected number of neutrino events from a core-collapse supernova at 10 kpc to be detected at JUNO(20 kton). . . . .	75

# Chapter 1

## Introduction

### 1.1 Giant Resonances

A nucleus can be excited using different probes ranging from photons to electrons and protons and from light nuclei (e.g.,  $\alpha$  particles) to heavy nuclei with each probe emphasizing on the different aspects of nuclear excitation. For excitation up to few MeVs, nucleus responds via simple single particle-hole excitations but broad resonances appear for energy range between 10 to 30 MeV (Fig. 1.1). These resonances also known as giant resonances characterize the propagation of collective modes of a nuclear system. Many such resonances have been identified since the discovery of first giant dipole resonance in 1947, which was excited by the photo-nuclear reaction.

The different modes of excitation can be classified by considering the effective interactions between the projectile and the target nucleus. The interactions are both spin and isospin dependent. For example, the central part of the interaction between projectile  $p$  and  $i^{th}$  nucleon of the nucleus can be written as

$$V_{ip}(r_{ip}) = V_0^C(r_{ip}) + V_\tau^C(r_{ip})\vec{\tau}_i \cdot \vec{\tau}_p + V_\sigma^C(r_{ip})\vec{\sigma}_i \cdot \vec{\sigma}_p + V_{\sigma\tau}^C(r_{ip})\vec{\sigma}_i \cdot \vec{\sigma}_p \vec{\tau}_i \cdot \vec{\tau}_p. \quad (1.1)$$

Here, the first term describes the isoscalar vibrations in which the protons and neutrons oscillate in phase depending on the multipole pattern defined by  $\Delta L$ . Interactions with isospin operators  $\vec{\tau}_i \cdot \vec{\tau}_p$  induce isospin-flip transitions with  $\Delta T = 1$  in which protons and neutron vibrate out of phase. The third term induces spin-flip transitions ( $\Delta T = 1$ ) in which spin-up and spin-down nucleons vibrate out of phase. The fourth term induces both isospin-flip and spin-flip transitions ( $\Delta T = 1, \Delta S = 1$ ) in which protons with spin-up/down vibrates against neutrons with spin-down/up.

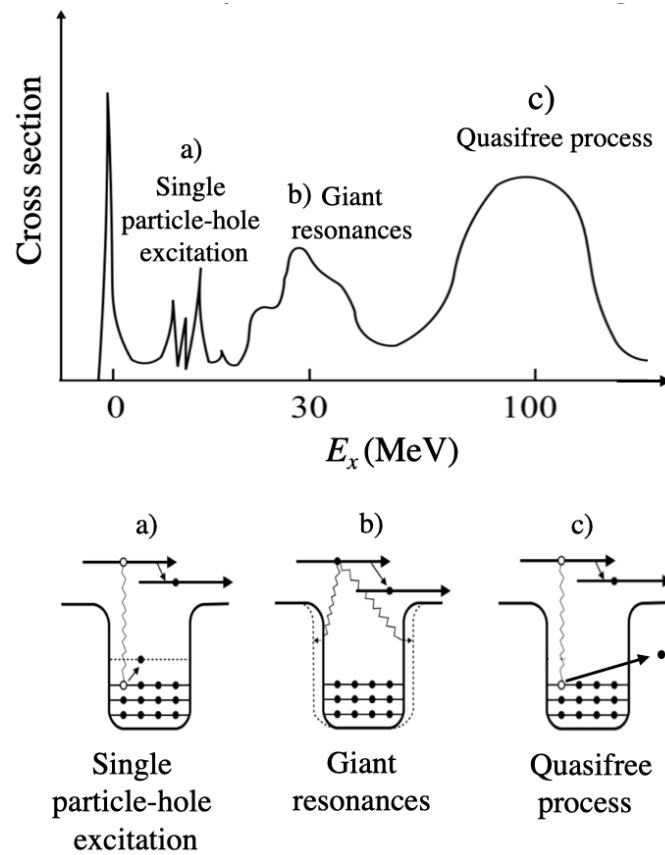


Fig. 1.1 Response of the nucleus as a function of excitation energy.

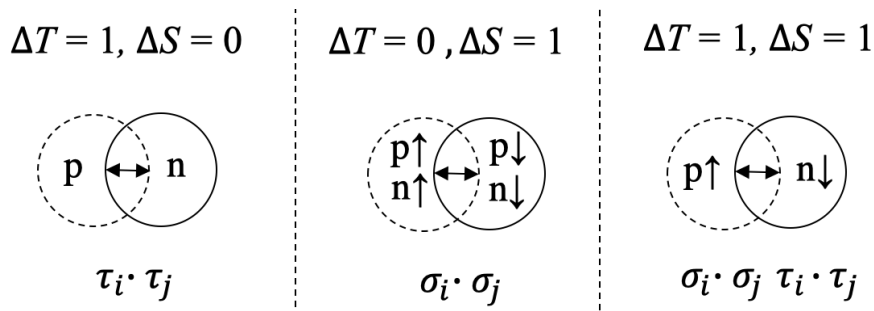


Fig. 1.2 Classification of giant resonances for dipole ( $\Delta L = 1$ ) excitations.

At the microscopic level, giant resonances can be understood qualitatively by considering a schematic shell model picture as shown in Fig. 1.3. These collective vibrations result from the coherent superposition of many such single particle-hole transitions. Major shells are denoted as  $N, N+1$ , etc. and are separated by  $\sim 1\hbar\omega$  or  $\sim 41A^{-1/3}$  MeV. Giant resonances result from the transitions of nucleons to higher major shells under the influence of an

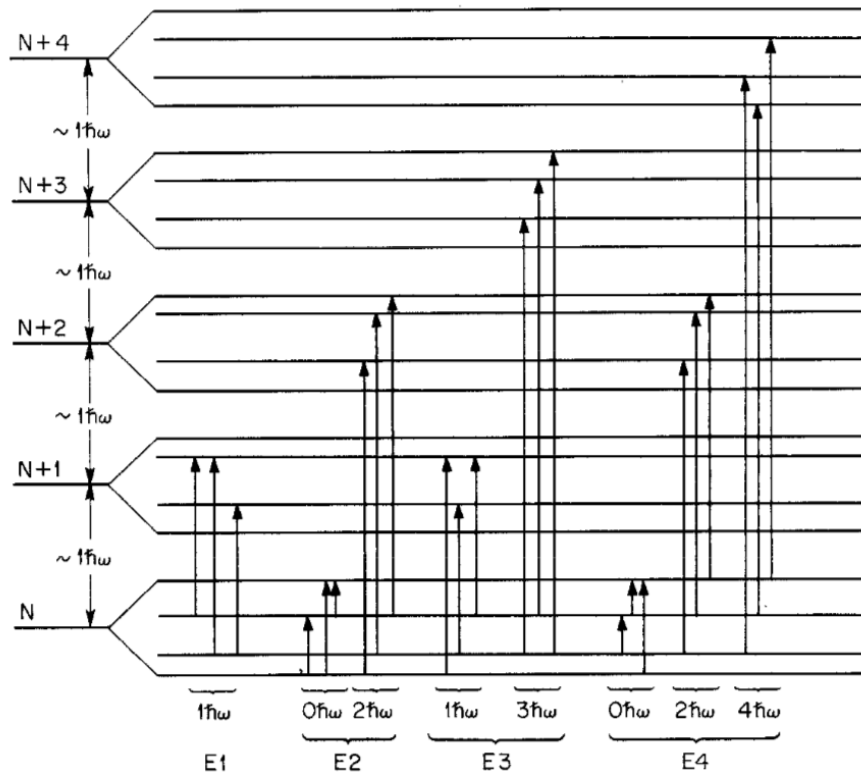


Fig. 1.3 Schematic representation of multipole transitions between the shell model states.

interaction that order these transitions into coherent motion. The interaction excites the nucleus to  $n^{\text{th}}$  major shell obeying the parity conservation.

For example, the isovector giant dipole resonance is built up by superposition of E1 transitions spanning  $1\hbar\omega$  and is expected to be located at an excitation energy of  $41A^{-1/3}$  MeV, however, it is located at  $\sim 77A^{-1/3}$  MeV. This difference arises from the fact that residual particle-hole interaction is attractive for isoscalar and repulsive for isovector excitations [14] which causes isoscalar resonance to move down in energy and isovector resonance to move up in energy relative to the unperturbed energy of  $41A^{-1/3}$  MeV. Similarly, for E2 transitions two different transitions spanning  $0\hbar\omega$  and  $2\hbar\omega$  are allowed with transitions pushed down or up in energy for isoscalar and isovector modes respectively. Various overlapping resonances and their large width (3-5 MeV) highlights the difficulty in studying giant resonances.

This problem can be resolved by using specific probes exciting only the specific modes of giant resonances, the prime example being the excitation of Isovector Giant Dipole Resonance (IVGDR,  $J^\pi = 1^-$ ,  $T = 1$ ) using photo-absorption. This reaction overwhelmingly proceeds by dipole absorption (since E1 transition strength is orders of magnitude stronger than other multipoles), hence exciting the IVGDR. Other probe specifications include inelastic  $\alpha$  scattering at beam energies of 100-250 MeV for studying isoscalar resonances, charge

exchange reactions like (p,n) and ( $^3\text{He,t}$ ) for studying higher multipole isovector resonances, etc.

### 1.1.1 Sum Rule

Giant resonances are so named because a considerable fraction of electric transition strength is localized at certain excitation energy. These transition strengths can also be expressed in terms of theoretical limit for the strength, so-called sum-rule.

The transition strength associated with a moment  $F$  (assumed to be hermitian operator) is equal to the sum of transition probability multiplied by the excitation energy and the sum of the strengths can be given as

$$S(F) = \sum_a (E_a - E_0) |\langle a|F|0\rangle|^2, \quad (1.2)$$

where  $a$  labels the complete set of excited states to which the transitions can be possible by operating  $F$  on the ground state. By exploiting the general commutation relations and using the completeness of the states  $\sum_a |a\rangle\langle a| = 1$ , the sum can also be expressed as

$$\begin{aligned} \sum_a (E_a - E_0) |\langle a|F|0\rangle|^2 &= \sum_a \langle a|F|0\rangle (E_a - E_0) \langle 0|F|a\rangle, \\ &= \frac{1}{2} \sum_a \langle 0|F|a\rangle \{ \langle a|[H, F]|0\rangle - \langle 0|[H, F]|a\rangle \} \langle a|F|0\rangle, \\ &= \frac{1}{2} \langle 0|[F, [H, F]]|0\rangle. \end{aligned} \quad (1.3)$$

where  $H$  is the hamiltonian

$$H = \sum_k \left[ \frac{-\hbar^2 \nabla_k^2}{2M_k} + V(\vec{r}_k) \right]. \quad (1.4)$$

If  $F$  is a hermitian operator depending only on the spatial coordinates

$$F = \sum_k F(\vec{r}_k), \quad (1.5)$$

and if the interactions do not explicitly depend on the momenta of the particles, then Eq. (1.3) becomes

$$S(F) = \frac{1}{2} \left\langle 0 \left| \sum_k \frac{-\hbar^2}{2M_k} [F(\vec{r}_k), [\nabla_k^2, F(\vec{r}_k)]] \right| 0 \right\rangle. \quad (1.6)$$

The commutator can be solved as follows

$$\begin{aligned}
[\nabla^2, F] &= \nabla^2 F - F \nabla^2, \\
&= \nabla(\nabla F + F \nabla) - F \nabla^2, \\
&= \nabla^2 F + \nabla F \nabla + \nabla F \nabla + F \nabla^2 - F \nabla^2, \\
&= \nabla^2 + 2\nabla F \nabla. \\
[F, [\nabla^2, F]] &= F(\nabla^2 F + 2\nabla F \nabla) - (\nabla^2 + 2\nabla F \nabla)F, \\
&= F \nabla^2 F + 2F \nabla F \nabla - (\nabla^2 F + 2\nabla F(\nabla F + F \nabla)), \\
&= -2\nabla F(\nabla F), \\
&= -2(\nabla F)^2.
\end{aligned} \tag{1.7}$$

Finally, the commutator is simply the sum of kinetic energies as shown

$$S(F) = \langle 0 | \sum_k \frac{\hbar^2}{2M_k} (\nabla_k F(\vec{r}_k))^2 | 0 \rangle. \tag{1.8}$$

where  $M_k$  and  $q_k$  is the mass and the charge of the  $k$ th nucleon, respectively. The significance of this energy weighted sum rule lies in the fact that this sum can be represented as an expectation value of a one-body operator and is relatively insensitive to the detailed correlations in the initial state. The electric multipole transition operator for the system of nucleons can be given as

$$\mathcal{M}(E\lambda; \mu) = e \sum_{k=1}^A \left[ \left( \frac{1}{2} - t_z \right) r^\lambda Y_{\lambda\mu} \right]_k. \tag{1.9}$$

Naively one would expect only the protons should appear in the description of electromagnetic transitions, since they alone carry the charge inside the nucleus, however, this is not the case. Lets assume the case of single-particle excitation of neutron. Although it carries no charge, but because the total center of mass must be stationary, the rest of nucleus will move to balance that and produce displacement of charge. Hence, the effect of the recoil of the remainder nucleus upon the single-particle transition must be taken into account. We now express electric dipole transition operator in terms of intrinsic coordinates so that to remove any contribution from c.m. motion by rewriting  $\vec{r}_k = \vec{R} + \vec{r}_k^{int}$ , where  $\vec{R} = \sum_i \vec{r}_i / A$  is the c.m. coordinate. Hence, Eq. (1.9) can be written as

$$\mathcal{M}(E1) = e \sum_{k=1}^A \left( \frac{1}{2} - t_{zk} \right) (\vec{r}_k - \vec{R}). \tag{1.10}$$

For purely isovector dipole transitions, we can write

$$\mathcal{M}(E1) = -e \sum_{k=1}^A t_{zk} (\vec{r}_k - \vec{R}), \quad (1.11)$$

Since,  $t_z = +\frac{1}{2}$  for neutrons and  $t_z = -\frac{1}{2}$  for protons, this can be rewritten as

$$\mathcal{M}(E1) = e \frac{N-Z}{2} \vec{R} - \sum_{k=1}^A t_{zk} \vec{r}_k. \quad (1.12)$$

or using the definition of c.m. coordinate,

$$\begin{aligned} \mathcal{M}(E1; \mu) &= e \sum_{k=1}^A \left( \frac{N-Z}{2A} - t_{zk} \right) \vec{r}_k, \\ &= e \sum_{k=1}^A \left[ \left( \frac{N-Z}{2A} - t_{zk} \right) r Y_{1\mu} \right]_k, \end{aligned}$$

Using the gradient formula [14]

$$\sum_{\mu} \nabla f(r) Y_{\lambda\mu}^*(\hat{r}) \cdot \nabla f(r) Y_{\lambda\mu}(\hat{r}) = \frac{2\lambda+1}{4\pi} \left( \left( \frac{df}{dr} \right)^2 + \lambda(\lambda+1) \left( \frac{f}{r} \right)^2 \right). \quad (1.13)$$

and Eq. (1.8), one can show that

$$\begin{aligned} S(E1) &= \frac{3}{4\pi} \frac{\hbar^2}{2M} 3e^2 \left[ \left( \frac{N-Z}{2A} - \frac{1}{2} \right)^2 N + \left( \frac{N-Z}{2A} + \frac{1}{2} \right)^2 Z \right], \\ &= \frac{9}{4\pi} \frac{\hbar^2}{2M} \frac{NZ}{A} e^2 = 14.8 \frac{NZ}{A} e^2 \text{fm}^2 \text{MeV}. \end{aligned}$$

This is the strength of the state exhausting 100% of  $E1$  energy weighted sum-rule (EWSR). For the case of  $^{12}\text{C}$  EWSR can be given as

$$S(E1)_{^{12}\text{C}} = 14.8 \frac{6 \times 6}{12} = 44.4 e^2 \text{fm}^2 \text{MeV}. \quad (1.14)$$

### 1.1.2 Photo-nuclear absorption for $^{12}\text{C}$

As mentioned earlier, photoabsorption strongly excites IVGDR which is dominated by  $E1$  transitions (since the other multipole transition strengths are orders of magnitude weaker than  $E1$  transition strength). Hence, experimentally, the strength of  $E1$  transitions can be determined by integrating the photo-nuclear absorption cross section over the giant resonance

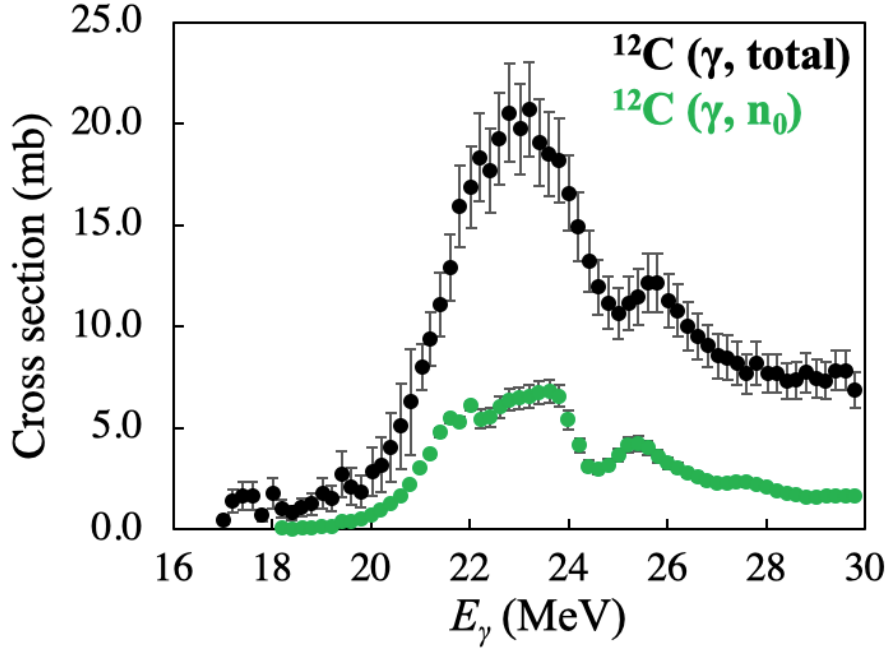


Fig. 1.4 Photo-nuclear cross section for  $^{12}\text{C}$ .

(GR) energy region. The relation between the  $E1$  strength and photo-nuclear absorption cross section can be written as [15, 16]

$$S(E1) = \frac{9}{16\pi^3\alpha} \int_{GR} \sigma dE \quad e^2\text{fm}^2\text{MeV}, \quad (1.15)$$

where  $\alpha$  is fine structure constant. The photo-nuclear cross section for  $^{12}\text{C}$  was obtained from the Ref. [17] and the integrated cross section is

$$\int_{GR} \sigma dE = 116 \text{ MeV} \cdot \text{mb}. \quad (1.16)$$

The total  $E1$  strength exhausted in giant resonance region is

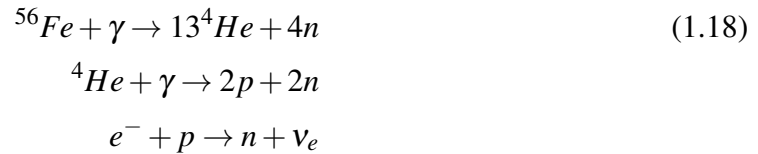
$$S_{E1} = 28.8 \quad e^2\text{fm}^2\text{MeV}. \quad (1.17)$$

which is 64.4% of the total EWSR. It can be stated that a considerable fraction of electric transition strength is localized at certain excitation energy *i.e.* IVGDR energy region, hence the name ‘‘Giant Resonance’’.

## 1.2 Neutrinos from core-collapse Supernova

At the core of a star, fusion of hydrogen into helium releases the energy which heats it up providing outward pressure that supports the star against the gravitational collapse. But at the last stages of stellar evolution, the entire hydrogen is converted into helium and the fusion starts to slow down. The core contracts under the influence of gravity which leads to an increase in temperature that initiates helium fusion and temporarily stabilizes the star against the collapse. Again, when the entire helium is used up, this cycle repeats, from one element to another, with each step producing the heavier element and finally ending at the most stable element  $^{56}\text{Fe}$ . Eventually, the star evolves into an onion like structure with  $^{56}\text{Fe}$  at its core. As the  $^{56}\text{Fe}$  has the highest binding energy per nucleon, no further energy can be produced by the fusion. At this stage, the core is under huge gravitational pressure, as there is no fusion halting the collapse. The star is supported only by the degeneracy pressure of the electrons. When the core mass exceeds the Chandrasekhar limit ( $1.4M_{\odot}$ ), it can no longer support itself by electron degeneracy pressure and begins to collapse.

The collapse produces temperatures high enough to reduce all the preexisting nuclei in the core to  $\alpha$  particles and neutrons via photodisintegration and, subsequently, into constituent nucleons. Simultaneously, electron capture on nuclei also takes place producing neutrons and neutrinos ( $\nu_e$ ). Since neutrinos interact weakly with matter, they escape freely carrying away energy and further accelerating the collapse.



As the core density increases, the mean free path of neutrino becomes shorter. When the mean free path becomes shorter than the core size, the core becomes opaque to the neutrinos and they get trapped forming a neutrinosphere. The main source of opacity during this collapse stage is the coherent scattering off the nuclei  $\nu_e + A \rightarrow \nu_e + A$ . The neutrino trapping increases the fermi pressure of neutrinos and then suppresses the drastic increase in electron capture.

The infalling core is divided into two parts [18, 19], referred as, the inner region which collapses homologously and subsonically and the outer region which collapses supersonically. When the density of the inner core reaches nuclear density, the core restores stability due to repulsive nuclear forces and the collapse of the inner core is decelerated whereas the outer

core is still collapsing at supersonic velocities. The outer core free falls on the stiff inner core and undergoes a bounce generating a shock wave propagating outwards. Furthermore, the shock wave propagates outwards dissociating nuclei into free nucleons and drastically increasing the electron capture. Dissociation of the nuclei eliminates the main source of neutrino opacity leading to the recession of neutrinosphere and neutrinos are emitted copiously, giving rise to initial  $\nu_e$  burst, also known as neutronization burst. The duration of the neutronization burst is the time scale of shock propagation and is about less than 10 ms and the total energy emitted during the burst is only of the order of  $10^{51}$  ergs due to the short duration time.

In the shock traversed region, the matter is hot and relatively less dense. The electron degeneracy is not high and the relativistic protons can also be created thermally and other flavors of neutrinos are also created by electron-positron annihilation as

$$e^- + e^+ \rightarrow \nu + \bar{\nu} \quad (1.19)$$

The shock wave also sweeps off some of the matter of the falling outer core which accretes onto the inner core forming a proto-neutron star. This star consists of a dense core and a mantle that is collapsing. The gravitational energy released from the collapse is carried away as thermal energy by the neutrinos, hence, cooling down the proto-neutron star. All types of neutrinos are emitted in the time scale of 10 s with approximately equal luminosities with the thermal spectrum characterized by the edge of their neutrinosphere. Those flavors of neutrinos which interact the most with the matter decouple at the largest radius ( or the neutrinosphere for that flavor will have the largest radius) and thus have the lowest temperature. The  $\nu_\mu$  and  $\nu_\tau$  neutrinos and their antiparticles (also called  $\nu_x$ ) have only neutral-current interactions with matter, and hence, leave at the highest temperature. The  $\nu_e$  and  $\bar{\nu}_e$  have also charged-current interactions and therefore leave with lower temperatures. Out of them  $\nu_e$  has lower temperature as the matter is neutron-rich and thus  $\nu_e$  interacts more than  $\bar{\nu}_e$ . The energies of the neutrinos show the ordering  $\langle E_{\nu_e} \rangle < \langle E_{\bar{\nu}_e} \rangle < \langle E_{\nu_x} \rangle$ . After about one minute, the neutron star becomes transparent for neutrinos and neutrino luminosity drops suddenly. The energy spectra of these neutrinos is described in detail in Chapter 5.

After about an hour from the core bounce, the wave propagates to the stellar surface blowing off the outer layers and the star actually explodes.

### 1.3 Why Carbon?

This specific isotope was chosen because it has been used as a target material in the form of organic liquid scintillator (LS) in many large-scale neutrino experiments [20, 21] with the application of detection of neutrinos from the core-collapse supernova explosion in our galaxy. The main reaction for the neutrino detection is the charged-current (CC) anti-neutrino reaction with a proton ( $\bar{\nu}_e + p \rightarrow e^+ + n$ ), also known as inverse  $\beta$ -decay reaction (IBD). The special interest is in the neutral-current (NC) neutrino or anti-neutrino inelastic scattering with  $^{12}\text{C}$ , which can excite  $^{12}\text{C}$  to its giant resonances, followed by the emission of  $\gamma$  rays that can be observed in the detector. It is of a special interest since the  $\gamma$ -ray cross section is significant enough to be detected and is independent of the neutrino oscillations.

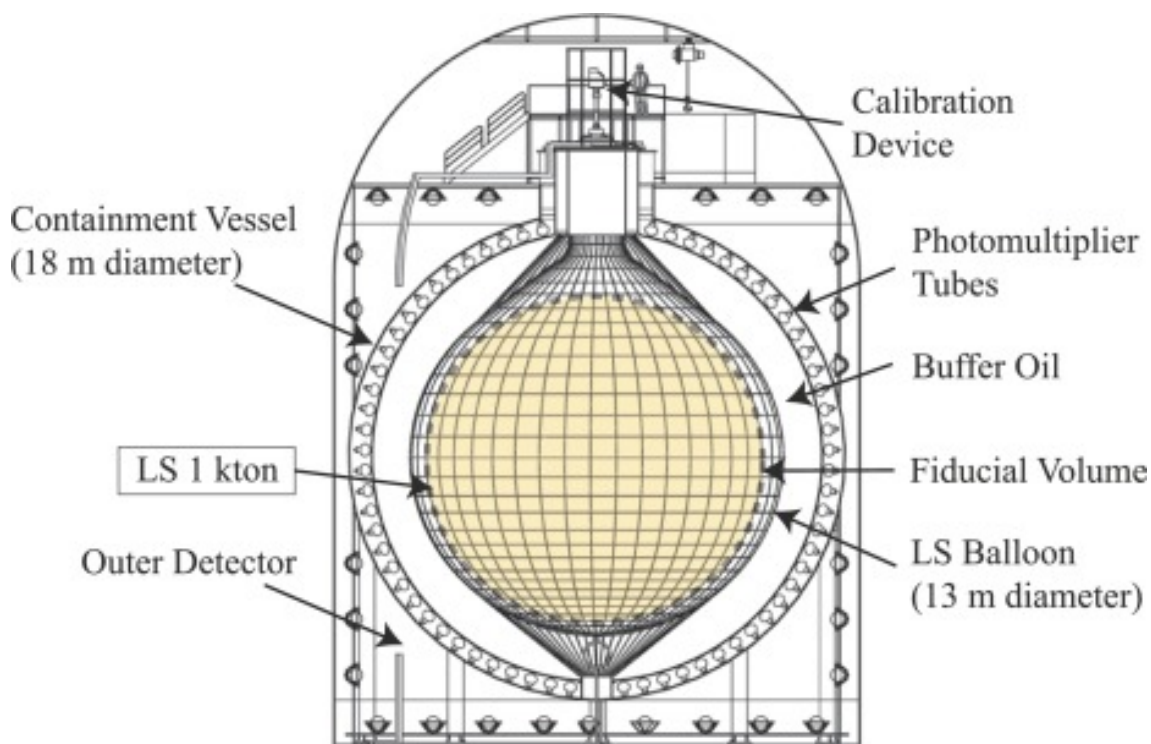


Fig. 1.5 Schematic view of KamLAND detector.

The first observation of  $^{12}\text{C}(\nu, \nu')^{12}\text{C}^*(1^+, 15.11 \text{ MeV}, T=1)$  reaction with 15.11 MeV  $\gamma$  ray which is associated with the electromagnetic decay was carried out by KARMEN experiment [22]. The  $\gamma$ -ray emission probability ( $\Gamma_\gamma/\Gamma$ ) of excitation levels of  $^{12}\text{C}$  below the separation energy ( $S_p=15.96 \text{ MeV}$ ) has been well measured [23]. However, the giant resonances appear above the separation energy and they mainly decay hadronically via particle emission (p, n, d, and  $\alpha$ ) to the daughter nucleus. Although they decay mostly to the ground states of the daughter nucleus, some of them go to excited states of these nuclei,

emitting  $\gamma$  rays. Langanke et al. [24] proposed the above decay mechanism of the giant resonances and estimated the event rate from supernova explosion for water target ( $^{16}\text{O}$ ). They stressed on the importance of measuring NC events since it is more sensitive to  $\nu_\mu$  and  $\nu_\tau$  neutrinos than to  $\nu_e$  neutrinos. However, there are no experimental measurements of  $\gamma$  rays from the excited states of  $^{12}\text{C}$  in the energy region  $E_x=16\sim 32$  MeV.

## 1.4 Decay of Giant resonances

The giant resonances may decay via two modes:

1. Hadronic decay: This decay proceed via strong interactions with a typical decay width ( $\Gamma_{Had}$ ) of few keV to MeV range. In this mode, the excited nucleus ( $^{12}\text{C}^*$ ) decays to either ground state or excited states of daughter nuclei ( $^{11}\text{B}$ ,  $^{11}\text{C}$ , etc.) by nucleon emission ( $p$ ,  $n$ , etc.). If these excited states are below the particle emission threshold in  $^{11}\text{B}$  ( $S_p = 11.2$  MeV) or  $^{11}\text{C}$  ( $S_p = 8.7$  MeV), they decay by  $\gamma$ -ray emissions. No  $\gamma$ -ray emissions with  $E_\gamma > 11$  MeV are possible for this decay mode.
2. Electromagnetic decay: This decay proceeds via electromagnetic interactions with a typical decay width ( $\Gamma_{EM}$ ) of eV to few keV range. In this mode, excited nucleus ( $^{12}\text{C}^*$ ) may decay directly to its ground state with high energy  $\gamma$ -ray emissions ( $11 < E_\gamma < 32$  MeV).

Although the electromagnetic decay width is much smaller than the hadronic decay width ( $\Gamma_{Em}/\Gamma_{Had} \approx \alpha = 1/137$ ), these decays are highly selective and can be used as a powerful tool to study and discriminate the multi-polarities of giant resonances. Hence, the study of both decay modes is important. However, there has been no comprehensive study based on experimental measurements for these decay mechanisms.

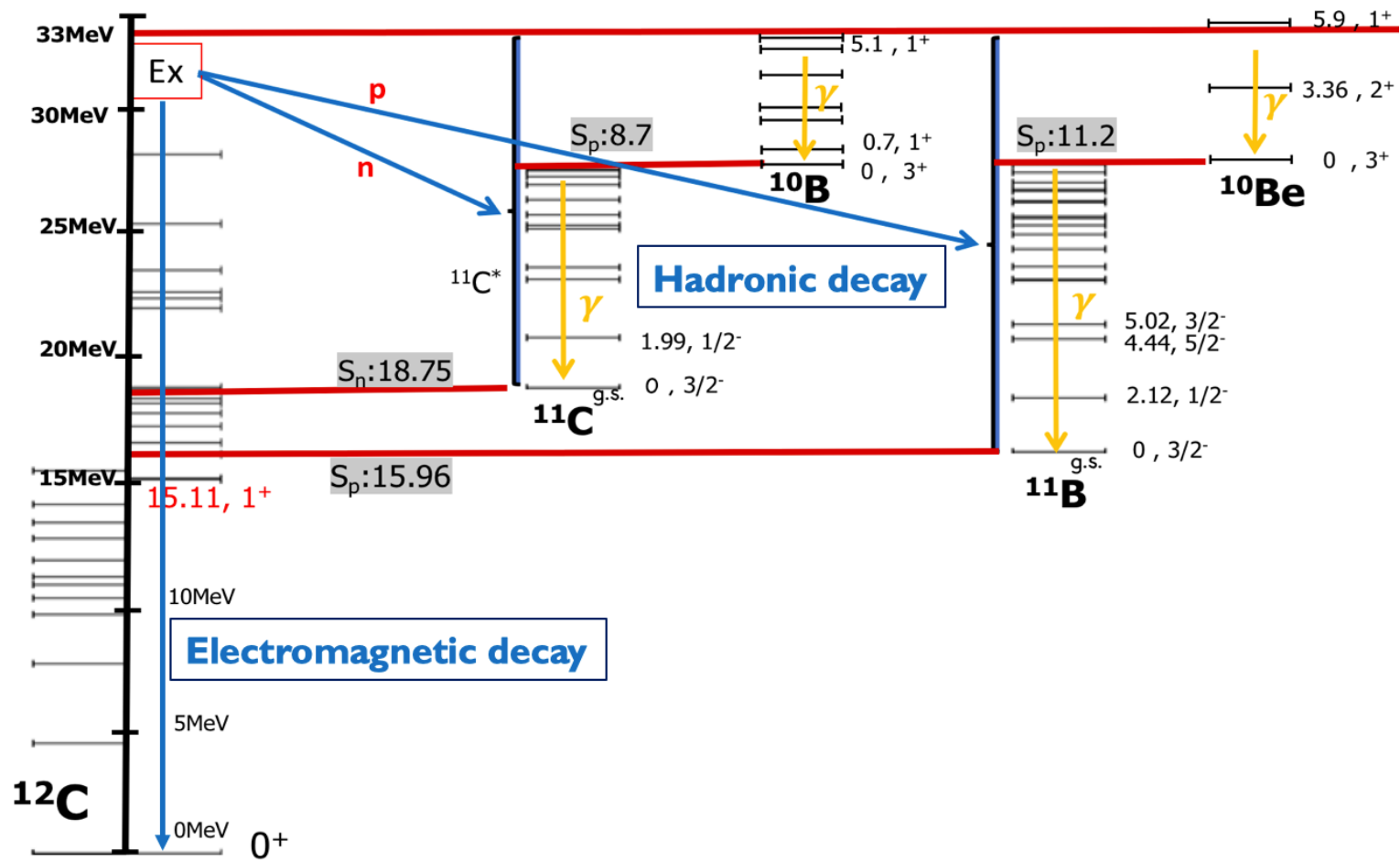


Fig. 1.6 Schematic representation of electric multipole transitions between the shell model states.

## 1.5 Statistical decay model

The hadronic decays can be described using statistical decay model. The model calculation was based on the Hauser-Feshbach formalism [25, 26] and was used to predict the probability for a nucleus excited to its giant resonances to decay to the daughter nuclei via particle emissions. The transmission coefficient from an excited nucleus ( $E_x$ ) to the  $i^{\text{th}}$  energy state of daughter nucleus  $A(E_A^i, J_A^i, \pi_A^i)$  by the emission of particle  $a$  is given by the summation over all quantum mechanically allowed partial waves,

$$T(E_x \rightarrow a + (A, i)) = \sum_{S=|J_A^i - s_a|}^{J_A^i + s_a} \sum_{L=|J_x - S|}^{J_x + S} T_L^a(\epsilon_a), \quad (1.20)$$

where  $T_L^a(\epsilon_a)$  is the individual transmission coefficient of a particle with kinetic energy  $\epsilon_a$  given by  $E_x - E_A^i -$  separation energy, spin  $s_a$ , and orbital angular momentum  $L$ . The summation over  $L$  is restricted by the parity conservation rule  $\pi_x = \pi_a \pi_A^i (-1)^L$ . These individual transmission coefficients are obtained by solving the Schrödinger equation with the optical potential for the particle nucleus interaction.

### 1.5.1 Transmission Coefficient

The radial part of the Schrödinger equation for the relative motion of two particle system can be written as

$$\frac{1}{r^2} \frac{d}{dr} r^2 \frac{d\phi_l}{dr} + [k^2 - l(l+1) - 2 \frac{\mu}{\hbar^2} (V_{opt})] \phi_l = 0, \quad (1.21)$$

where  $l$  is the orbital angular quantum number and  $k$  is the wave number. The transmission coefficient for the  $l^{\text{th}}$  partial wave can be given as

$$T_l = 4k \int \phi_l^* \left( \frac{-2\mu}{\hbar^2} W \right) \phi_l r^2 dr, \quad (1.22)$$

where  $W$  is the imaginary part of the complex optical potential.

The optical model potential are empirically determined by assuming a functional form with various unspecified parameters [25]. These parameters are then determined by the fit to

the experimental data. The commonly used form of optical potential is given as

$$\begin{aligned}
 V_{opt} &= \mathcal{V}_c + \boldsymbol{\sigma} \cdot \mathbf{L} \mathcal{V}_{LS}, \\
 \mathcal{V}_c &\equiv V_{Coul} - V f(x_0) - iW f(x_W), \\
 \mathcal{V}_{LS} &= (V_{LS} - iW_{LS}) \left( \frac{\hbar}{m\pi c} \right)^2 \frac{1}{r} \frac{d}{dr} f(x_{LS}),
 \end{aligned} \tag{1.23}$$

where  $L$  is the angular momentum operator and  $V, W, W_D, V_{LS}$  and  $W_{LS}$  are constants.  $V_{Coul}$  is the Coulomb potential for a uniformly charged sphere of radius  $R_c$  and is given as

$$V_{Coul} = \begin{cases} \frac{zZe^2}{r} & r \geq R_c \\ \frac{zZe^2}{2R_c} \left( 3 - \frac{r^2}{R_c^2} \right) & r \leq R_c. \end{cases}$$

The function  $f(x)$  is chosen to be of Woods-Saxon form given as

$$f(x_i) = \frac{1}{1 + e^{x_i}} \quad x_i = \frac{r - r_i A^{1/3}}{a_i} \quad R_i = r_i A^{1/3}. \tag{1.24}$$

The parameters  $V, W, V_{LS}, W_{LS}, r_c, r_i$  and  $a_i$  are obtained from the fit to elastic scattering data. The program code CASCADE [27] numerically solves the Schrödinger equation to obtain  $T_l$  as a function of  $l$ . We employed global optical potential parameters given in Ref. [28–31] for the calculation of the transmission coefficient. The validity of the code has been checked by comparing the output with other calculations [32] as shown in Fig. 1.7.

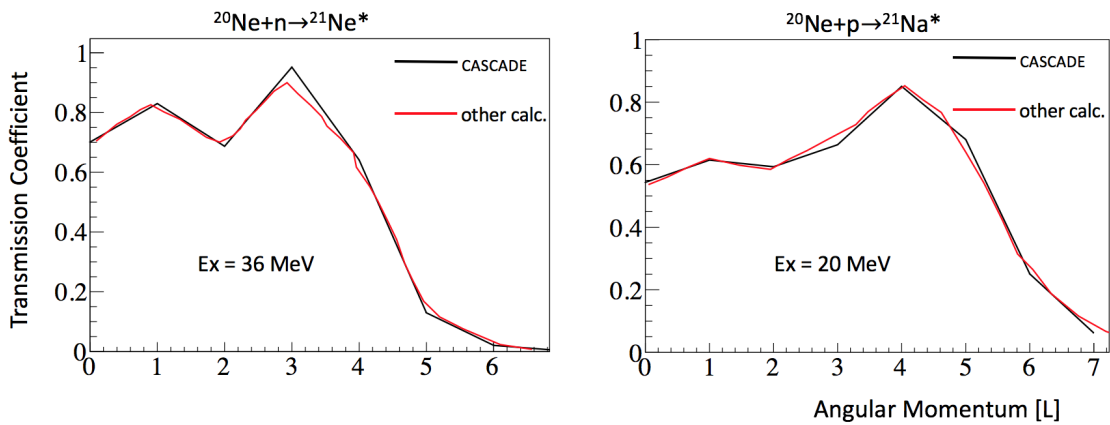
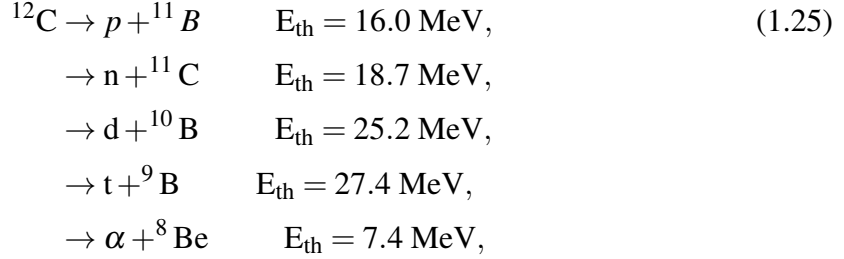


Fig. 1.7 Transmission coefficient as a function of angular momentum from CASCADE and other calculations.

The decay of an excited nucleus can proceed via different channels  $a = p, n, d, t$ , and  $\alpha$ . Excited  $^{12}\text{C}$  may decay via:



Then, the probability for an excited nucleus ( $E_x$ ) to decay to the  $i^{\text{th}}$  state of daughter nuclei can be given as

$$\tilde{c}_i = \frac{\beta_a \cdot T(E_x \rightarrow a + (A, i))}{\sum_{a,i} \beta_a \cdot T(E_x \rightarrow a + (A, i))}, \tag{1.26}$$

where  $\beta_a$  is the isospin Clebsch Gordan coefficient [33, 34]. Table 1.1 shows the calculations for  $^{12}\text{C}$  at  $E_x = 22 \text{ MeV}$ ,  $J^\pi = 1^-$  and  $T = 1$  decaying to  ${}^{11}\text{B}$  and  ${}^{11}\text{C}$ . With the increase in excitation energy, other channels ( $d, t, \text{etc.}$ ) also open up. The calculations were also performed for different excitation energies, spin-parities, and isospin.

Decay channel	Energy state (MeV) ( $J^\pi$ )	$T$	$T$	Isospin C.G. coefficient	$\tilde{c}$
$p + {}^{11}\text{B}$	g.s. ( $3/2^-$ )	$T_0 + 2T_2$	2.40	0.5	0.36
	2.12 ( $1/2^-$ )	$T_0 + T_2$	1.36	0.5	0.21
	4.44 ( $5/2^-$ )	$2T_2 + T_4$	0.05	0.5	0.01
	5.02 ( $3/2^-$ )	$T_0 + 2T_2$	0.48	0.5	0.07
$n + {}^{11}\text{C}$	g.s. ( $3/2^-$ )	$T_0 + 2T_2$	1.45	0.5	0.22
	2.00 ( $1/2^-$ )	$T_0 + T_2$	0.87	0.5	0.13

Table 1.1 Statistical model calculations for  $^{12}\text{C}$  at  $E_x = 22 \text{ MeV}$ ,  $J^\pi = 1^-$  and  $T = 1$ . The quantities  $T$  and  $t_i$  are the total total transmission coefficient and the individual transmission coefficients, respectively.

## 1.6 Electromagnetic Decays

Electromagnetic transition probability from initial state  $|i\rangle$  with spin  $J_i$  to final state  $|f\rangle$  with spin  $J_f$  is characterized by partial radiation width  $\Gamma_{fi}$ . The states are further characterized by energy, spin, and parity quantum numbers  $|i\rangle = |E_i, J_i, \pi_i\rangle$  and  $|f\rangle = |E_f, J_f, \pi_f\rangle$ . The photon

emission from  $|i\rangle \rightarrow |f\rangle$  is characterized by energy  $\hbar\omega = \hbar ck = E_i - E_f$ , where  $k$  is the wave vector,  $\hbar$  is a reduced Planck constant and  $c$  is the speed of light. The partial radiation width can be written as

$$\Gamma_{fi}^{XL} = \frac{8\pi(L+1)}{L[(2L+1)!!]^2} \left(\frac{E_\gamma}{\hbar c}\right)^{2L+1} B(XL) \downarrow, \quad (1.27)$$

where  $B(XL) \downarrow$  is the reduced transition probability of de-excitation given as

$$B(XL) \downarrow = \frac{|\langle iJ_i || \mathcal{M}^{XL} || fJ_f \rangle|^2}{2J_i + 1}, \quad (1.28)$$

where  $\mathcal{M}^{XL}$  is the multipole operator with multipolarity  $L$  and  $X = E$  refers to electric mode or  $X = M$  refers to magnetic mode of transition.

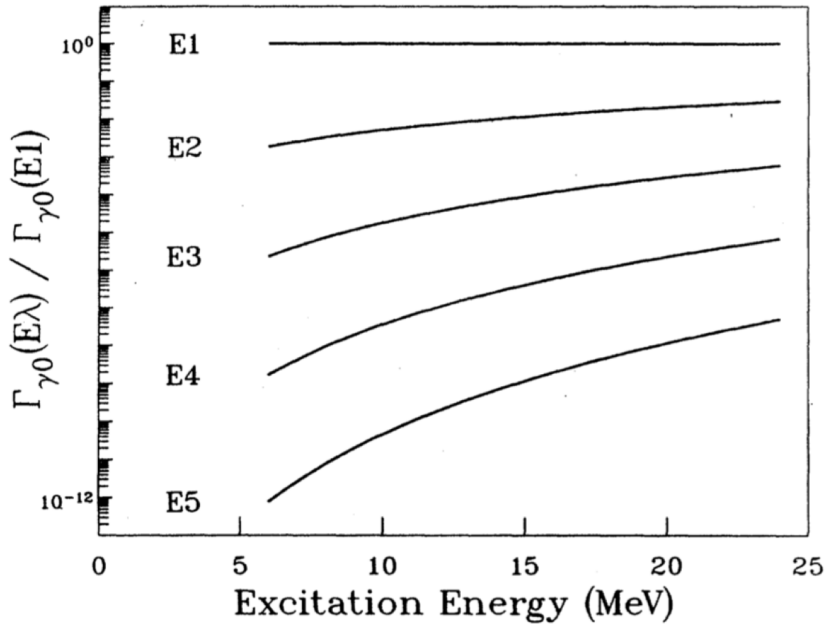


Fig. 1.8 The ground state  $\gamma$  widths of sharp state fully exhausting the appropriate energy weighted sum rule as a function of the excitation energy of the state, relative to the E1 width.

The electromagnetic decay of giant resonances is extremely sensitive to the multipolarity of the excited state. This can be demonstrated using Fig. 1.8 where the ground state  $\gamma$  width ( $\Gamma_{\gamma 0}$ ) expected for a sharp state exhausting 100% of the relevant EWSR is shown as a function of multipolarity and energy, relative to that for E1 transition. For an excited state of  $^{12}\text{C}$  with  $J^\pi = 1^-$ , the direct electromagnetic decay to the ground state would be dominated by E1 transition. The ground state  $\gamma$  decay width for a state at energy  $E$  decaying via E1

transition can be given as

$$\Gamma_{\gamma 0} = \frac{16}{9(\hbar c)^2} E^3 B(E1). \quad (1.29)$$

Previously, there has been only one such measurement of direct electromagnetic decays, that too for a heavy nucleus ( $^{208}\text{Pb}$ ) [15, 16] where the authors measured the direct  $\gamma$ -ray branching ratio from the giant resonances of  $^{208}\text{Pb}$ . They measured the energy-averaged branching ratio, integrated over the excitation energy interval 9.5-25 MeV to be  $0.019 \pm 0.002$ . There has been no such measurement for a light nucleus.

## 1.7 Objectives

The complete understanding of the decay mechanism of the giant resonances can be achieved by measuring the  $\gamma$  rays from their decay. The decays emitting  $\gamma$  rays with energy  $E_\gamma < 11$  MeV correspond to hadronic decays and the decays emitting  $\gamma$  rays with energy  $16 < E_\gamma < 32$  MeV correspond to electromagnetic decays. An experiment (E398) to measure these  $\gamma$  rays from the giant resonances of  $^{12}\text{C}$  was carried out at RCNP (Osaka University) with the following objectives.

1. Excitation of  $^{12}\text{C}$  to its giant resonances using a proton beam.
2. Measurement of  $\gamma$  rays from hadronic decays ( $E_\gamma < 11$  MeV) and as well as electromagnetic decays ( $16 < E_\gamma < 32$  MeV).
3. Study of the hadronic and electromagnetic decay mechanisms of the giant resonances.
4. Comparison of measurements with statistical model calculation.
5. Estimation of NC events at large scale scintillator-based detectors from core-collapse supernova using our measurements.

In the next chapter, a detailed description of the experimental setup is given. The analysis procedure and results are described in chapter 3 followed by the application of supernova NC events estimation in chapter 4. The thesis summary and conclusion is given in chapter 6.



# Chapter 2

## Experiment

The experiment (E398) to measure the  $\gamma$  rays emitted from giant resonances in  $^{12}\text{C}$  was carried out at Research Center for Nuclear Physics (RCNP), Osaka University. An unpolarized proton beam at 392 MeV bombarded the natural carbon ( $^{\text{nat}}\text{C}$ ) target with the beam bunch interval of 59 ns. The scattered protons were measured around  $0^\circ$  and were analyzed by the high-resolution magnetic spectrometer Grand Raiden (GR) [1]. In coincidence with scattered protons,  $\gamma$  rays were measured using an array of  $5 \times 5$  NaI(Tl) counters. A schematic view of the accelerator facility is shown in Fig. 2.1. The description of the experimental setup is provided in this chapter.

### 2.1 Beam and target

An unpolarized proton beam was produced by an Electron Cyclotron Resonance ion source, NEOMAFIOS [35] and injected to an Azimuthally Varying Field (AVF) cyclotron which accelerated it up to 65 MeV. The 65-MeV proton beam was further accelerated up to 392 MeV using the Ring cyclotron. The 392-MeV proton beam was then achromatically transported by WS beam line and bombarded the target. Faraday cup (FC) located at the beam dump was used to monitor the beam current. Also, the beam was finely tuned using the halo-free mode.

A natural carbon target with thickness  $36.3 \text{ mg/cm}^2$  and 99.9% purity was mounted at target frame. The natural abundance of  $^{12}\text{C}$  is 98.93%. The target frame was mounted on a movable target ladder and placed at the center of the scattering chamber. The scattering chamber was designed to be of a relatively smaller size in order to minimize the absorption of  $\gamma$  rays. The photo of the target ladder and scattering chamber is shown in Fig. 2.2.

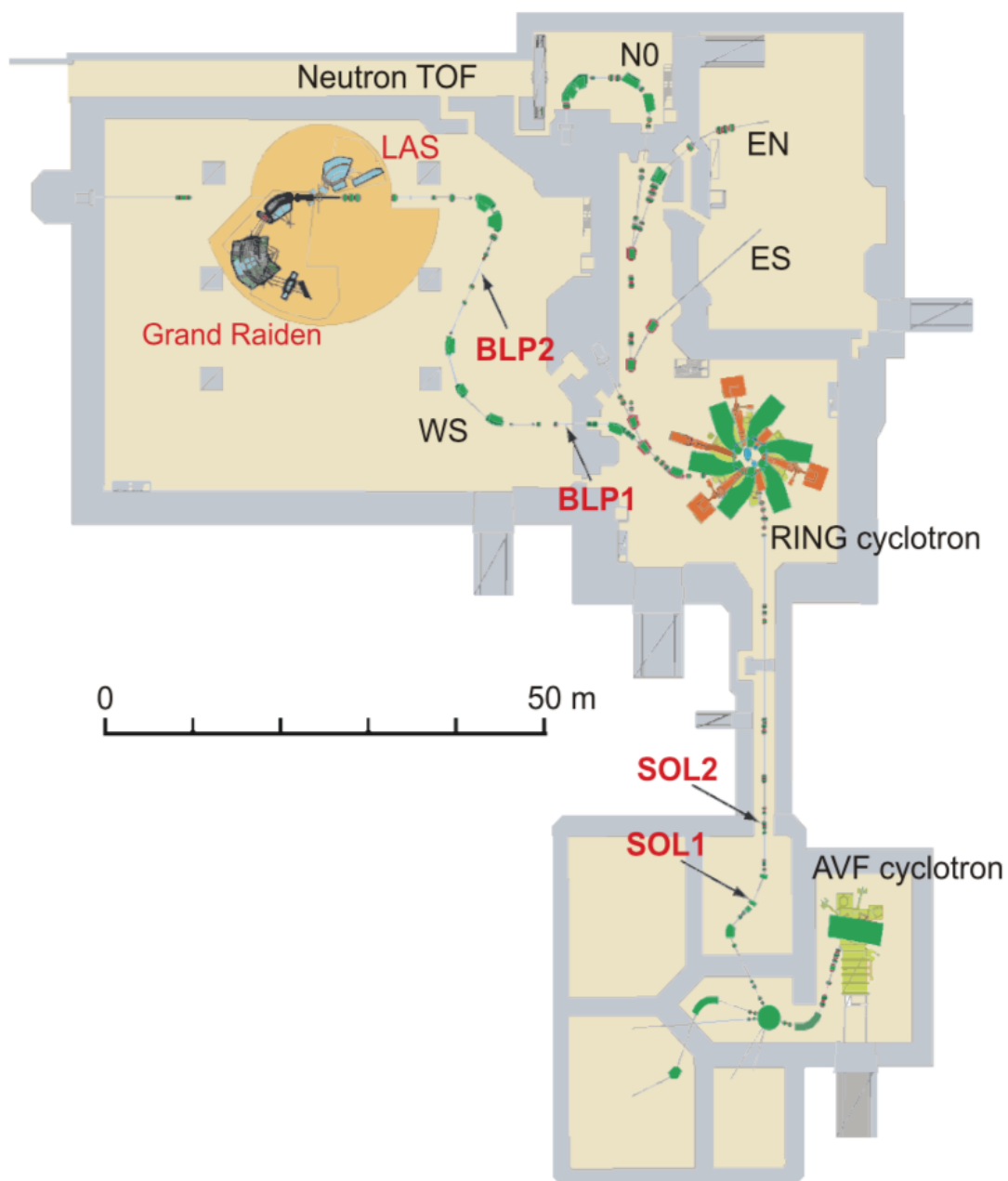


Fig. 2.1 An overview of the RCNP facility. The experiment was performed in the WS experimental hall, where the Grand Raiden spectrometer is located.

## 2.2 Magnetic Spectrometer

A schematic layout of the high-resolution spectrometer Grand Raiden at  $0^\circ$  mode is illustrated in Fig. 2.3. The spectrometer has a Q1-SX-Q2- D1-MP-D2(+DSR) configuration, where the



Fig. 2.2 Target ladder system (left) and scattering chamber (right).

capital letters specify the type of magnets. The letters D, Q, SX, and MP stand for the dipole, quadrupole, sextupole, and multipole, respectively. This magnetic configuration provides a high momentum resolution of  $p/\Delta p = 37000$ . The full design specifications are listed in Table 2.3. After passing through the spectrometer, the primary beam was transported to the beam dump where the beam current was monitored by  $0^\circ$  Faraday Cup (FC). The beam dump was shielded by concrete blocks to reduce the backgrounds for the focal plane detectors and the  $\gamma$ -ray detector.

Table 2.1 Specification of GR

Magnetic configuration	QSDMDD
Mear orbit radius	3m
Total deflection angle	$162^\circ$
Focal plane tilting angle	$45^\circ$
Maximum particle rigidity	5.4Tm
Vertical magnification (y y)	5.98
Horizontal magnification (x x)	-0.417
Momentum range	5%
Momentum resolution ( $p/\Delta p$ )	37076
Scattering angle setting	$0^\circ$
Acceptance of horizontal angle	$\pm 20\text{mr}$
Acceptance of vertical angle	$\pm 70\text{mr}$

After getting scattered at the target position and passing through a series of different magnets the beam was guided to the focal plane detectors. This detector system consisted of two multi-wire drift chambers (MWDC1 and MWDC2) followed by two plastic scintillators (PS1 and PS2) as shown in Fig. 2.4. The MWDC's measure a charged-particle track at the

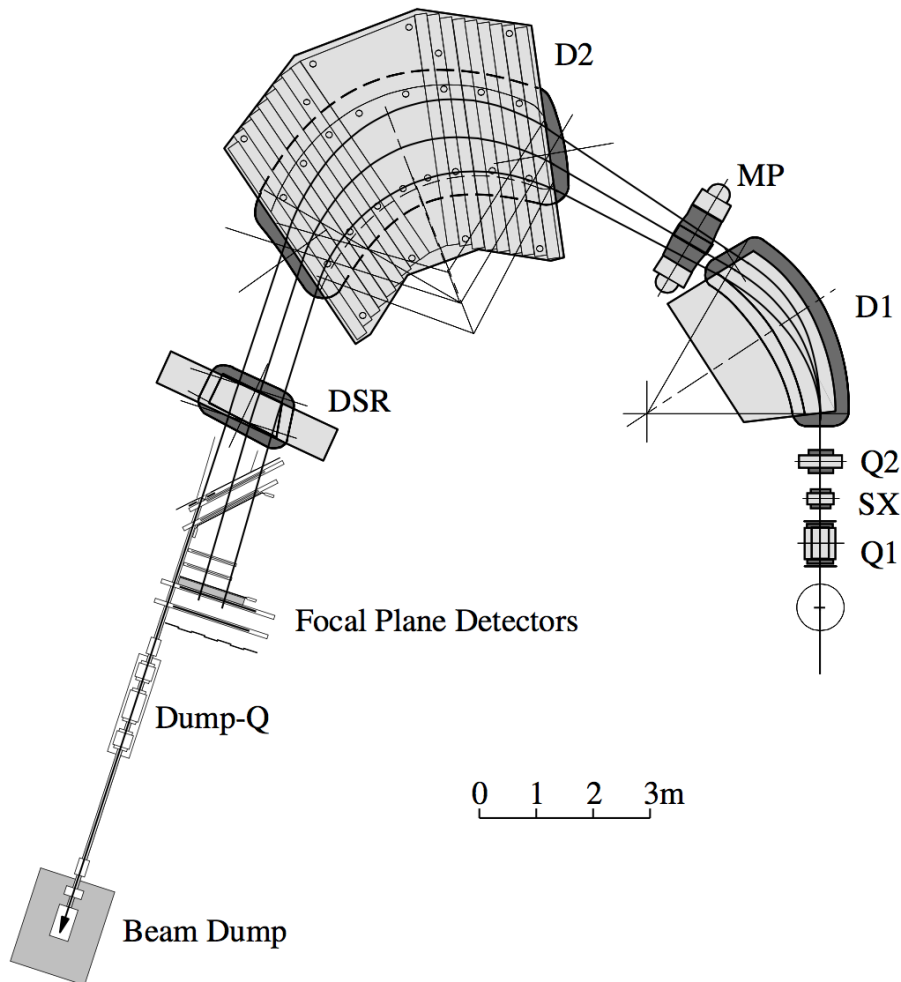


Fig. 2.3 Magnetic spectrometer "Grand Raiden" [1].

focal plane of the GR spectrometer and they were used to measure the excitation energy of the target nucleus ( $E_x$ ) and the scattering angle of the protons ( $\theta_p$ ) at the target position. Signals from MWDCs were pre-amplified and discriminated by LeCroy 2735DC board and the timing information of the wires was digitized by LeCroy 3377 time-to-digital converter (TDC). Each of the two plastic scintillators (PS) that were placed downstream of MWDCs were coupled with 2 photo-multiplier tubes (PMT) from both sides. These were used for particle identification and creating the fast trigger signal for the data acquisition system. The timing and pulse height information were digitized by TDC and analog to digital converter (ADC), respectively.

The structure of the MWDC is shown in Fig. 2.5. A charged particle passing the detector (MWDC) ionizes the gas and produces electron-ion pairs. The electrons drift due to the applied electric field with a relatively constant velocity of about  $5 \text{ cm}/\mu\text{s}$  from the place of

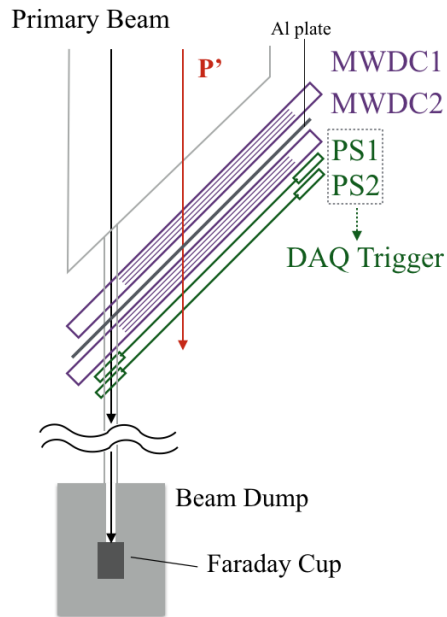


Fig. 2.4 Focal plane detectors of Grand Raiden.

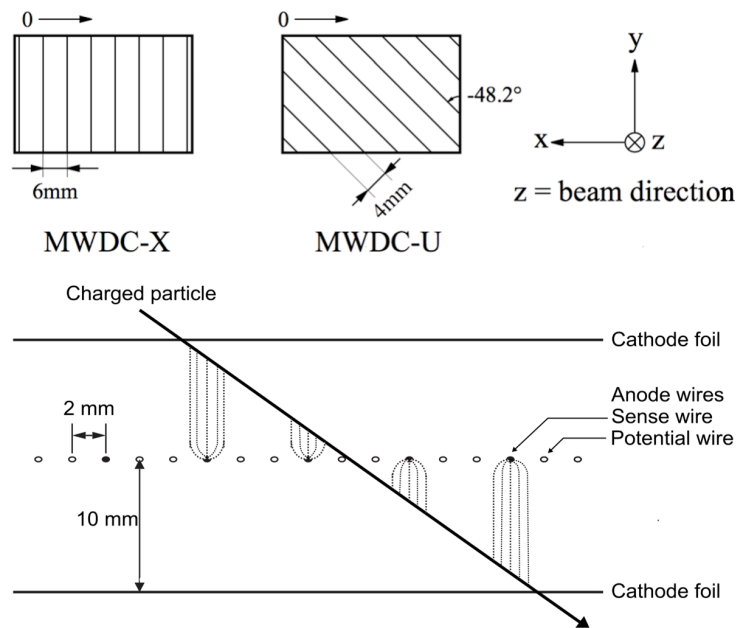


Fig. 2.5 Wire configuration (up) and structure (down) of MWDC [1].

ionization towards the anode plane. This approximate constancy can be achieved through secondary scattering, by a specific combination of gas mixture, pressure and applied electric field. For example, a high voltage of  $-0.4\text{kV}$  (X) and  $-0.5\text{kV}$  (U) was applied to the potential

wires in order to minimize the dependence of drift velocity on position. From the measured drift time the position can be deduced.

The spectrometer covers the scattering angle of  $0^\circ < \theta_p < 3.5^\circ$ . An energy resolution of 120 keV (FWHM) was achieved at  $E_x = 15.1$  MeV. The details of the GR spectrometer has been described elsewhere [1, 36].

### 2.3 $\gamma$ -ray detector

A  $\gamma$ -ray detector was made of  $5 \times 5$  NaI(Tl) counters ( $2'' \times 2'' \times 6''$  each) and it was placed at  $\theta_\gamma = 90^\circ$  with respect to the beam direction and at a distance of 10 cm from the target as shown in Fig. 2.6. Two plastic scintillators with a thickness of 3 mm were placed in front of the  $\gamma$ -ray detector in order to separate the background by charged particles directly entering the  $\gamma$ -ray detector. Both ADC (charge information) and TDC (time information) of each NaI counter were digitized by LeCroy FERA and FERET systems and were recorded by the DAQ system.

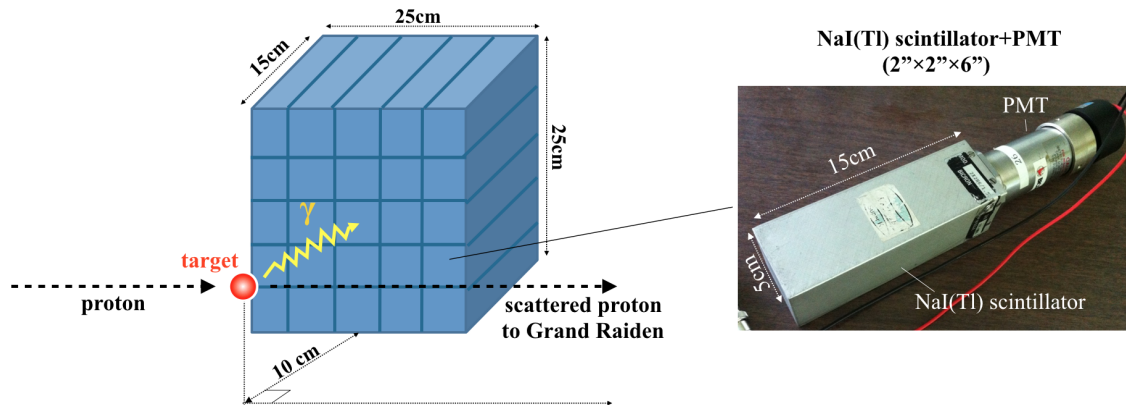


Fig. 2.6 An array of  $\gamma$ -ray detector (left) and a NaI(Tl) scintillation counter (right).

Table 2.2 Radioactive sources used for the detector performance check.

Sources	$E_\gamma$ [MeV]
$^{137}\text{Cs}$	0.67
$^{60}\text{Co}$	1.17 and 1.33
$^{241}\text{Am} + \text{Be}$	4.43
$^{252}\text{Cf} + \text{Ni}$	8.54 and 8.99

### 2.3.1 Detector performance: Off beam

The initial energy calibration for NaI counters was done using various sources before the beam time. The sources used are tabulated in Table 2.2. The high energy response was checked using quasimonochromatic  $\gamma$ -ray beams (33.3 MeV) produced at the synchrotron radiation

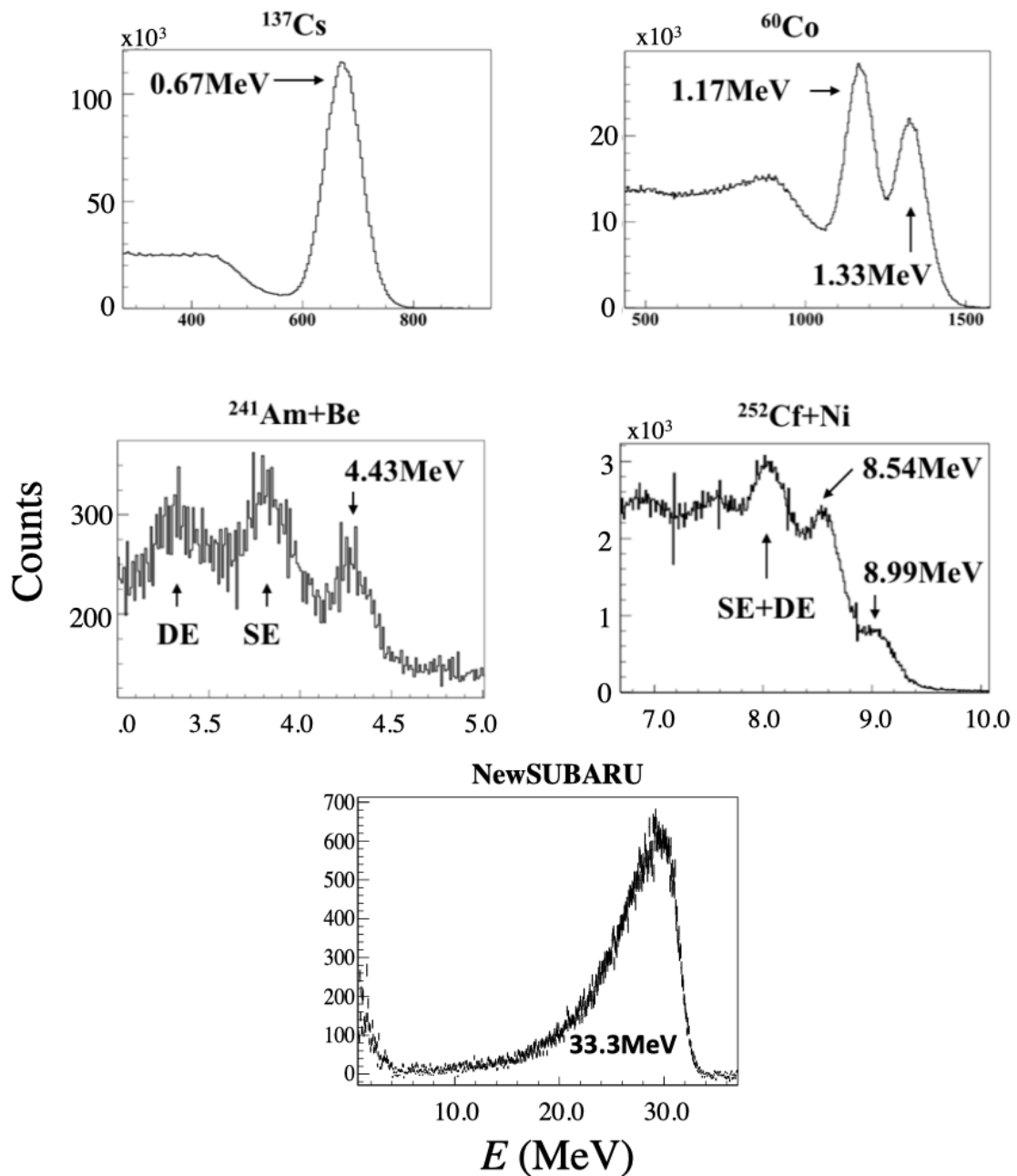


Fig. 2.7 The energy spectra taken by radioactive sources. SE (DE) denotes single (double) escape peak.

facility NewSUBARU in the inverse Compton scattering of Nd : YVO<sub>4</sub> laser photons from relativistic electrons (2.11). The details of this experiment are shown in the next section.

Various energy spectra from different sources is shown in Fig. 2.7. The variation of energy resolution with  $\gamma$ -ray energy is shown in Fig. 2.8(up) and was fitted using the function shown in Eq. (2.1).

$$\sigma(\text{keV}) = 1.41\sqrt{E_\gamma} - 9.5. \quad (2.1)$$

The calibration plot of  $\gamma$ -ray energy versus ADC channel (Fig. 2.8(down)) shows linear distribution. Hence, the linearity of pulse height was achieved for the energy range from 0.67 to 33.3 MeV.

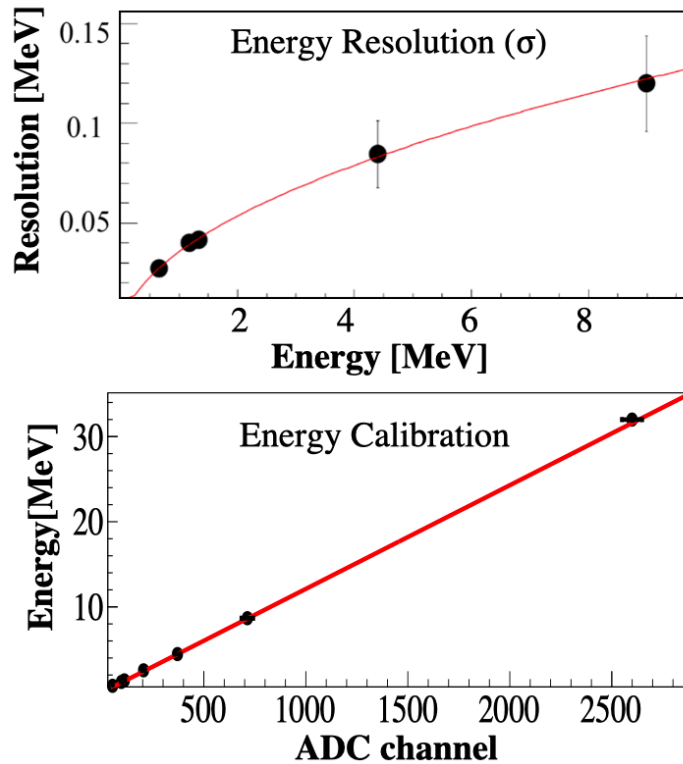


Fig. 2.8 Energy resolution and pulse height response of a NaI counter.

The response functions of the  $\gamma$ -ray detector were generated by Monte Carlo simulations (MC) using the program “Geant4”. The response function  $P(E_\gamma; E)$  is defined as the probability for a  $\gamma$  ray of energy  $E_\gamma$  irradiated uniformly upon the target position to be measured as energy  $E$  by the  $\gamma$ -ray detector. The detector geometry and the effect of the materials between the target and detector were taken into account during the detector simulation. The response functions were normalized by the  $\gamma$  rays emitted by the source calculated by the source’s known radioactivity and the measuring time. The response functions reproduce both

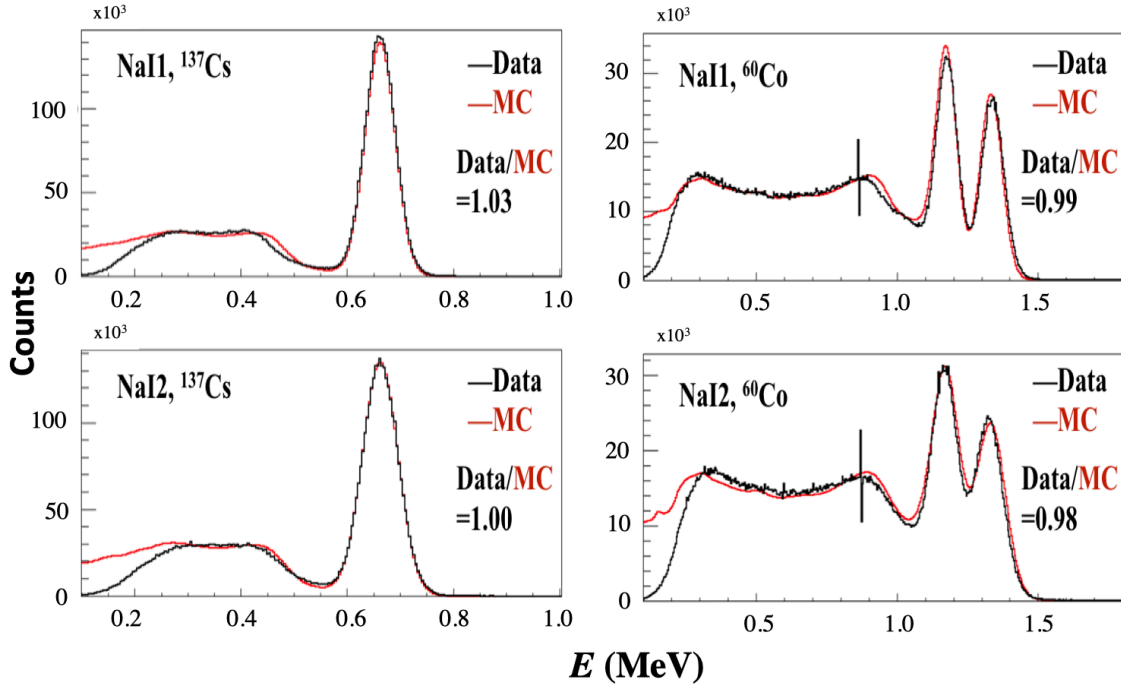


Fig. 2.9 The measured energy spectra (black) and normalized response function (red). Data/MC shown in the figures is the number of events from the data divided by that from the normalized response function with energy higher than 0.3 MeV for  $^{137}\text{Cs}$  and 0.5 MeV for  $^{60}\text{Co}$ .

the shape as well as detection efficiency within an uncertainty of 3%. The comparison of data and normalized response functions for  $^{137}\text{Cs}$  and  $^{60}\text{Co}$  source is shown in Fig. 2.9.

### 2.3.2 NewSUBARU: Experiment

Quasimonochromatic  $\gamma$ -rays are produced at NewSUBARU facility in the inverse Compton scattering of laser photons from electrons at 974 MeV electrons injected from a linear accelerator into NewSUBARU storage ring. The injected beam can be either accelerated up to 1.5 GeV or decelerated down to 0.5 GeV. The experimental setup for the present measurement is depicted in Fig. 2.10. The laser is produced outside the ring and was guided through four mirrors and one lens into vacuum tube to the collision points, P1 (for  $\text{CO}_2$  laser) and P2 (Nd :  $\text{YVO}_4$  laser). The stability and alignment of optical elements were checked using He-Ne laser beam. The energy of the Compton scattered  $\gamma$  rays can be given by the following equation:

$$E_\gamma = \frac{4\varepsilon_p(\gamma^2/1+R)}{1+(\gamma^2/1+R)\theta^2}, \quad (2.2)$$

where

$$\gamma = \frac{E}{m_e c^2}, \quad R = \frac{4\gamma\epsilon_p}{m_e c^2}. \quad (2.3)$$

The laser photon with energy  $\epsilon_p$  collides with electron with kinetic energy  $E$  and  $E_\gamma$  is the energy of scattered photon scattered at angle  $\theta$ .

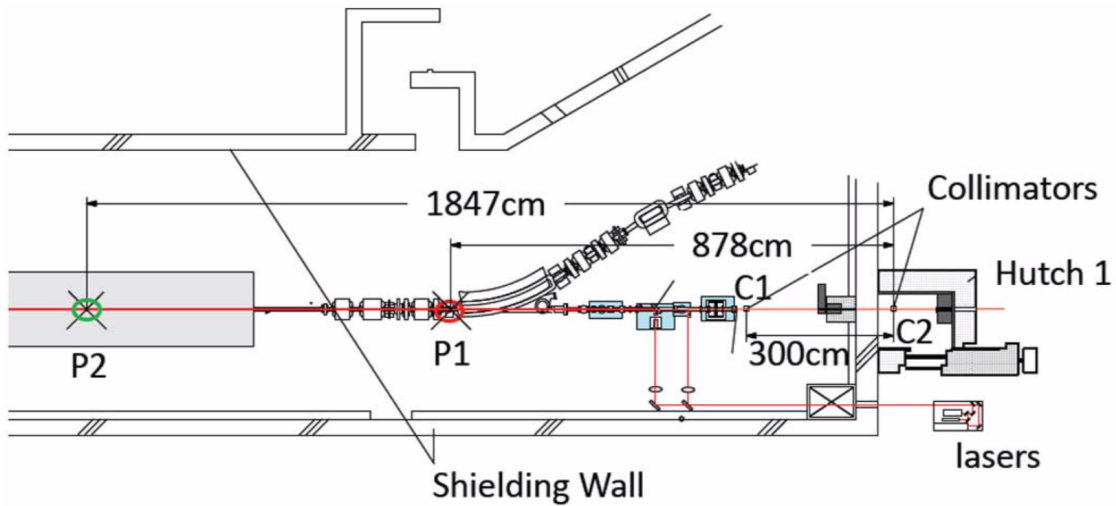


Fig. 2.10 Experimental setup at NewSUBARU facility.



Fig. 2.11 NaI(Tl) detector (same used for E398 experiment) used for measuring 33 MeV  $\gamma$ -rays at NewSUBARU facility.

## 2.4 Trigger and data acquisition system

The DAQ system was divided into two components, GR-DAQ and  $\gamma$ -DAQ. The logic circuit of the plastic scintillators (PS) at the focal plane is shown in Fig.2.12. The charge from each end (Left and Right) of a PS was divided into two signals. One of them was transferred to

Table 2.3 Different  $\gamma$  ray energies obtained from inverse scattering of different laser photons.

Laser	Wavelength ( $\mu m$ )	$E = 1 \text{ GeV}$ $E = 1.5 \text{ GeV}$	
		$E_\gamma \text{ (MeV)}$	
Nd : YVO <sub>4</sub> / $\omega$	1.064	17.0	35.1
Nd : YVO <sub>4</sub> / $2\omega$	0.532	32.8	68.5
CO <sub>2</sub>	10.59	1.63	3.6

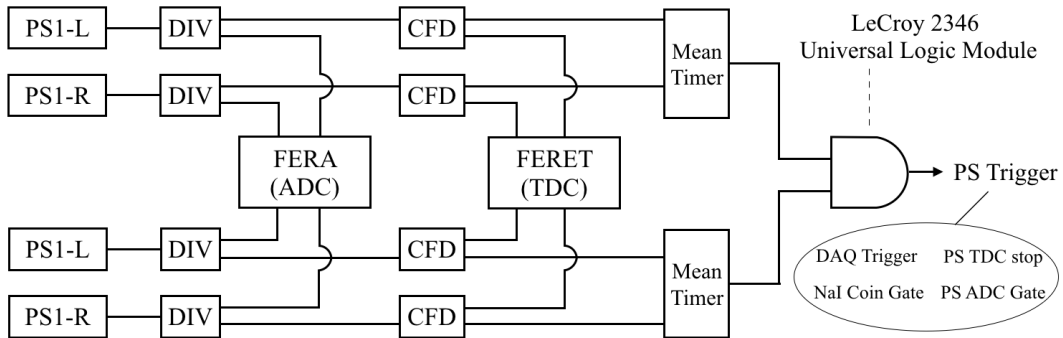


Fig. 2.12 Circuit diagram of the plastic scintillators.

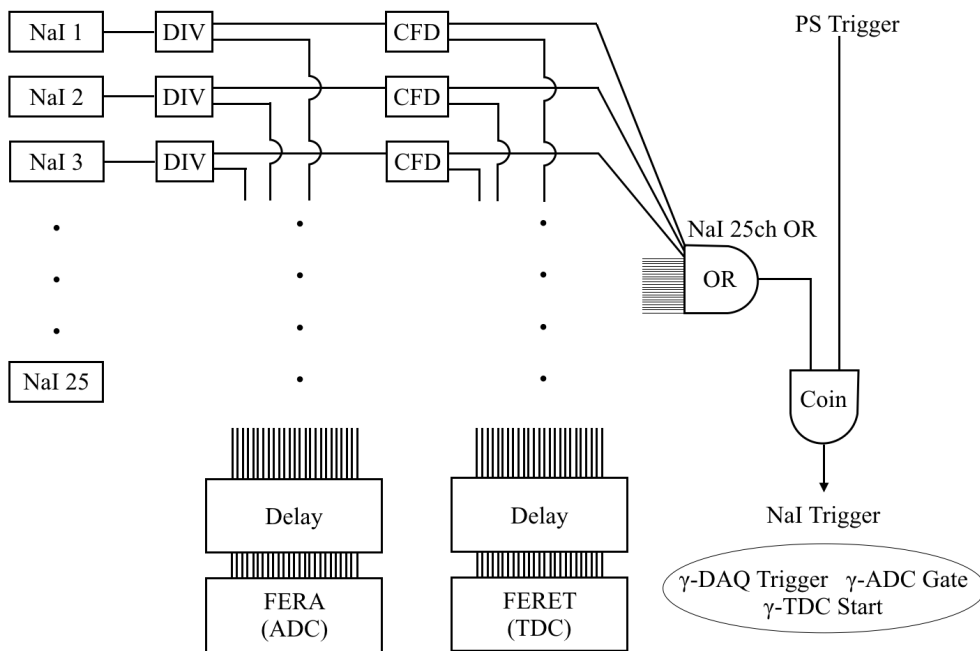


Fig. 2.13 Circuit diagram of PS Trigger and NaI Trigger.

ADC (FERA) for pulse height information and the other was discriminated by a constant fraction discriminator (CFD) and transferred to TDC (FERET) for time-of-flight information. Furthermore, the CFD outputs were also sent to a mean timer module in order to generate a

coincidence signal for each PS. The coincidence signals of 2 PSs were transferred to a LeCroy 2346 Universal Logic Module of the field programmable gate array (FPGA) chip. A PS trigger was generated by the coincidence of discriminator signals of two plastic scintillators and was used for GR-DAQ trigger. The details of the DAQ system of Grand Raiden are described in Ref.[37].

The circuit diagram of the  $\gamma$ -ray detector is shown in Fig 2.13. The same type of ADC and TDC read-out modules as mentioned above were used for the  $\gamma$ -ray detector. The CFD outputs from 25 NaI counters were transferred to a coincidence module and an OR signal was generated if at least one of the NaI counters recorded a hit. The OR signal was then transferred to another coincidence module together with the PS trigger signal. A NaI-Trigger signal was generated by taking the coincidence of the PS trigger signal and the NaI-OR signal and was used for GAM-DAQ Trigger.

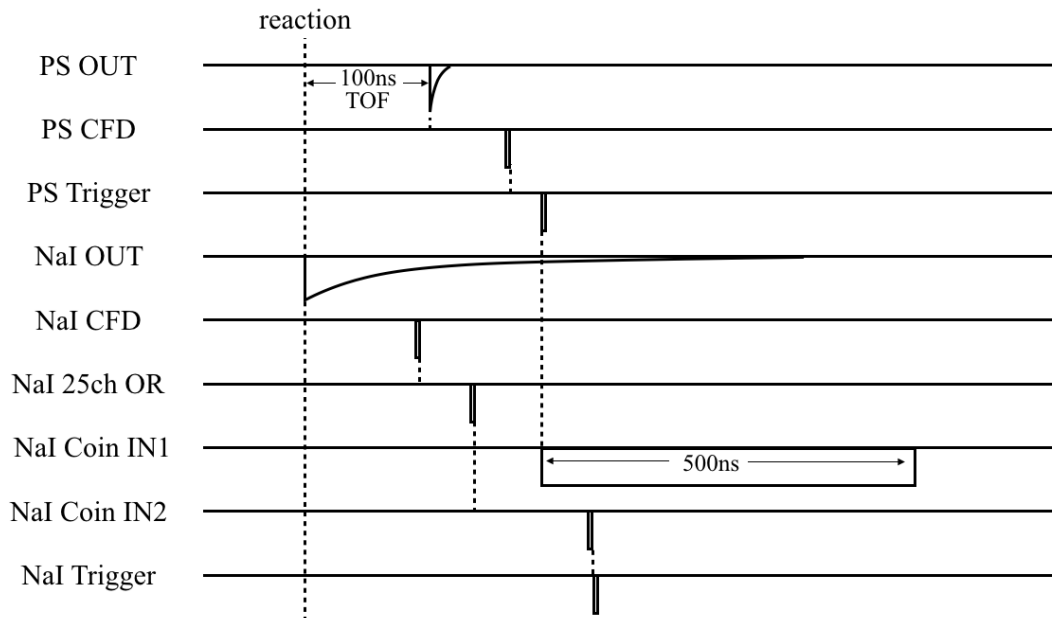


Fig. 2.14 Timing chart of signals.

## 2.5 $\gamma$ -ray background subtraction

We selected the prompt  $\gamma$  rays and subtracted the accidental coincidences using the TDC information for each  $E_x$  interval. The time difference between the GAM signal, which is defined as the sum of discriminator signals of all NaI counters and the PS trigger is plotted in Fig.2.15 for  $\gamma$  rays from  $^{12}\text{C}(15.11 \text{ MeV}, 1^+, T = 1)$ . Events in the prominent first peak (red) was selected as the coincidence events between the two signals, whereas those in the other

peaks were selected as accidental events (background). Pulse intervals of 60 nsec correspond to the bunch structure of the beam. The  $\gamma$ -ray energy spectrum (red line) and background spectrum (blue line) for  $E_x$  at 15.11 MeV are shown in Fig.2.15(b).

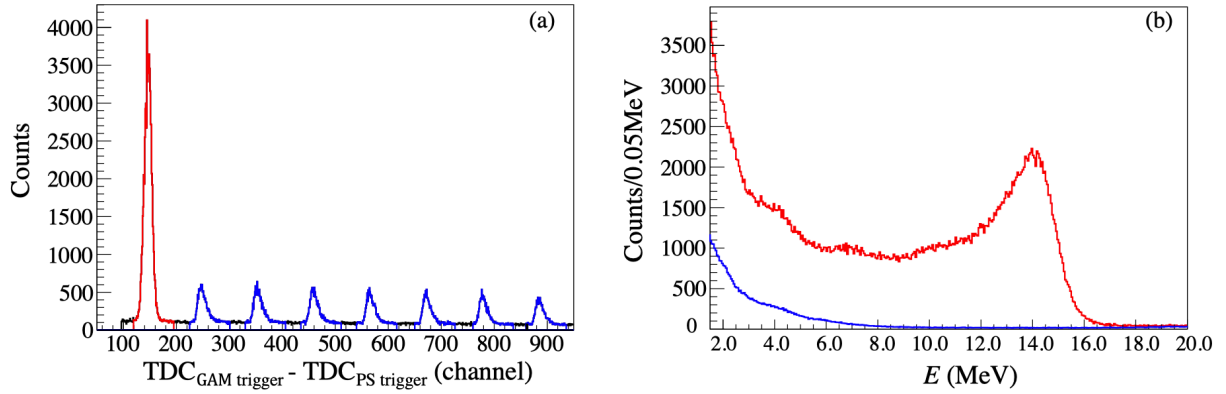


Fig. 2.15 (a) Time difference between  $\gamma$  trigger and PS trigger. (b)  $\gamma$ -ray energy spectrum (red) and background spectrum (blue) for 15.11 MeV state ( $1^+$ ,  $T = 1$ ) of  $^{12}\text{C}$ .

## 2.6 On Beam: Calibration

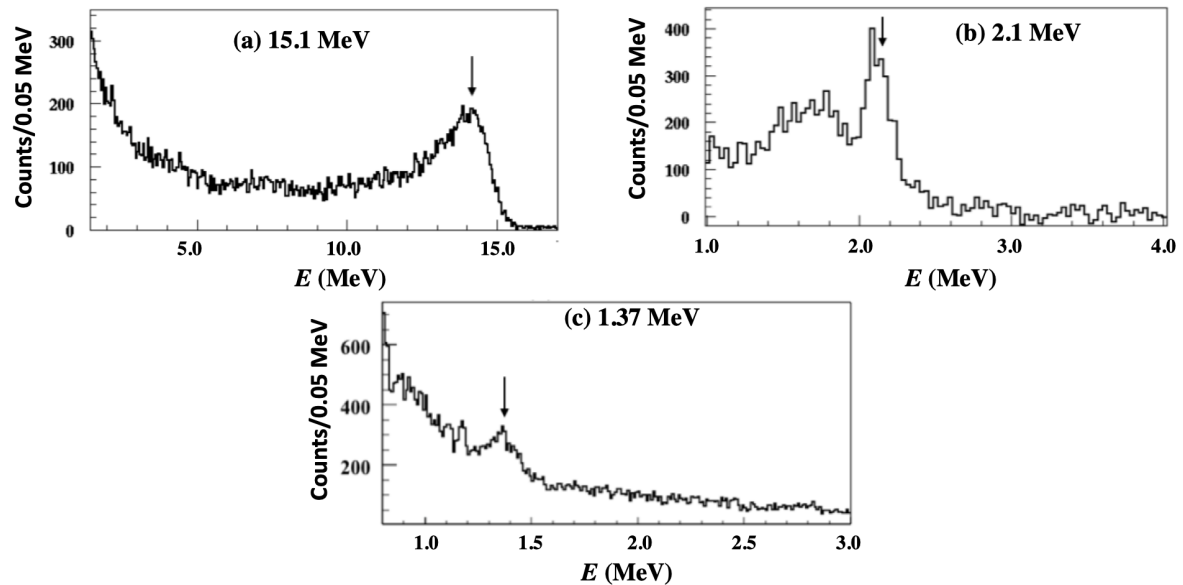


Fig. 2.16 (a) In-situ  $\gamma$  rays used for calibration of energy response.

While the initial energy calibration for NaI counters was done using different sources before the experiment, the energy response of NaI counters decreased gradually during the

beam time due to the irradiation by beam-induced particles. Therefore, we calibrated the energy response of each NaI counter for each run (typically 2 hours) using the following in-situ  $\gamma$  rays,  $^{12}\text{C}$  (15.11 MeV,  $1^+$ ),  $^{11}\text{B}$  (2.12 MeV,  $1/2^-$ ) and 1.37 MeV from  $^{24}\text{Mg}^*$  shown in Fig. 2.16. The  $\gamma$  ray of 1.37 MeV was induced by the secondary interactions with the aluminum of the chamber surrounding the target. The mean energy 1.37 MeV was determined by the nearby Germanium counter. During the in-situ calibration, we found that 15 downstream counters had poor energy resolution and we used only the other 10 upstream counters. The energy resolution  $\sigma(E)/E$  of each counter among 10 upstream counters was 5% at 2 MeV and 3% at 15 MeV. The experiment was conducted using three beam intensities, 0.5, 1.0 and 1.5 nA but the gain variation was least for the 0.5 nA dataset; hence, this dataset was used for the  $\gamma$ -ray analysis.

# Chapter 3

## Analysis and Results

### 3.1 Magnetic Spectrometer Analysis

The double differential cross section is given as

$$\sigma_{p,p'} \equiv \frac{d^2\sigma}{d\Omega dE_x} = J \frac{N_{E_x}}{\Delta E_x} \frac{1}{\Omega} \frac{1}{L\eta} \frac{e}{Q} \frac{A}{N_A \rho}, \quad (3.1)$$

where  $J$  is the Jacobian for the transformation from the laboratory frame to CM (center of

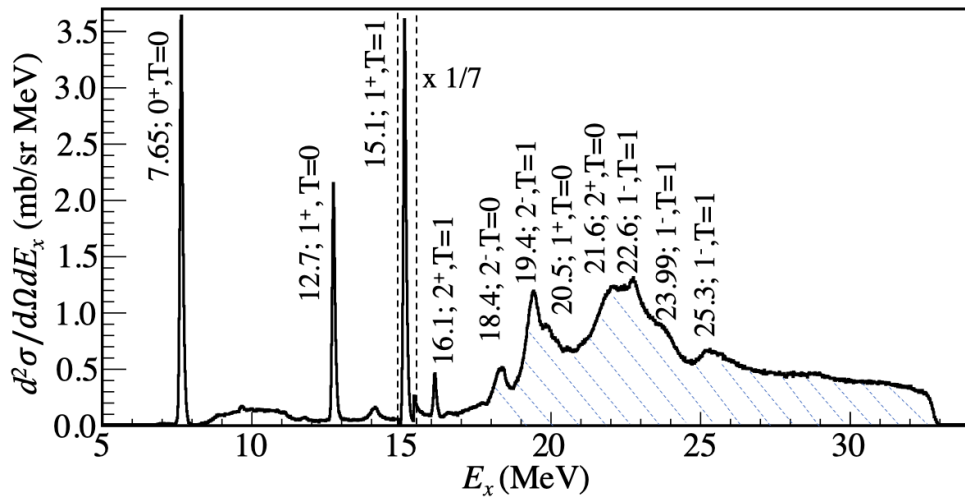


Fig. 3.1 Double differential cross section of the  $^{12}\text{C}(p,p')$  reaction at  $E_p = 392$  MeV and  $\theta = 0^\circ$ .

mass) frame (0.81),  $\eta$  is the tracking and trigger efficiency (0.91),  $L$  is the DAQ live time,  $e$  is the elementary charge (C),  $Q$  is the total beam charge (C), and  $N_{E_x}$  is the number of excitation events in the energy range  $E_x$  and  $E_x + \Delta E_x$  obtained after subtracting the background. The

$E_x$ (MeV)	$N_{E_x}$	systematic uncertainty (%)
16-18	665973	1.6
18-20	2827890	1.8
20-22	3170340	1.9
22-24	4070890	2.4
24-26	2401860	2.0
26-28	1887220	1.8
28-30	1738970	2.3
30-32	1596650	2.6

Table 3.1 The number of excitation events for different energy regions and the systematic uncertainty in their estimation.

Variable	Value
Tracking efficiency ( $\eta$ )	1%
Solid angle ( $\Omega$ )	3%
Beam charge (Q)	3%
Target thickness (t)	2%
Background subtraction	3%
Total	6%

Table 3.2 Systematic uncertainties in the measurement of differential cross section.

detailed procedure for background subtraction was provided in Ref. [36]. Furthermore,  $A$  is the atomic weight (g/mol),  $N_A$  is Avogadro's number, and  $\rho$  is the areal density (36.3 mg/cm<sup>2</sup>). The spectrometer acceptance was not symmetrical with respect to the horizontal and vertical directions ( $-9 \text{ mrad} \leq \theta_x \leq 0 \text{ mrad}$ ,  $|\theta_y| \leq 43 \text{ mrad}$ ). The events were chosen within a solid angle ( $\Omega$ ) of 0.77 msr.

The measured cross section of  $^{12}\text{C}(p,p')$  is shown in Fig. 3.1. Giant resonances are clearly seen in the spectrum. We list the excitation energies  $E_x$ , spin-parities ( $J^\pi$ ), and isospin ( $T$ ) of the known resonances in Table 4.2. We show the differential cross section for  $^{12}\text{C}(15.11 \text{ MeV}, 1^+, T = 1)$  and  $^{16}\text{O}(11.5 \text{ MeV}, 2^+, T = 0)$  in Fig. 3.2, demonstrating the consistency of our cross section with those of previous experiments performed using the same GR spectrometer at the same beam energy [2, 3]. Our cross section measurements of  $^{16}\text{O}(11.5 \text{ MeV}, 2^+, T = 0)$  were performed during the same experiment with a cellulose ( $\text{C}_6\text{H}_{10}\text{O}_5$ ) target. Both of our measured cross sections are consistent with those measured in previous experiments within the systematic uncertainty of 6%.

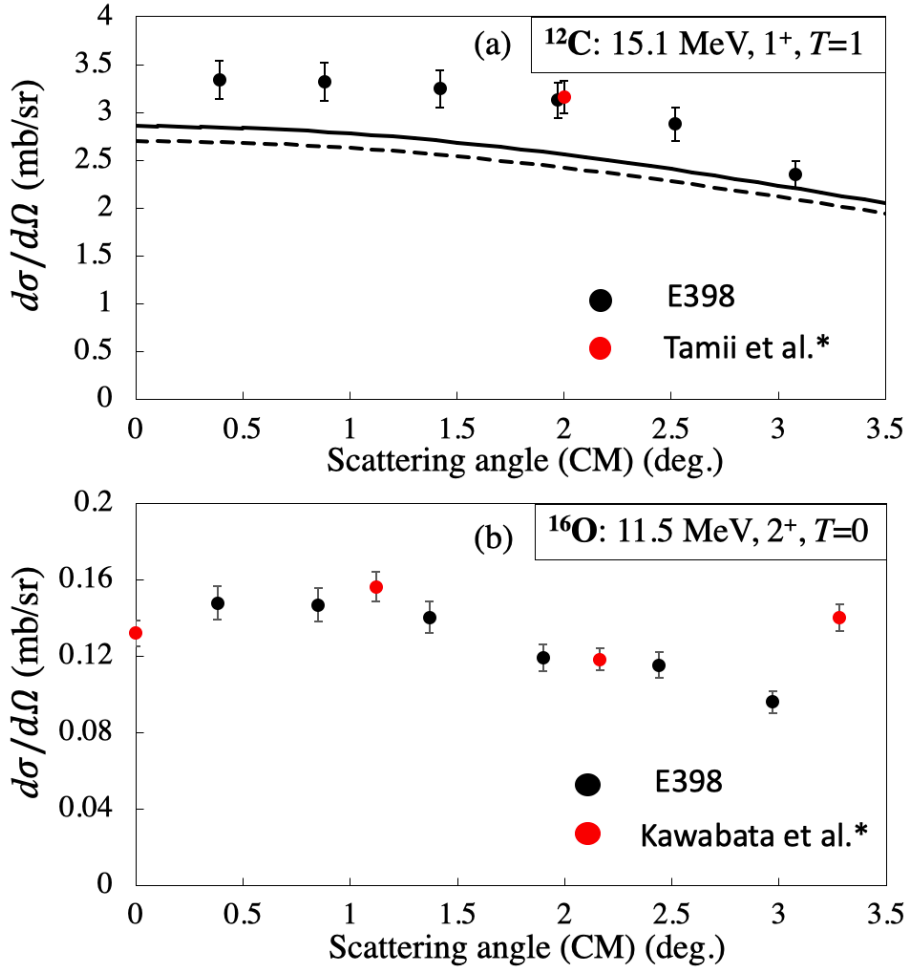


Fig. 3.2 (a) Differential cross section of the  $^{12}\text{C}(p,p')$  reaction as a function of scattering angle (black data points) and comparison with previous experiment [2] (red data points). Solid and dashed lines are the DWBA calculation results for the transitions to 15.1 MeV state (see text for details). (b) Differential cross section for  $^{16}\text{O}(p,p')$  reaction as a function of scattering angle and comparison with previous experiment [3].

## 3.2 $\gamma$ -ray Analysis

The response functions of the  $\gamma$ -ray detector were generated by Monte Carlo simulations (MC) using version 10.4.9 patch 04 of the Geant4 toolkit. The response function  $P(E_\gamma; E)$  is defined as the probability for a  $\gamma$  ray of energy  $E_\gamma$  irradiated uniformly upon the target position to be measured as energy  $E$  by the  $\gamma$ -ray detector, and

$$\int_{E_{th}}^{E_{max}} P(E_\gamma; E) dE = \eta(E_\gamma), \quad (3.2)$$

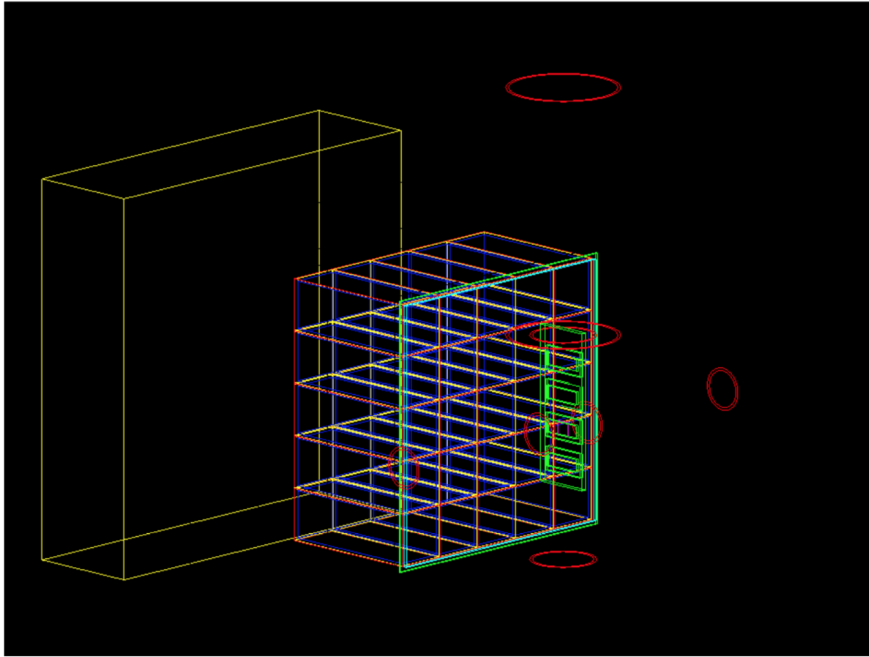


Fig. 3.3 Geometrical set up in the MC simulation depicting various components and materials (Blue = NaI).

where  $\eta(E_\gamma)$  is the detection efficiency for a  $\gamma$  ray of energy  $E_\gamma$ . For the present case, the threshold ( $E_{th}$ ) for the  $\gamma$ -ray detectors was chosen to be 1.5 MeV. The detector geometry and the effect of the materials between the target and detector were taken into account during the detector simulation. The accuracy of the response functions was tested by comparison with the  $\gamma$ -ray spectra of 15.1 MeV and 6.9 MeV measured during the experiment.

To generate the response function of a 15.1 MeV  $\gamma$  ray, cascade  $\gamma$  rays from the 15.1 MeV state [7], 10.66, 7.45, 4.8, 4.4 and 2.4 MeV, were also taken into account, along with their respective branching ratios. The response function was then normalized by the 15.1 MeV excitation counts measured by the spectrometer in the energy range of  $E_x = 14.9$ -15.4 MeV. Further, we determined the correction factor (0.88) for the response function to account for the dead time of the  $\gamma$ -ray detector by normalizing the data to reproduce the well-measured 15.1 MeV  $\gamma$ -ray emission probability ( $\Gamma_\gamma/\Gamma = 0.96 \pm 0.04$ ). The response function for a 15.1 MeV  $\gamma$  ray is shown in Fig. 3.5(a) (red line) along with the  $\gamma$ -ray energy spectrum measured from the  $^{12}\text{C}$  (15.1 MeV,  $1^+$ ) (black data points) after subtracting the background spectrum. The procedure for measuring the  $\gamma$ -ray spectrum and background subtraction was described previously and shown in Fig. 2.15. The photopeak and single- and double-escape peaks appear as one broad peak due to the resolution of the  $\gamma$ -ray detector. This correction factor (0.88) was used to scale the response function of all the other  $\gamma$  rays.

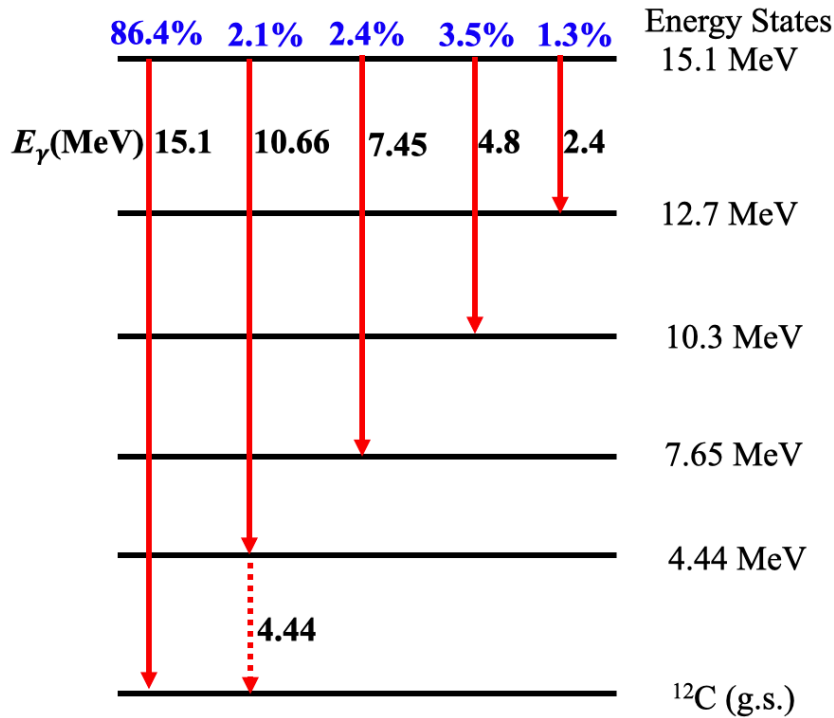


Fig. 3.4 Cascade  $\gamma$  rays from 15.1 MeV state of  $^{12}\text{C}$ .

We show in Fig. 3.5(b) the  $\gamma$ -ray spectrum (after background subtraction), as measured from  $E_x(^{16}\text{O}) = 6.9\text{-}7.3$  MeV. Within this range, two states of  $^{16}\text{O}$ , 6.9 MeV and 7.1 MeV were excited. These states decay to the ground state by emitting 6.9 MeV and 7.1 MeV  $\gamma$  rays, respectively, with 100% emission probability. The response functions were generated for 6.9 MeV and 7.1 MeV and weighted according to their contribution. A comparison with the response function normalized by excitation counts in the same  $E_x$  range is shown in Fig. 3.5(b). When the value of data/MC for 15.1 MeV was normalized to 1.0 using the correction factor (0.88), the same factor yields data/MC =  $0.98 \pm 0.02$  for 6.9 MeV (including 7.1 MeV). The efficiency ( $\eta(E_\gamma)$ ) was evaluated to be 2.3% for  $E_\gamma = 2.0$  MeV and 5.9% for  $E_\gamma = 15.1$  MeV.

For the lower  $\gamma$ -ray energy range, the consistency was checked off-beam using a  $^{60}\text{Co}$  source that emits two simultaneous  $\gamma$  rays with energies of 1.13 and 1.33 MeV. The response function generated for  $^{60}\text{Co}$  reproduced the data within an uncertainty of 3%. The consistency between data and response function within the systematic uncertainty of 5% validates our measurement of  $\gamma$ -ray emission probability for the energy range from 1.1-15.1 MeV.

It should be noted that the  $\gamma$ -ray emission probability has been calibrated using the well-known emission probability of  $\gamma$ -rays from 15.1 and 6.9 MeV state. This validates our

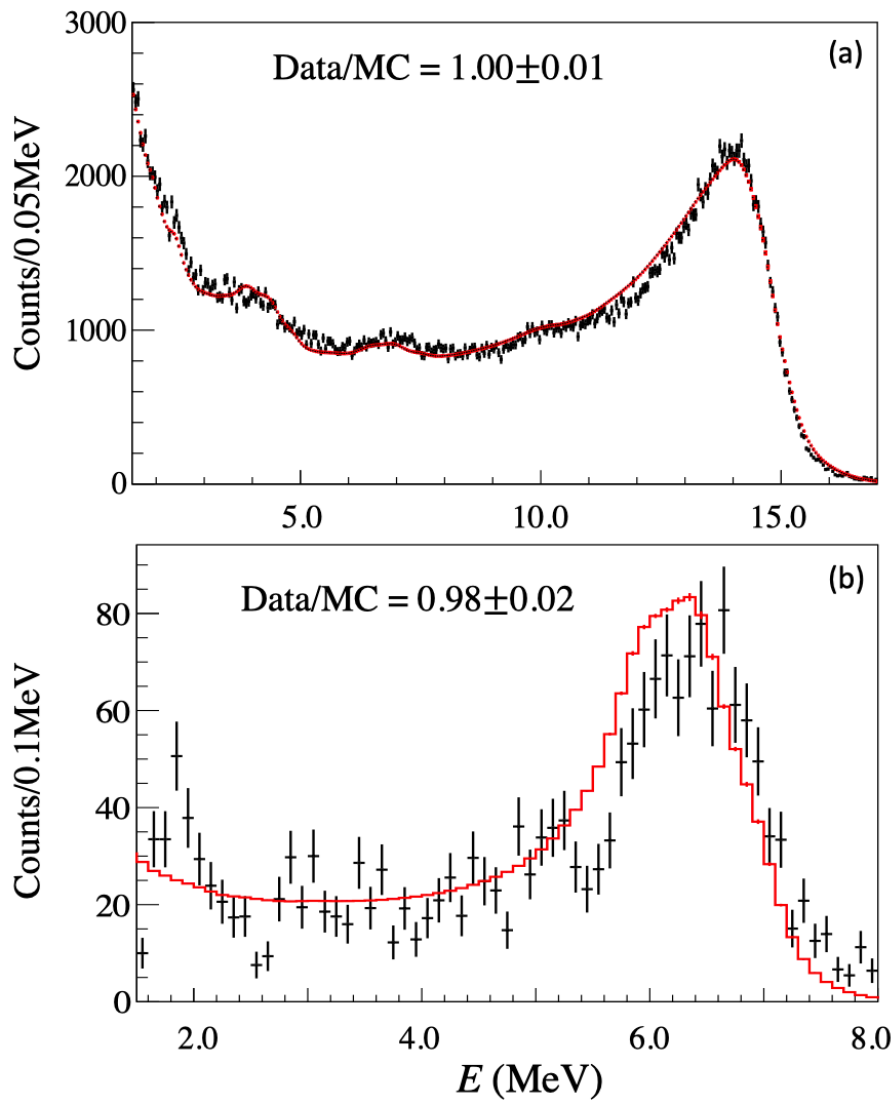


Fig. 3.5 Measured  $\gamma$ -ray spectrum (black) after background subtraction and response function (red line) for the (a) 15.11 MeV state ( $J^\pi = 1^+$ ) of  $^{12}\text{C}$  (b) 6.9 MeV state ( $J^\pi = 2^+$ ) of  $^{16}\text{O}$  (see text for details).

measurement of  $\gamma$ -ray emission probability from the giant resonances (described in the next chapter).

### 3.3 $\gamma$ rays from the giant resonances

The two-dimensional histogram shows the  $\gamma$ -ray coincidence events for one of the ten NaI(Tl) counters. The line  $E_x - E > 0$  marks the energy conservation limit as there should be no  $\gamma$

rays with energy higher than the excitation energy of  $^{12}\text{C}$ . The events detected in the region  $E_x - E < 0$  are the accidental coincidences caused due to scattered protons.

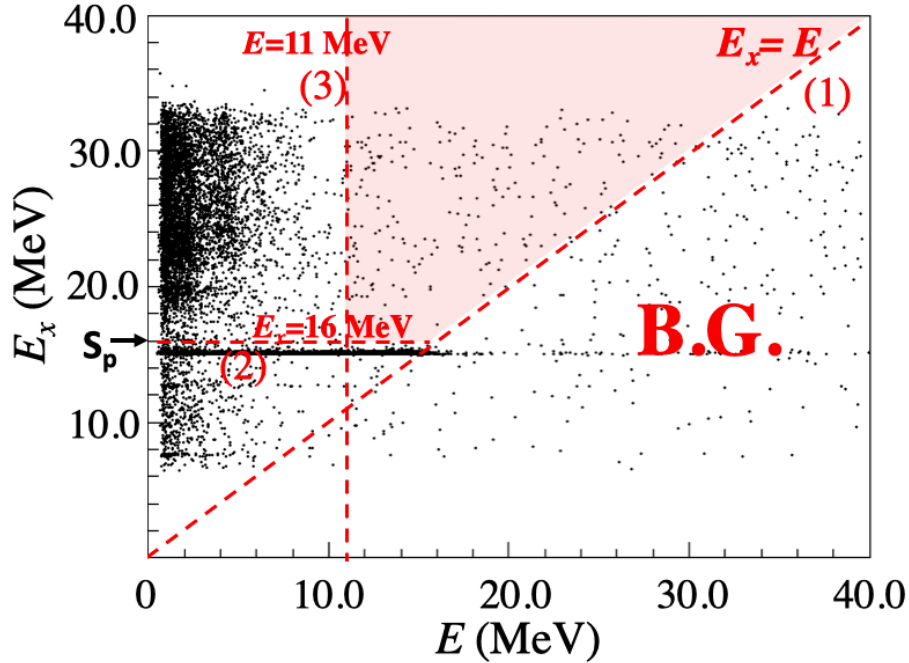


Fig. 3.6 Two-dimensional histogram with  $E_x$  at y axis and  $E$  (deposited  $\gamma$ -ray energy) at x axis.

A large number of events are observed at  $E_x = 15.1$  MeV. The events at the intersection of the lines  $E_x - E = 0$  and  $E_x = 15.1$  MeV are the  $\gamma$  rays decaying directly to the ground state with  $E_\gamma = 15.1$  MeV whereas the events at  $E_x - E < 0$  are the compton scattering of 15.1 MeV  $\gamma$  ray and the cascade  $\gamma$  rays.

The region with  $E_x > 16$  MeV marks the giant resonance region. All the events in the region  $E_x > 16$  MeV and  $E_x - E > 0$  are the  $\gamma$  rays from the giant resonances of  $^{12}\text{C}$ . As no  $\gamma$  rays with  $E > 11$  MeV are possible from the hadronic decays of giant resonances, the events in the region  $E > 11$  MeV and  $E_x - E > 0$  are the direct electromagnetic decays probably to the ground state of  $^{12}\text{C}$ .

### 3.3.1 Hadronic Decays

The  $\gamma$ -ray energy spectra ( $E < 11$  MeV) from the giant resonances were measured for various  $E_x$  values with a 2 MeV energy step. Figure 3.7 shows the measured  $\gamma$ -ray energy spectrum (black line) and the background spectrum (red line).

### 3.3.2 Electromagnetic Decays

The projection of two-dimensional plot shown in Fig. 3.6 over  $E$  axis for  $E_x > 16$  MeV is shown in Fig. 3.8. The events below  $E < 11$  MeV are the  $\gamma$  rays from hadronic decay of giant resonances and the events above  $E > 11$  MeV are the  $\gamma$  rays from electromagnetic decay of giant resonances. Hence, the events in the region (a)  $E_x > E$  (b)  $E_x > 16$  MeV and (c)  $E > 11$  MeV correspond to electromagnetic decays.

Electromagnetic decays can be studied more systematically using  $E_x - E$  plots where we plot the projection of 2-dimensional plot shown in Fig. 3.6 on  $E_x - E$  axis. One of the examples of direct electromagnetic decays is shown using 15.1 MeV state of  $^{12}\text{C}$ .  $E_x - E$  plot for 15.1 MeV state is shown in Fig. 3.9. The events at  $E_x - E$  correspond to direct decays to the ground state whereas the events at the positive side of  $E_x - E$  correspond to cascade  $\gamma$  rays and Compton scattering. The events at the negative side are the background events. Due to the resolution of the  $\gamma$ -ray detectors, the true signal starts from -2 MeV rather than zero. One of the main advantages of  $E_x - E$  projection is that it separates out the real signal (positive side) and the background (negative) regions whereas in the  $E$  projection both the real signal and background are mixed. The projection of electromagnetic decay region over  $E_x - E$  axis for giant resonance energy region is shown in Fig. 3.10. Figure 3.11 shows  $E_x - E$  plots for different  $E_x$  regions of giant resonances.

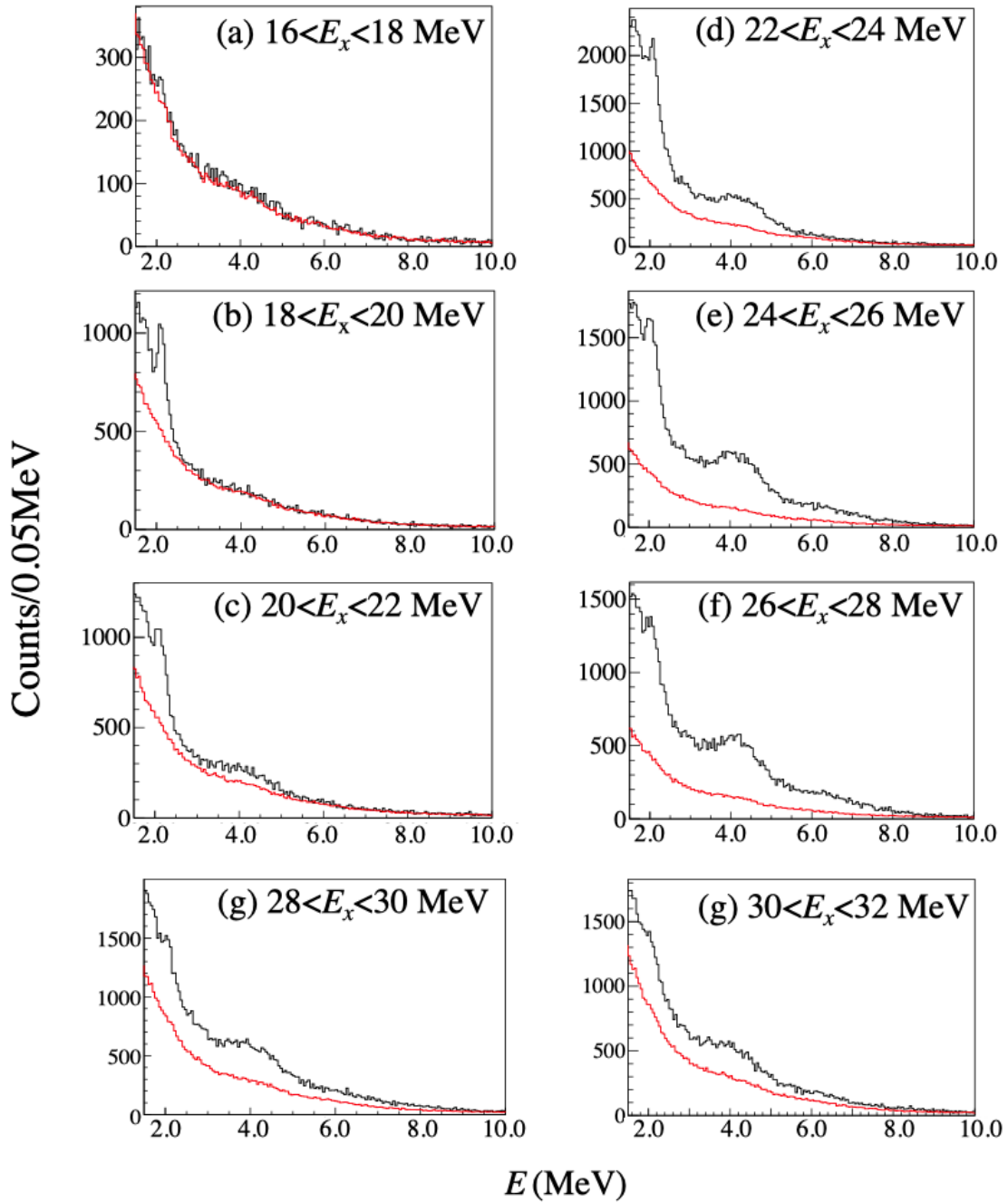


Fig. 3.7  $\gamma$ -ray energy spectrum (black) and background energy spectrum (red) from hadronic decays at various excitation energies in the giant resonance region of  $^{12}\text{C}$ .

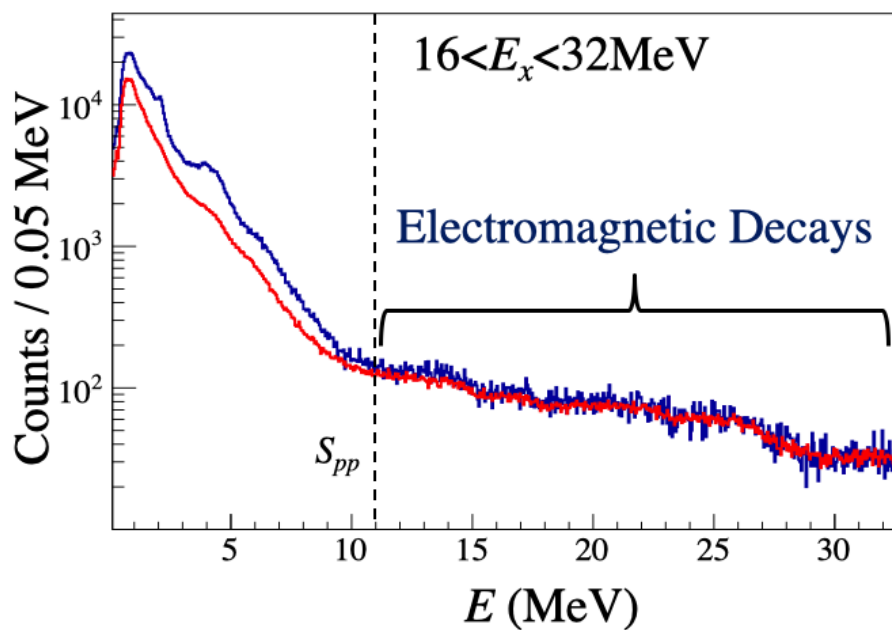


Fig. 3.8  $\gamma$ -ray energy spectrum (blue) and background energy spectrum for the giant resonance energy region ( $E_x > 16$  MeV) of  $^{12}\text{C}$ .

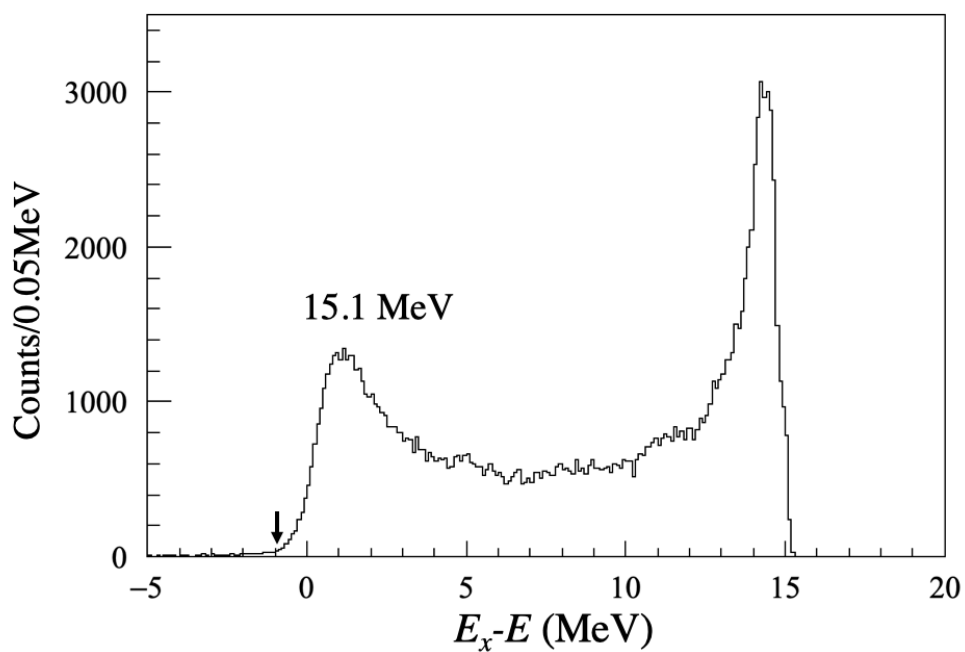


Fig. 3.9  $E_x - E$  spectrum (blue) for for 15.1 MeV after background subtraction.

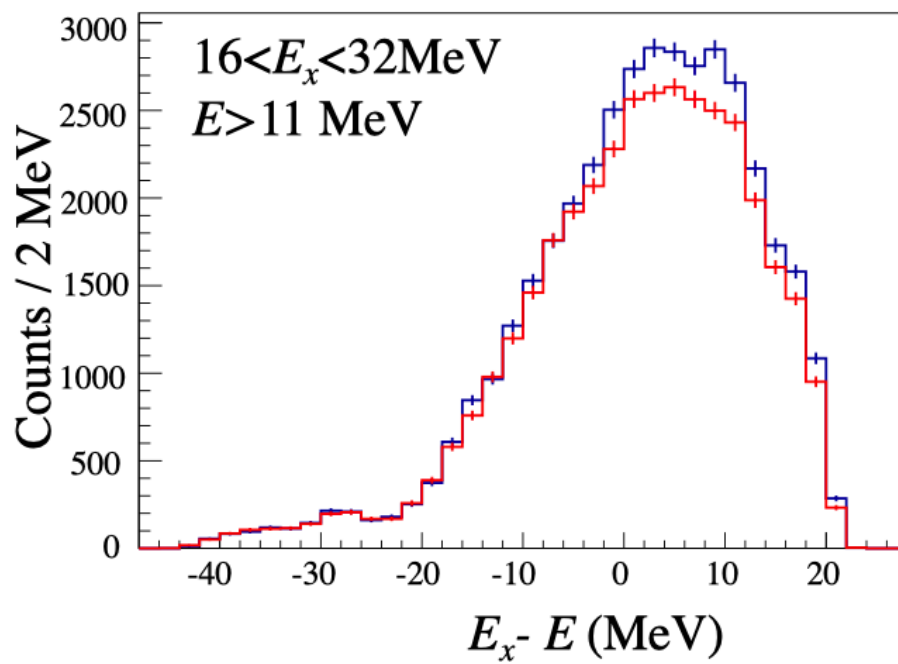


Fig. 3.10  $E_x - E$  spectrum (blue) and background spectrum (red) for the giant resonance energy region of  $^{12}\text{C}$  with  $E > 11$  MeV.

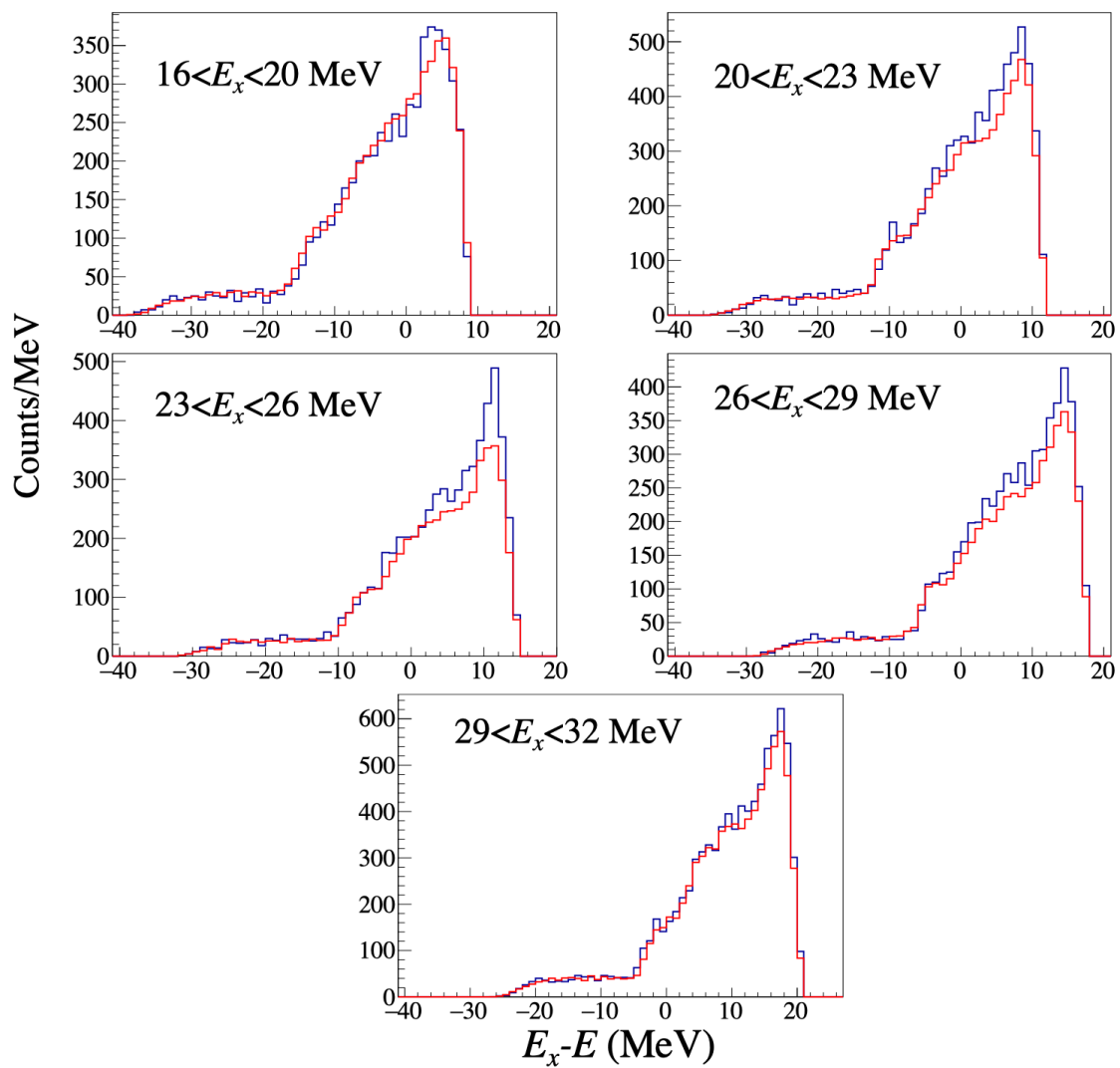


Fig. 3.11  $E_x - E$  spectra (blue) for different  $E_x$  regions with background spectra (red line).

# Chapter 4

## Discussion

### 4.1 Structure of giant resonances

We now discuss the energy spectra shown in Fig. 3.1 in more details. In a previous experiment [2], the polarization transfer (PT) observables were measured for  $^{12}\text{C}(p,p')$  at the same beam energy and  $0^\circ$  in the GR spectrometer, in which the excitation strengths were decomposed into a spin-flip part ( $\Delta S = 1$ ) and a non-spin-flip part ( $\Delta S = 0$ ). Fig. 4.3(a) shows the cross section  $d^2\sigma/d\Omega dE_x$  (solid line) the same as that in Fig. 3.1 and the spin-flip cross section  $\Sigma \cdot d^2\sigma/d\Omega dE_x$  (shaded region), where the total spin transfer  $\Sigma$  is unity for spin-flip transitions ( $\Delta S = 1$ ) and zero for non-spin-flip transitions ( $\Delta S = 0$ ). We used the  $\Sigma$  values measured in the previous experiment [2], whereas the cross sections  $d^2\sigma/d\Omega dE_x$  are our measurements. In the spin-flip cross section, excited states at  $E_x = 18.35, 19.4, 22-23,$  and  $25$  MeV were observed whereas the non-spin-flip cross section was dominated by broad resonances at  $E_x = 22-24$  and  $25-26$  MeV.

We now compare our  $\Sigma \cdot d^2\sigma/d\Omega dE_x$  (Fig. 4.3(a) shaded region) with the  $T = 1$  charge-exchange  $^{12}\text{C}(p,n)^{12}\text{N}$  spin-flip cross section measured at  $E_p = 296$  MeV [4], which is multiplied by a factor of 0.5 to account for the  $T = 1$  Clebsch-Gordan coefficients between the  $^{12}\text{C}(p,p')$  and  $^{12}\text{C}(p,n)^{12}\text{N}$  reactions. Moreover, the excitation energy was shifted for the case of the  $^{12}\text{C}(p,n)^{12}\text{N}$  reaction by 15.1 MeV.

The  $T = 1$  charge-exchange  $^{12}\text{C}(p,n)^{12}\text{N}$  spin-flip cross section was also measured at  $E_p = 135$  MeV by Anderson et al. [38] and both data agree within the given errors. Both observed resonances at  $E_x = 19.4$  ( $2^-$ ),  $22-23$  ( $2^-$ ), and  $25$  ( $1^-$ ) MeV. Our spin-flip cross sections (shaded region) agree with the  $T = 1$  charge-exchange spin-flip cross sections, except for a small disagreement in the region  $E_x = 18-19.4$  MeV. This obvious disagreement arises from the fact that our data also includes isoscalar resonance at  $E_x = 18.35$  MeV, which is not observed in the charge exchange reaction. This comparison primarily indicates that

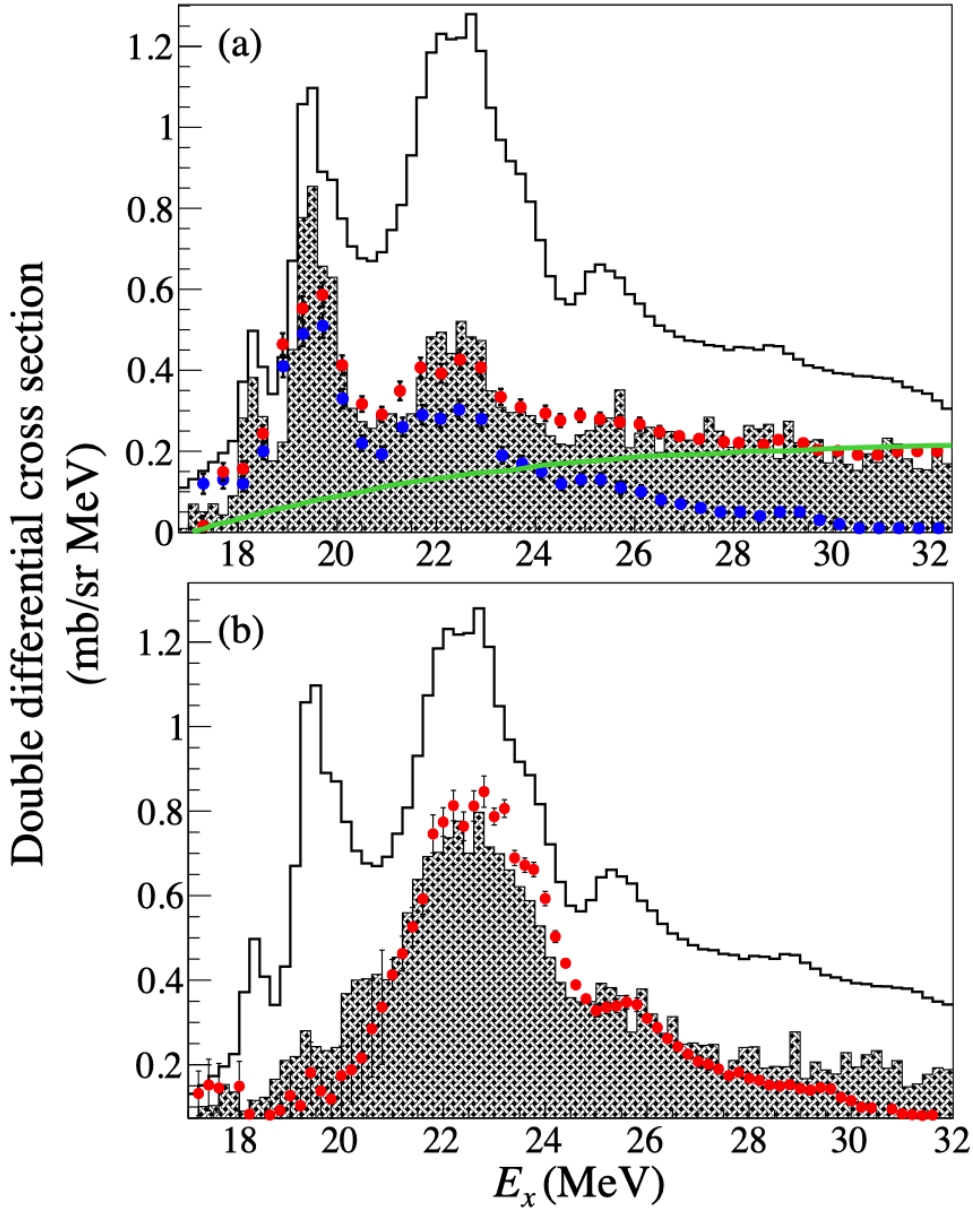


Fig. 4.1 (a) Spin flip component  $\Sigma \cdot d^2\sigma/d\Omega dE_x$  (shaded region) compared with  $d^2\sigma/d\Omega dE_x$  (black line). The spin flip cross section for  $^{12}\text{C}(p,n)^{12}\text{N}$  reaction (blue data points) and the contribution of quasifree process (green curve) to the spin flip cross section obtained from Ref. [4]. The sum of  $^{12}\text{C}(p,n)^{12}\text{N}$  spin flip cross section and quasifree contribution is shown by red data points. (b) Non spin flip component  $(1 - \Sigma) \cdot d^2\sigma/d\Omega dE_x$  (shaded region) compared with  $d^2\sigma/d\Omega dE_x$  (black line). The calculation of Coulomb excitation using the  $^{12}\text{C}(\gamma, \text{total})$  photo-absorption cross section (red points). The bin width is 0.2 MeV.

the  $(p, p')$  spin-flip cross sections are mostly dominated by the  $T = 1$  component, and the contribution of  $T = 0$  is small. Indeed, analysis of the effective interaction ( $V$ ) based on the  $N$ -

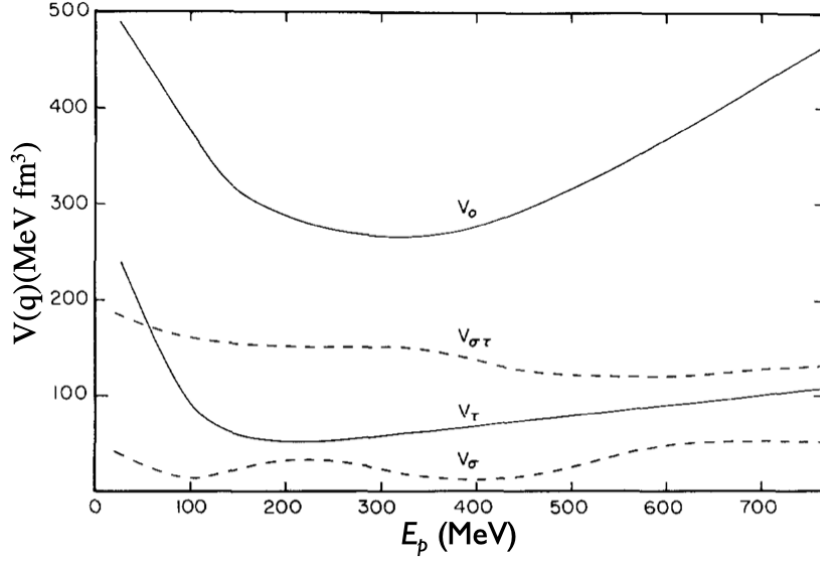


Fig. 4.2 Energy dependence of the effective nucleon-nucleon interaction for vanishing momentum transfer  $q \rightarrow 0$  [5, 6].

$N$  t-matrix using the experimentally observed nucleon-nucleus scattering over a wide energy range by Ref. [5, 6] suggests that the spin-isospin term ( $V_{\sigma\tau}$ ) in the effective interaction is independent of the beam energy in the range of 100-800 MeV and that the spin-isospin term ( $V_{\sigma\tau}$  ( $T = 1$ )) is much stronger than the spin term ( $V_{\sigma}$  ( $T = 0$ )) (Fig. 4.2). The isovector spin-flip excitations in  $^{12}\text{C}$  were also studied for ( $^6\text{Li}, ^6\text{Li}^*$ ) reaction [39].

Figure 4.3(b) shows the cross section  $d^2\sigma/d\Omega dE_x$  (solid line) and the non-spin-flip cross section  $(1 - \Sigma) \cdot d^2\sigma/d\Omega dE_x$  (shaded region). It was suggested in the  $^{16}\text{O}(p, p')$  experiment at the same beam energy (392 MeV) and  $0^\circ$  [3] that the forward non-spin-flip cross section may be related to the photo-absorption cross section. It is known that while non-spin-flip cross section is dominated by isovector giant dipole resonance ( $J^\pi = 1^-, T = 1$ ), the Coulomb excitations are dominated by  $E1$  transitions that favor non-spin-flip isovector  $J^\pi = 1^-$  excitations. It is interesting to compare these two cross sections in more detail.

We examined this feature using the latest calculation of the Coulomb excitation [40] in the forward ( $p, p'$ ) reaction, which is expressed in terms of the photo-nuclear absorption cross section for  $^{12}\text{C}(\gamma, total)$  [17]. In this calculation the equivalent virtual photon numbers are estimated using relativistic eikonal approximation given as

$$\frac{dn_{\pi l}}{d\Omega} = Z_1^2 \alpha \left( \frac{\omega k}{\gamma v} \right)^2 \frac{l[(2l+1)!!]^2}{(2\pi)^3(l+1)} \sum_m |G_{\pi lm}|^2 |\Omega_m(q)|^2, \quad (4.1)$$

where  $Z_1$  is the charge of the projectile,  $\alpha = e^2/\hbar c$ ,  $l$  denotes the transition multipolarity and  $G_{\pi lm}$  is the Winther-Alder relativistic function. Further, the Coulomb excitation cross section can be given as

$$\frac{d^2\sigma}{d\Omega dE_\gamma} = \frac{1}{E_\gamma} \sum_{\pi l} \frac{dn_{\pi l}}{d\Omega} \sigma_\gamma^{\pi l}, \quad (4.2)$$

where  $\sigma_\gamma^{\pi l}$  is the photo-nuclear absorption cross section with  $\pi$  as the mode of excitation—electric (E) or magnetic (M) and  $\Omega$  is the solid angle.

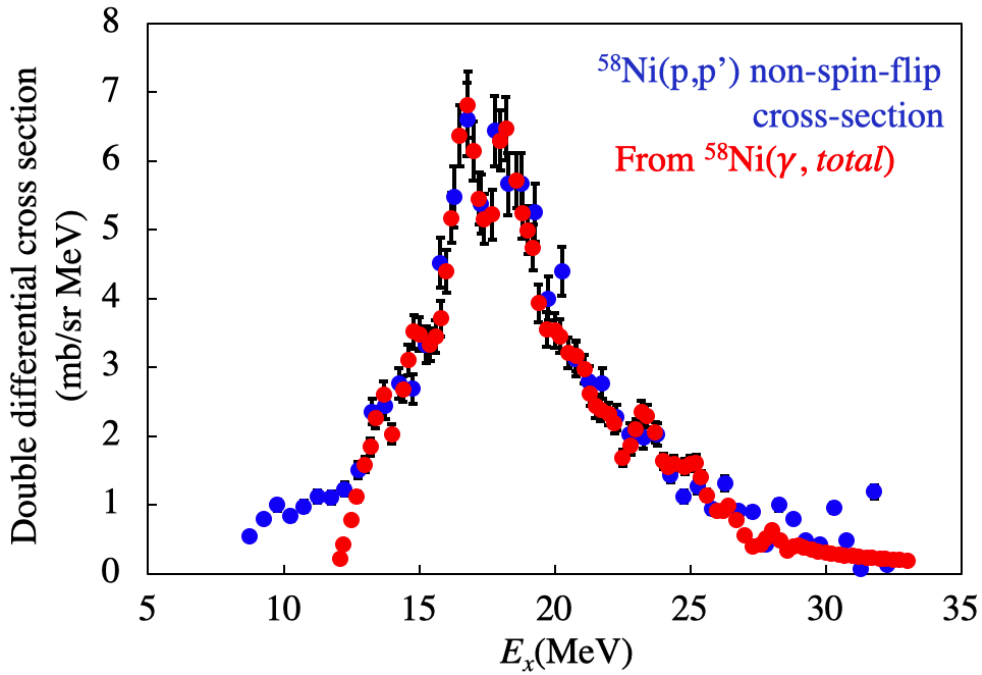


Fig. 4.3 (a) The comparison of non-spin flip cross section for  $^{58}\text{Ni}(p, p')$  (blue) with the calculation of Coulomb excitation using  $^{58}\text{Ni}(\gamma, \text{total})$  cross section.

	$T = 1$	$T = 1$
$\Delta S = 1$	Dominant	Negligible
$\Delta S = 0$	Dominant ( $1^-$ )	Negligible

Table 4.1 Contribution from different components to the total cross section for  $E_x = 16\text{-}32$  MeV .

The calculation of Coulomb excitations is shown in Fig. 4.3(b) and agrees fairly well with the non-spin-flip data, except for the low energy region  $E_x = 18\text{-}21$  MeV and the high energy region  $E_x > 30$  MeV. In the low energy region, our non-spin-flip data also includes isoscalar resonance at  $E_x = 20.5$  MeV which does not couple to the photo-absorption

process, hence the observed disagreement with the calculations. We also compared the calculation for Coulomb excitation with the non-spin-flip cross section for the  $^{58}\text{Ni}(p,p')$  reaction measured at  $0^\circ$  in RCNP [41] and found a good agreement within 10%. Other small isoscalar contributions to the non-spin-flip cross section of  $^{12}\text{C}$  for  $E_x > 25$  MeV were reported in a  $^{12}\text{C}(d,d')$  experiment [11] and a  $^{12}\text{C}(\alpha, \alpha')$  experiment [42, 43].

It is clearly seen that the energy region  $E_x = 16\text{-}32$  MeV consists of many overlapping resonances with different spin-parities and isospins. In order to unfold these resonances, we fit the cross section with known resonances [7] and a quasifree continuum. The resonances were assumed to have Lorentzian distributions and the quasifree cross section was assumed to have a smooth functional form as described in Ref. [44] (also shown in Fig. 4.3(a)). The overall fitting function was thus given as

$$f(E_x) = \sum_m \frac{\sigma_m}{1 + (E_x^2 - E_m^2)^2 / E_x^2 \Gamma_m^2} + \mu \cdot N \frac{1 - e^{[-(E_x - E_0)/T]}}{1 + [(E_x - E_{QF})/W_L]^2}, \quad (4.3)$$

where  $E_m$  and  $\Gamma_m$  are the peak energy and the resonance width, respectively, for the  $m^{\text{th}}$  resonance. Their values were taken from Ref. [7] and kept fixed during the fitting. The values of  $N$  (0.2 mb/sr MeV),  $E_{QF}$  (27 MeV),  $W_L$  (55 MeV),  $E_0$  (16 MeV), and  $T$  (6 MeV) were determined from fitting to the  $^{12}\text{C}(p,n)^{12}\text{N}$  cross section [4] and were kept fixed during this fit. The parameters  $\sigma_m$  (peak cross section) and  $\mu$  were determined to reproduce the data in the region of  $E_x = 18\text{-}32$  MeV and are tabulated in Table 4.2. The fit is shown in Fig. 4.4.

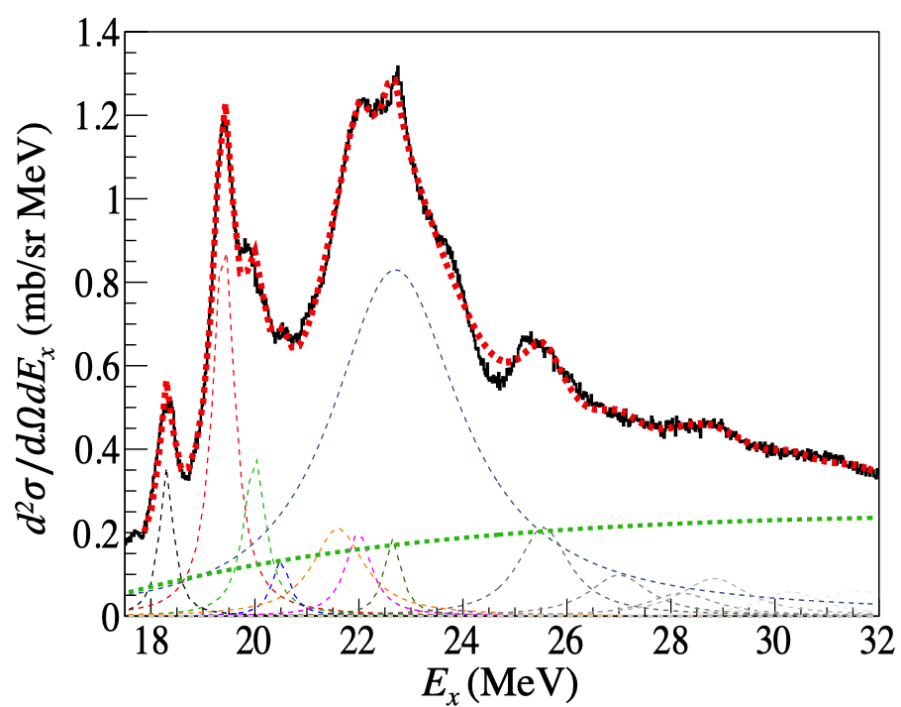


Fig. 4.4 Double differential cross section for the giant resonance region in  $^{12}\text{C}$  fitted with various resonances [7] and a quasifree continuum (green dotted curve). The red curve shows the overall fit obtained from the sum of all contributions.

$E_m$ (MeV)	$J^\pi; T$	$\Gamma_m$ (MeV)	$\sigma_m$ (mb/sr MeV)
18.35**	$2^-; 0$	$0.35 \pm 0.05$	$0.35 \pm 0.03$
19.40	$2^-; 1$	$0.49 \pm 0.03$	$0.90 \pm 0.05$
20.00	$2^+$	$0.38 \pm 0.10$	$0.39 \pm 0.04$
20.50**	$1^+; 0$	$0.30 \pm 0.05$	$0.15 \pm 0.03$
21.60	$2^+; 0$	$1.20 \pm 0.15$	$0.18 \pm 0.02$
21.99	$1^-; 1$	$0.61 \pm 0.11$	$0.19 \pm 0.06$
22.63*	$1^-; 1$	$0.40 \pm 0.04$	$0.84 \pm 0.11$
22.65	$1^-; 1$	$3.20 \pm 0.20$	$0.19 \pm 0.13$
23.52*	$1^-; 1$	$0.41 \pm 0.05$	$0.06 \pm 0.06$
23.99	$1^-; 1$	$0.57 \pm 0.12$	$0.04 \pm 0.01$
24.38	$2^+; 1$	$0.67 \pm 0.06$	$0.00 \pm 0.00$
24.41	-	$1.30 \pm 0.30$	$0.00 \pm 0.00$
24.90	-	$0.90 \pm 0.20$	$0.00 \pm 0.00$
25.30	$1^-; 1$	$0.51 \pm 0.10$	$0.19 \pm 0.04$
25.40	$1^-$	$2.00 \pm 0.20$	$0.00 \pm 0.00$
25.96	$2^+$	$0.70 \pm 0.20$	$0.14 \pm 0.02$
27.00	$1^-; 1$	$1.40 \pm 0.20$	$0.11 \pm 0.03$
28.20	$1^-; 1$	$1.60 \pm 0.20$	$0.06 \pm 0.01$
28.83	-	$1.54 \pm 0.09$	$0.09 \pm 0.01$
29.40	$2^+; 1$	$0.80 \pm 0.20$	$0.02 \pm 0.01$
30.29	$2^-; 1$	$1.54 \pm 0.09$	$0.04 \pm 0.01$
31.16	-	$2.10 \pm 0.15$	$0.07 \pm 0.01$
32.29	-	$1.32 \pm 0.23$	$0.01 \pm 0.01$
quasifree continuum	-	-	$\mu = 1.27 \pm 0.25$

Table 4.2 Resonance energy ( $E_m$ ), resonance width ( $\Gamma_m$ ), spin-parity, and isospin obtained from Ref. [7], and  $\sigma_m$  obtained from fit. \* $E_m$  and  $\Gamma_m$  were obtained from [9, 10]. \*\*Spin-parity and isospin were obtained from Ref. [11, 2].

$E_p$ (MeV)	$V$ (MeV)	$r_0$ (fm)	$a_0$ (fm)	$W_v$ (MeV)	$r'_0$ (fm)	$a'_0$ (fm)	$V_{LS}$ (MeV)	$r_{LS}$ (fm)	$a_{LS}$ (fm)	$W_{LS}$ (MeV)	$r'_{LS}$ (fm)	$a'_{LS}$ (fm)	$r_{0C}$
398	-2.51	1.08	0.48	21.6	1.13	0.64	3.21	0.93	0.57	-2.79	1.00	0.53	1.05

Table 4.3 Optical model parameters used in DWBA calculations taken from Ref. [8].

$E_x$ (MeV)	$J^\pi; T$	$b$ (fm)	$d_3p_1$	$d_3p_3$	$d_5p_3$	$s_1p_3$	$d_5p_1$	$p_1p_1$	$p_1p_3$	$p_3p_1$	$p_3p_3$
15.1 <sup>(a)</sup>	1 <sup>+</sup> ;1	1.86	-	-	-	-	-	-	-	-	-
								0.0581	0.6901	0.3394	0.0764
15.1 <sup>(b)</sup>	1 <sup>+</sup> ;1	1.86	-	-	-	-	-	0.0829	0.6701	0.2904	0.0841
19.4 <sup>(b)</sup>	2 <sup>-</sup> ;1	1.64	-	-	0.5415	0.3043	-	-	-	-	-
				0.0926			0.3047				
22.8 <sup>(b)</sup>	1 <sup>-</sup> ;1	1.64	-	0.1472	-	-	-	-	-	-	-
			0.1263		0.6874	0.2108					

Table 4.4 Transition matrix elements used in DWBA calculations. The superscript (a) denotes transition matrix elements from Cohen and Kurath [8] and (b) denotes matrix elements obtained from SFO Hamiltonian [12, 13]. The amplitude for the component  $l_i l_j$  represents an excitation from the  $l_j$  hole state to the  $l_i$  particle state. The subscripts on the single-particle orbitals represent the quantity  $2j$ . Here, the  $2s_{1/2}$  orbital is designated as  $s_1$ .

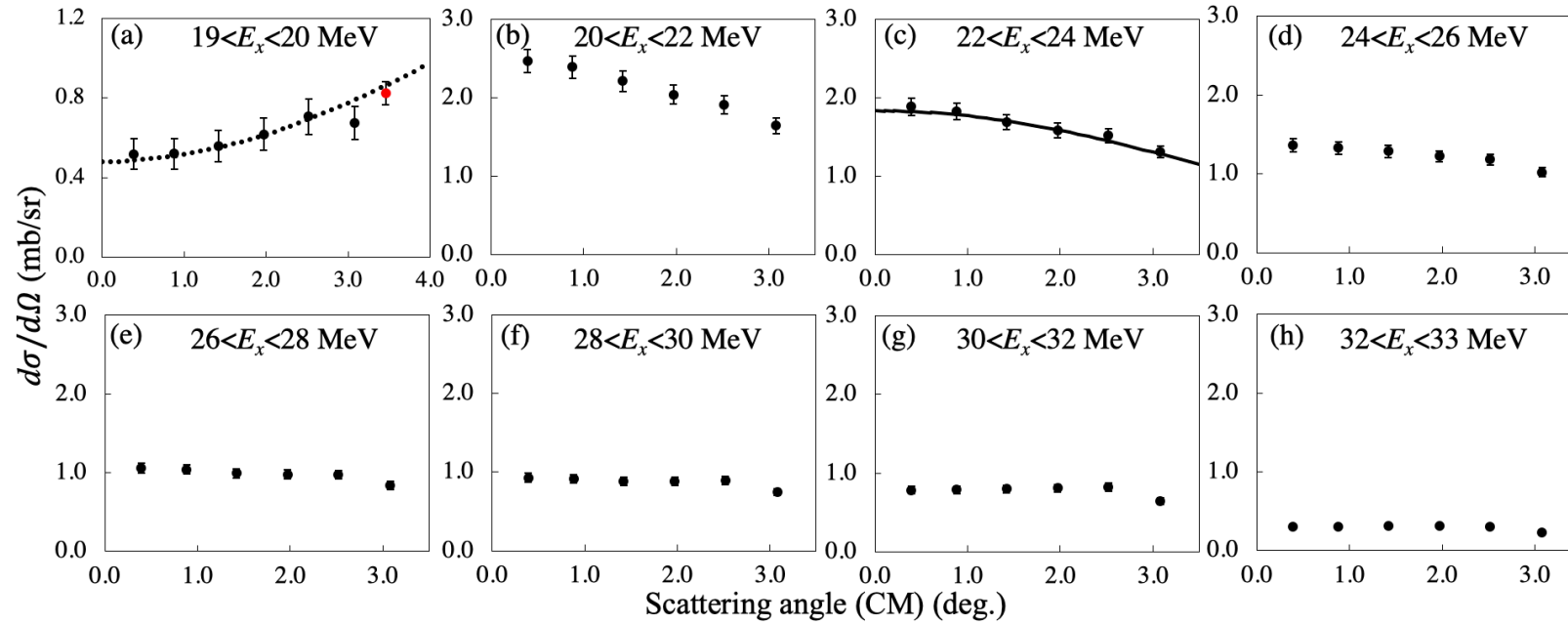


Fig. 4.5 Differential cross section as a function of scattering angle at various excitation energies in the giant resonance region of  $^{12}\text{C}$ . Dotted and solid black lines show the result of DWBA calculations (see text). (a) A data point (red) from another experiment [8] is also shown.

### 4.1.1 DWBA calculations

We also present the differential cross section for the  $^{12}\text{C}(p,p')$  reaction as a function of scattering angle in various  $E_x$  regions (Fig. 4.5). Some of the angular distributions were compared with DWBA calculations.

The DWBA calculations were performed using the program DWBA07 [45]. The single particle wave functions for the bound particles were of harmonic oscillator form. For the giant resonance region, the harmonic oscillator parameter  $b = 1.64$  fm was adopted [12]. The distorted wave was derived using an optical potential. The optical potential parameters were taken from Ref. [8], as determined from 398 MeV proton scattering from  $^{12}\text{C}$ , and are listed in Table 4.3. The effective  $NN$  interaction derived by Franey and Love [5] at  $E_p = 425$  MeV was used. The transition densities were obtained from shell model calculations using SFO Hamiltonians [12, 13] and are tabulated in Table 4.4.

In Fig. 4.3(a), it is clearly seen that the energy region  $E_x = 19$ -20 MeV is dominated by spin-flip cross section, and the data shown in Fig. 4.5(a) shows a clear angular dependence. The shape is well reproduced by the DWBA calculation results for the transitions to  $E_x = 19.4$  MeV ( $J^\pi = 2^-$ ,  $T = 1$ ; SDR). For the energy region  $E_x = 22$ -24 MeV, which is dominated by Coulomb excitations, the calculation results for the transitions to  $E_x = 22.8$  MeV ( $J^\pi = 1^-$ ,  $T = 1$ ; GDR) also reproduce the shape of angular distribution shown in Fig. 4.5(c). For  $E_x > 24$  MeV, no clear angular dependence was observed.

We also tested DWBA for the cross section calculations of the 15.1 MeV state. The harmonic oscillator parameter was chosen to match the prominent maxima of longitudinal and transverse form factors ( $F_L(q)$  and  $F_T(q)$ ) measured in a previous electron scattering experiment [46, 47]. Two types of transition densities were used for the calculations of the 15.1 MeV state (Table 4.4), the transition densities obtained from shell model calculations using SFO Hamiltonians [12, 13] and 1-p shell transition densities from Cohen and Kurath [8]. The comparison between calculations using these two different transition densities is shown in Fig. 3.2(a), along with the measured cross section. The dashed line represents the calculated cross section using transition densities from SFO Hamiltonians, and the solid line was obtained using Cohen and Kurath transition densities and scaled by a factor of 1.15 [8].

## 4.2 $\gamma$ rays from the giant resonances

### 4.2.1 Hadronic Decays

The  $\gamma$ -ray energy spectra from the giant resonances were measured for various  $E_x$  values with a 2 MeV energy step. Figure 3.7 (left) shows the measured  $\gamma$ -ray energy spectrum (black line) and the background spectrum (red line). The decay scheme of excited  $^{12}\text{C}$  is also shown.

As  $E_x$  reaches the proton separation energy ( $S_p = 16.0$  MeV), the  $^{12}\text{C}$  state decays hadronically to the ground state of  $^{11}\text{B}$  by emitting a proton. No  $\gamma$ -ray emission is possible until  $E_x$  exceeds the threshold ( $S_p + 2.1 = 18.1$  MeV) for proton decay to the first excited state of  $^{11}\text{B}^*(2.1$  MeV). This feature was confirmed experimentally as no  $\gamma$  rays were observed from the region  $E_x = 16$ -18 MeV (shown in Fig. 3.7(a)). The same feature can be seen in Fig. 3.7(b) where we observed only a 2.1 MeV  $\gamma$  ray, as the 2.1 MeV state of  $^{11}\text{B}$  is the only energetically accessible state at  $E_x = 18$ -20 MeV. As  $E_x$  reaches 21 MeV, it can decay to the 2<sup>nd</sup> (4.4 MeV) and 3<sup>rd</sup> (5.0 MeV) excited states of  $^{11}\text{B}$  or to the first excited state of  $^{11}\text{C}^*(2.0$  MeV),  $S_n + 2.0 = 20.7$  MeV after neutron emission ( $S_n = 18.7$  MeV). As a result, we observed nearly doubled  $\gamma$ -ray emission rate in Fig. 3.7(c). With increasing  $E_x$ , the larger  $\gamma$ -ray emission rate and higher energy  $\gamma$  rays were observed until the excitation energy reached 27.2 MeV, which is the separation energy of daughter nuclei  $^{11}\text{B}$  ( $S_{p'} = 11.2$  MeV) and  $^{11}\text{C}$  ( $S_{p'} = 8.7$  MeV). For  $E_x > 27.2$  MeV, the  $^{12}\text{C}$  state can decay via 3-body decay to lighter nuclei. As far as hadronic decays are concerned, no  $\gamma$  rays with  $E_\gamma > 11$  MeV were observed<sup>1</sup>. These features agree qualitatively with the theoretical predictions of Langanke et al. [24], who stated that the  $\gamma$  rays from the giant resonances are emitted from excited states of daughter nuclei after hadronic decay. We will further analyze the  $\gamma$ -ray emissions quantitatively.

In order to obtain the  $\gamma$ -ray emission probability from the giant resonances of  $^{12}\text{C}$ , we fit the data with  $\gamma$ -ray response functions generated for the excited states of daughter nuclei, which can be defined as

$$P_i(E) = b_0 \cdot P(E_\gamma^i; E) + \sum_{j=1} b_j \cdot P(E_\gamma^i - E_\gamma^j, E_\gamma^j; E), \quad (4.4)$$

where  $P_i(E)$  is the response function for the  $i^{\text{th}}$  state of the daughter nuclei at energy  $E^i$ ,  $b_0$  is the probability for the  $i^{\text{th}}$  state to decay directly to the ground state by emitting a  $\gamma$  ray of energy  $E_\gamma^i$ , and  $b_j$  is the probability for the  $i^{\text{th}}$  state to decay to a lower energy state ( $E^j$ ) by emitting a  $\gamma$  ray of energy  $E_\gamma^i - E_\gamma^j$  and then decay to the ground state by emitting a  $\gamma$  ray of

<sup>1</sup>The study of electromagnetic decay of giant resonances in  $^{12}\text{C}$ , emitting  $\gamma$  rays of  $E_\gamma > 11$  MeV, will be reported elsewhere.

energy  $E_\gamma^j$ . For example, the first and the second excited states of  $^{11}\text{B}$  decay directly to the ground state, emitting single  $\gamma$  rays with energies of 2.12 and 4.4 MeV, respectively, with  $b_0 = 1.0$ . Hence, their response functions are given as  $P(2.12 \text{ MeV}; E)$  and  $P(4.4 \text{ MeV}; E)$ . The third excited state of  $^{11}\text{B}$  decays to the ground state by emitting a 5.02 MeV  $\gamma$  ray with a probability of 0.85 ( $b_0$ ) and to the 2.12 MeV state by emitting a 2.9 MeV  $\gamma$  ray ( $5.02 - 2.12 \text{ MeV}$ ) with a probability of 0.15 ( $b_1$ ) followed by further decay to the ground state by the emission of a 2.12 MeV  $\gamma$  ray. The response function for this state is given as  $0.85 \cdot P(5.0 \text{ MeV}; E) + 0.15 \cdot P(2.9, 2.12 \text{ MeV}; E)$ . Similarly, the response functions for all of the other excited states of daughter nuclei ( $^{11}\text{B}$  and  $^{11}\text{C}$ ) were generated using the  $\gamma$  emission probability ( $b_0$  and  $b_j$ ) given in Ref. [23] and are listed in Table 4.6. Once all of the response functions are generated, the efficiency ( $\eta_i$ ) for the detection of  $\gamma$  rays emitted from the  $i^{\text{th}}$  state of a daughter nucleus can be given as

$$\int_{E_{th}}^{E_{max}} P_i(E) dE = \eta_i. \quad (4.5)$$

The total  $\gamma$ -ray emission probability in each  $E_x$  region of  $^{12}\text{C}$  can be written as

$$R_\gamma(E_x) = \frac{\sigma_{p,p'\gamma}}{\sigma_{p,p'}} = \frac{N_\gamma^0}{N_{E_x}}, \quad (4.6)$$

where  $N_{E_x}$  is the total number of excited states of  $^{12}\text{C}$  in that  $E_x$  region and  $N_\gamma^0$  is the total number of  $\gamma$  rays emitted from these states. The contribution from the individual excited states ( $r_i$ ) of daughter nuclei (after particle decay) to the total  $\gamma$ -ray emission probability can be given as

$$r_i = \frac{N_i^0}{N_{E_x}} = \frac{N_i/\eta_i}{N_{E_x}}, \quad (4.7)$$

where  $N_i^0$  is the total number of  $\gamma$  rays emitted from the  $i^{\text{th}}$  state of a daughter nucleus from the target and  $N_i$  is the number of events detected. The quantity  $r_i$  can also be interpreted as the probability for  $^{12}\text{C}$  excited at  $E_x$  to decay to the  $i^{\text{th}}$  state of a daughter nuclei and emit a  $\gamma$  ray. Furthermore,  $r_i$  can be decomposed as

$$r_i = C_{GR} \cdot \tilde{r}_i + C_{QF} \cdot r_{QF}^i, \quad (4.8)$$

where  $C_{GR}$  and  $C_{QF}$  are the fractions of giant resonances (GR) and quasifree (QF) cross section in the total cross section obtained from Eq. (4.3), with

$$C_{GR} + C_{QF} = 1. \quad (4.9)$$

$\tilde{r}_i$  is the probability of giant resonances decaying to the  $i^{th}$  excited state of daughter nucleus and  $r_{QF}^i$  is the probability of daughter nucleus to be in the  $i^{th}$  excited state after quasifree knockout. The measured  $\gamma$ -ray spectrum ( $N_\gamma(E)$ ) in each  $E_x$  region can be expressed as

$$N_\gamma(E) = N_{E_x} \sum_i r_i \cdot P_i(E) + \alpha \cdot N_{bg}(E). \quad (4.10)$$

Alternatively, this can be written as

$$N_\gamma(E) = N_{E_x} [C_{GR} \sum_i \tilde{r}_i \cdot P_i(E) + C_{QF} \sum_j r_{QF}^j \cdot P_j(E)] + \alpha \cdot N_{bg}(E), \quad (4.11)$$

where  $N_{bg}(E)$  and  $N_{E_x}$  are the background spectrum and the number of excitation events, respectively. The quantities  $r_i$  and the background normalization factor ( $\alpha$ ) were set as free parameters in the fit.

The probability ( $r_{QF}^j$ ) after quasifree nucleon knockout can be obtained as follows. A proton knockout from the  $1p$  shell of  $^{12}\text{C}$  leads to the  $3/2^-$  ground state, the  $1/2^-$  state at 2.1 MeV, and the  $3/2^-$  state at 5.02 MeV in  $^{11}\text{B}$ . The spectroscopic factors for  $1p$  and  $1s$  knockout from  $^{12}\text{C}$  were experimentally determined from  $^{12}\text{C}(e, e'p)$  data and are listed in Ref. [48, 49]. Using  $1p$  spectroscopic factors, the probabilities for daughter nucleus ( $^{11}\text{B}$ ) to be in 2.1 MeV and 5.02 MeV states were estimated to be ( $r_{QF}^{2.12} =$ ) 4% and ( $r_{QF}^{5.02} =$ ) 3%, respectively. It should be noted that for  $E_x < 21$  MeV, only the 2.1 MeV state is energetically accessible with a probability of 4%, but as  $E_x$  exceeds 21 MeV, the 5.02 MeV state is also accessible. Similarly, a neutron knockout can also occur with equal probability and will lead to almost the same  $\gamma$ -ray response as that from a proton knockout. The only difference is that the threshold for neutron knockout is greater than that for proton knockout by 2.7 MeV. For  $E_x > 27.2$  MeV,  $1s$  nucleon knockout can also occur. Using  $1s$  spectroscopic factors and statistical model calculations (described in the next section), the  $\gamma$ -ray emission probability was also estimated and the  $\gamma$ -ray response function from quasifree processes are shown in Table 4.5.

$E_x$ region (MeV)	$\sum_j r_{QF}^j \cdot P_j(E)$
18-21	$0.5 \cdot (0.04 \cdot P(2.12\text{MeV}; E))$
21-24	$0.5 \cdot (0.04 \cdot P(2.12\text{ MeV}; E) + 0.03 \cdot P(5.02\text{MeV}; E))$ $+ 0.5 \cdot (0.04 \cdot P(2.0\text{MeV}; E))$
24-32	$0.5 \cdot (0.04 \cdot P(2.12\text{ MeV}; E) + 0.03 \cdot P(5.02\text{MeV}; E))$ $+ 0.5 \cdot (0.04 \cdot P(2.0\text{MeV}; E) + 0.03 \cdot P(4.8\text{MeV}; E))$

Table 4.5  $\gamma$ -ray response function from quasifree processes for different excitation energies.

Although 2.9 MeV  $\gamma$  rays are expected from the decay of several states (5.02, 7.28 MeV, etc) and is included in their response functions, we found that an independent response function for 2.9 MeV must be added to Eq. (4.15) to obtain a good fit. Furthermore, during the fit, 6.74 MeV ( $7/2^-$ ) and 6.79 MeV ( $1/2^+$ ) states of  $^{11}\text{B}$  and 6.48 MeV ( $7/2^-$ ) and 6.34 ( $1/2^+$ ) states of  $^{11}\text{C}$  were merged because these states lie close to each other and have the same  $\gamma$ -ray response function. Some of the fitted spectra are shown in Fig. 4.6.

The total  $\gamma$ -ray emission probability in different  $E_x$  regions can be given as

$$R_\gamma(E_x) = \sum_i r_i = C_{GR} \sum_i \tilde{r}_i + C_{QF} \sum_j r_{QF}^j, \quad (4.12)$$

This can be equivalently written as

$$R_\gamma(E_x) = \frac{(N_\gamma - N_{bg})/\bar{\eta}}{N_{E_x}}. \quad (4.13)$$

where  $N_\gamma$ ,  $N_{bg}$ , and  $N_{E_x}$  are the number of  $\gamma$ -ray events, background events, and excitation events, respectively, and  $\bar{\eta}$  is the weighted average efficiency in a particular  $E_x$  region and  $\bar{\eta}$  is given as

$$\begin{aligned} \bar{\eta} &= \frac{1}{\sum_i r_i} \sum_i r_i \cdot \eta_i \\ &= \frac{1}{C_{GR} \sum_i \tilde{r}_i + C_{QF} \sum_j r_{QF}^j} \left( C_{GR} \sum_i \tilde{r}_i \cdot \eta_i + C_{QF} \sum_j r_{QF}^j \cdot \eta_j \right). \end{aligned} \quad (4.14)$$

The total  $\gamma$ -ray emission probability and the probability ( $r_i$ ) obtained from the fit are shown in Table 4.7 for all  $E_x$  regions.

Energy state ( $^{11}\text{B}$ )(MeV)	$\gamma$ -ray energy (MeV)(Prob.)	Energy state ( $^{11}\text{C}$ ) (MeV)	$\gamma$ -ray energy (MeV)(Prob.)
2.12	2.12 (1.0)	2.00	2.00 (1.0)
4.44	4.44 (1.0)	4.32	4.32 (1.0)
5.02	5.02 (0.85) 2.89 (0.15) 2.12 (0.15)	4.80	4.80 (0.85) 2.80 (0.15) 2.00 (0.15)
6.79	6.79 (0.68) 4.66 (0.28) 2.12 (0.28) 1.77 (0.04) 5.02 (0.04)	6.34	6.34 (0.67) 4.33 (0.33) 2.00 (0.33)
7.28	7.28 (0.88) 2.84 (0.05) 4.44 (0.05) 2.26 (0.07) 5.02 (0.07)	6.90	6.90 (0.92) 2.58 (0.04) 4.32 (0.04) 2.10 (0.04) 4.80 (0.04)
7.97	7.97 (0.43) 5.85 (0.49) 2.12 (0.49) 0.69 (0.08) 7.28 (0.08)	7.49	7.49 (0.36) 4.49 (0.64) 2.00 (0.64)
8.56	8.56 (0.56) 6.43 (0.30) 2.12 (0.30) 4.11 (0.05) 4.44 (0.05) 3.54 (0.09) 5.02 (0.09)	8.10	8.10 (0.74) 6.10 (0.26) 2.00 (0.26)
8.92	8.92 (0.95) 4.47 (0.05) 4.44 (0.05)	8.42	8.42 (1.0)
9.27	9.27 (0.18) 4.83 (0.70) 4.44 (0.70) 2.53 (0.12) 6.74 (0.12)	9.20	9.20 (0.74) 6.47 (0.20) 2.72 (0.20) 4.88 (0.13) 4.31 (0.13)

Table 4.6 Energy states of daughter nuclei used for fitting, and cascade  $\gamma$  rays emitted from them with their respective emission probabilities (given in parentheses).

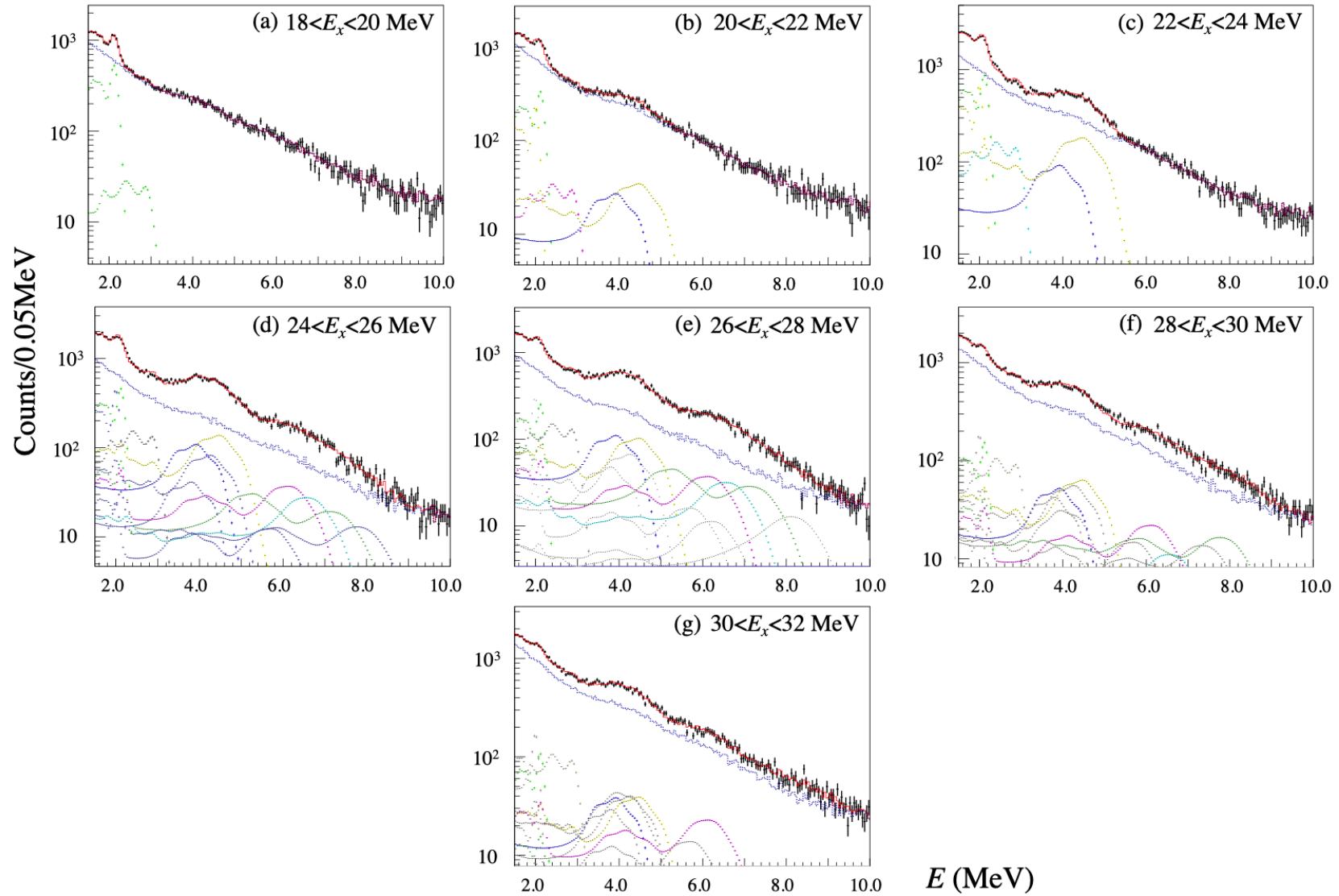


Fig. 4.6 The  $\gamma$ -ray spectrum (black data points), background spectrum (light blue line), total fit (red line), and  $\gamma$  rays from the excited states of daughter nuclei (colored dotted lines) are shown for various  $E_x$  regions.

Decay Scheme	Energy state (MeV) ( $J^\pi$ )	$^{12}\text{C}$ Excitation Energy ( $E_x$ ) (MeV)						
		18-20	20-22	22-24	24-26	26-28	28-30	30-32
		$r_i$ [%]						
$^{11}\text{B}+\text{p}$ ( $S_p=16.0$ MeV)	2.12 (1/2 <sup>-</sup> )	7.5(2)	3.8(2)	8.5(2)	7.4(3)	4.9(3)	2.6(3)	2.1(4)
	4.44 (5/2 <sup>-</sup> )	-	0.7(2)	2.0(2)	4.9(3)	5.0(3)	2.6(7)	1.1(4)
	5.02 (3/2 <sup>-</sup> )	-	0.8(2)	4.6(2)	5.4(3)	5.1(4)	3.2(9)	0.7(5)
	6.79 (1/2 <sup>+</sup> )	-	-	-	3.4(4)	2.3(5)	2.4(7)	1.8(4)
	7.28 (5/2 <sup>+</sup> )	-	-	-	1.1(4)	1.8(3)	0.6(3)	0.4(3)
	7.97 (3/2 <sup>+</sup> )	-	-	-	2.4(5)	3.9(5)	-	-
	8.56 (3/2 <sup>-</sup> )	-	-	-	1.1(3)	-	2.3(6)	0.8(2)
	8.92 (5/2 <sup>-</sup> )	-	-	-	-	1.0(1)	0.4(9)	-
	9.27 (5/2 <sup>+</sup> )	-	-	-	-	-	1.0(9)	3.7(7)
$^{11}\text{C}+\text{n}$ ( $S_n=18.7$ MeV)	2.00 (1/2 <sup>-</sup> )	-	2.2(1)	5.5(1)	5.7(2)	4.9(3)	2.7(3)	2.1(4)
	4.32 (5/2 <sup>-</sup> )	-	-	-	1.0(1)	2.5(2)	2.6(7)	1.1(4)
	4.80 (3/2 <sup>-</sup> )	-	-	-	3.0(2)	3.4(3)	2.6(8)	0.6(5)
	6.34 (1/2 <sup>+</sup> )	-	-	-	-	1.1(2)	0.8(2)	1.8(4)
	6.90 (5/2 <sup>+</sup> )	-	-	-	-	1.8(3)	0.6(3)	0.4(3)
	7.49 (3/2 <sup>+</sup> )	-	-	-	-	-	-	-
	8.10 (3/2 <sup>-</sup> )	-	-	-	-	-	1.2(3)	0.8(2)
	8.42 (5/2 <sup>-</sup> )	-	-	-	-	-	-	-
9.20 (5/2 <sup>+</sup> )	-	-	-	-	-	0.1(2)	0.4(1)	
quasifree	2.12 (1/2 <sup>-</sup> )	0.3(1)	0.9(2)	0.8(2)	1.5(3)	1.9(3)	2.3(3)	2.8(5)
	5.02 (3/2 <sup>-</sup> )	-	0.3(1)	0.3(1)	1.1(2)	1.4(2)	1.7(2)	2.1(5)
	2.9	0.7(2)	0.7(2)	2.8(2)	4.4(3)	5.4(4)	4.1(5)	4.3(5)
$R_\gamma$ (%)		8.2±0.5	11.3±0.7	27.7±1.6	43.9±2.4	47.9±2.6	32.4±1.9	26.0±1.6

Table 4.7 The probability ( $r_i$ ) obtained from the fit and the total  $\gamma$ -ray emission probability ( $R_\gamma$ ). Numbers in parentheses represent the error in the least significant digit.

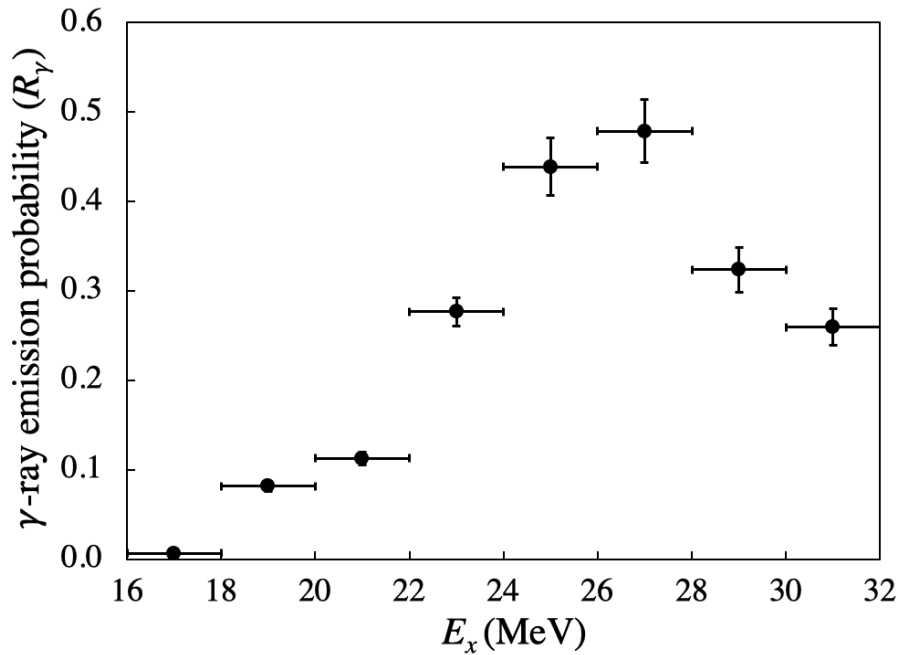


Fig. 4.7 The total  $\gamma$ -ray emission probability ( $R_\gamma$ ) as a function of  $E_x$  with systematic errors.

The  $\gamma$ -ray emission probability ( $R_\gamma$ ) as a function of excitation energy ( $E_x$ ) is shown in Fig. 4.7 along with both statistical and systematic errors. The systematic uncertainties include errors in the determination of excitation events,  $\gamma$ -ray background subtraction, and detection efficiency. The errors due to statistical uncertainty were 0.3-0.5%. The  $\gamma$ -ray emission probability increases with the increasing excitation energy starting, from zero at  $E_x = 16$  MeV and reaching a maximum value of  $47.9 \pm 0.5\% \pm 3.5\%$  at  $E_x = 27$  MeV, where the first and second uncertainties are statistical and systematic, respectively. After the 3-body decay threshold is reached, the emission probability gradually decreases with the increasing excitation energy. The most dominant contributions to the emission probability come from the 2.1 and 2.0 MeV states (first excited states of  $^{11}\text{B}$  and  $^{11}\text{C}$ , respectively). At higher excitation energies, the contributions from the higher energy states of daughter nuclei also become significant, as expected qualitatively.

The  $\gamma$ -ray emission probability was also measured as a function of scattering angle for different  $E_x$  regions and no strong angular dependence was observed (Fig. 4.8).

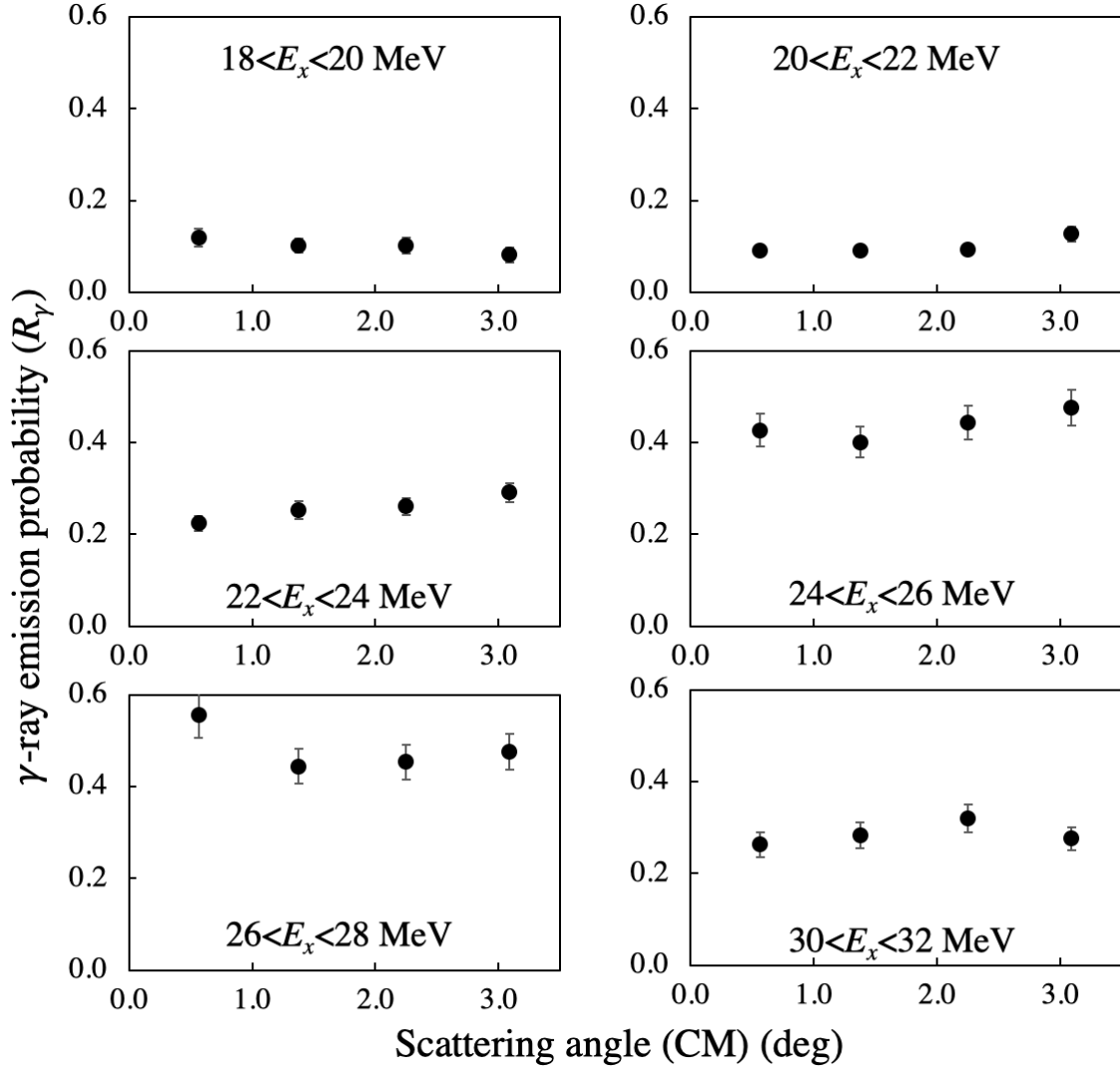


Fig. 4.8  $\gamma$ -ray emission probability as a function of scattering angle at various excitation energies in the giant resonance region of  $^{12}\text{C}$ .

#### 4.2.2 Statistical model calculations

Using the spin-parity information from Table 4.2, the calculated  $\gamma$ -ray spectrum  $N_{\gamma}^{calc.}(E)$  from  $^{12}\text{C}^*$  in different  $E_x$  regions can be given as

$$N_{\gamma}^{calc.}(E) = N_{E_x} \left[ C_{GR} \sum_i \tilde{c}_i \cdot P_i(E) + C_{QF} \sum_j r_{QF}^j \cdot P_j(E) \right] + \alpha \cdot N_{bg}(E). \quad (4.15)$$

The calculated  $\gamma$ -ray emission probability  $R_{\gamma}^{calc.}(E_x)$  can be determined as

$$R_{\gamma}^{calc.}(E_x) = C_{GR} \sum_i \tilde{c}_i + C_{QF} \sum_j r_{QF}^j. \quad (4.16)$$

$E_x$ (MeV)	2-body decay		3-body decay		Quasifree process	
	$C_{GR}^{2-body}$	$\sum \tilde{c}_i (i < S_p)$	$C_{GR}^{3-body}$	$\sum \tilde{c}_i (i > S_p)$	$C_{QF}$	$\sum r^{QF}$
18-20	0.85	0.06	0.00	0.00	0.15	0.02
20-22	0.83	0.25	0.00	0.00	0.17	0.06
22-24	0.83	0.44	0.00	0.00	0.17	0.06
24-26	0.69	0.62	0.00	0.00	0.31	0.07
26-28	0.56	0.74	0.00	0.00	0.44	0.07
28-30	0.48	0.75	0.00	0.00	0.52	0.07
30-32	0.32	0.58	0.06	0.01	0.62	0.08

Table 4.8 Contributions from the 2-body decay, 3-body decay and quasifree process along with calculated  $\gamma$ -ray emission probability.

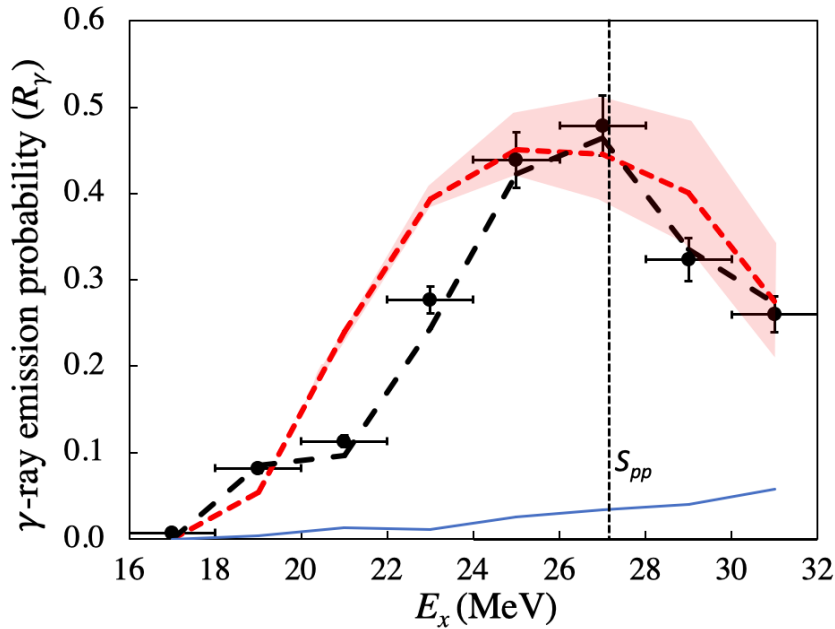


Fig. 4.9 Comparison between the measured  $\gamma$ -ray emission probability (data points) and the statistical model prediction (black dashed line). The red dashed line shows the  $\gamma$ -ray emission probability obtained from the fit using Eq. (4.12). The  $\gamma$ -ray emission probability from quasifree process (blue line) is also shown. The quantity  $S_{pp}$  represents two proton emission threshold (27.2 MeV) for  $^{12}\text{C}$ .

The main contribution to the total  $\gamma$ -ray emission probability ( $R_\gamma^{calc}$ ) comes from the decay of giant resonances. For  $E_x = 16-27$  MeV,  $R_\gamma^{calc}$  increases because  $C_{GR}$  dominates in this energy region and the number of accessible states of daughter nuclei also increases. For  $E_x > 27$  MeV,  $C_{GR}$  begins to decrease and so does the  $\gamma$ -ray emission probability, while the contribution of  $C_{QF}$  becomes nearly equal to  $C_{GR}$ . The red band in the Fig. 4.12 shows the uncertainty in the calculation due to the uncertainty of  $C_{GR}$  and  $C_{QF}$ .

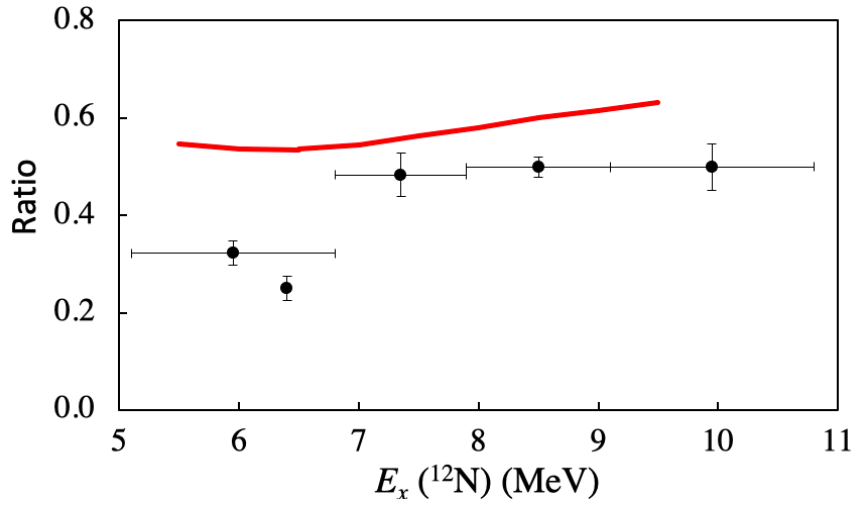


Fig. 4.10 Comparison between the measured ratio ( $\sigma_{^{11}\text{C}(1^{st})}/\sigma_{^{11}\text{C}(g.s.)}$ ) (black data points) and calculated ratio ( $\tilde{c}_{^{11}\text{C}(1^{st})}/\tilde{c}_{^{11}\text{C}(g.s.)}$ ) (red line).

The statistical model calculations predicted a higher decay probability to the excited states by 30-40% as compared to the measured values in the energy region  $E_x = 20$ -24 MeV. The same feature was observed, when we compared calculations with the measurement of  $^{12}\text{C}(\gamma, total)$  and  $^{12}\text{C}(\gamma, n_0)$  cross sections [17].

For  $E_x > 27.2$  MeV, the 3-body decay threshold is reached, and the decay involving two-nucleon emission ( $p + p + ^{10}\text{Be}$ ) also starts. Although the decay via 3-body process was significant ( $\approx 6\%$ ), it gave negligible contribution ( $< 1\%$ ) to the  $\gamma$ -ray emission probability.

The statistical model was also used to calculate the decay probability of  $^{12}\text{N}(E_x, J^\pi = 1^-)$  to the ground state and the first excited state of  $^{11}\text{C}$  after proton decay. Furthermore, these calculations were compared with data obtained from Ref. [50], where the author measured the reaction cross section for  $^{12}\text{N}^* \rightarrow p + ^{11}\text{C}$  (ground state or  $1^{st}$  excited state). The comparison of the measured ratio ( $\sigma_{^{11}\text{C}(1^{st})}/\sigma_{^{11}\text{C}(g.s.)}$ ) with the calculated ratio ( $\tilde{c}_{^{11}\text{C}(1^{st})}/\tilde{c}_{^{11}\text{C}(g.s.)}$ ) is shown in Fig. 4.10. The higher value of the calculated ratio implies that statistical model predicts higher decay probability to the  $1^{st}$  excited state.

### 4.2.3 Electromagnetic Decays

For the analysis  $\gamma$  rays from the electromagnetic decays several  $\gamma$ -ray response functions were generated with different  $E_\gamma^i$  where  $i$  stands for different  $\gamma$ -ray energy running from 16 to 32 MeV. The efficiency for the  $i^{th}$   $\gamma$  ray can be written as

$$\eta_i = \int_{11 \text{ MeV}}^{E_{max}} P(E_\gamma^i; E) dE. \quad (4.17)$$

It should be noted that the detection threshold is 11 MeV. Then, the  $\gamma$ -ray emission probability can be given as

$$R_{\gamma 0}(E_x) = \frac{(N_{\gamma 0} - N_{bg})/\bar{\eta}}{N_{E_x}}, \quad (4.18)$$

where  $N_{\gamma 0}$  is the number of  $\gamma$ -rays detected from excited  $^{12}\text{C}$  with  $E > 11$  MeV and  $\bar{\eta}$  is the averaged efficiency for the particular  $E_x$  range. Table 4.9 shows the number of direct  $\gamma$ -ray events ( $N_{\gamma 0}$ ), the number of background events ( $N_{bg}$ ), the number of excitation events ( $N_{E_x}$ ), efficiency ( $\bar{\eta}$ ) and the direct  $\gamma$ -ray emission probability ( $(R_{\gamma 0})$ ) with statistical and systematic uncertainties.

$E_x(\text{MeV})$	$N_{\gamma 0}$	$N_{bg}$	$N_{E_x}$	$\bar{\eta}$	$(R_{\gamma 0} \pm \text{stat.} \pm \text{sys.}) \times 10^{-2}$
16-20	2254	2140.3	3489210	0.027	$0.12 \pm 0.05 \pm 0.07$
20-23	3444	2984.2	5479123	0.032	$0.26 \pm 0.04 \pm 0.05$
23-26	3165	2634.3	4144857	0.035	$0.37 \pm 0.04 \pm 0.06$
26-29	3419	3061.5	2762530	0.037	$0.35 \pm 0.06 \pm 0.09$
29-32	6682	6204.8	3091624	0.040	$0.39 \pm 0.07 \pm 0.15$

Table 4.9  $\gamma$ -ray emission probability from the electromagnetic decay mode.

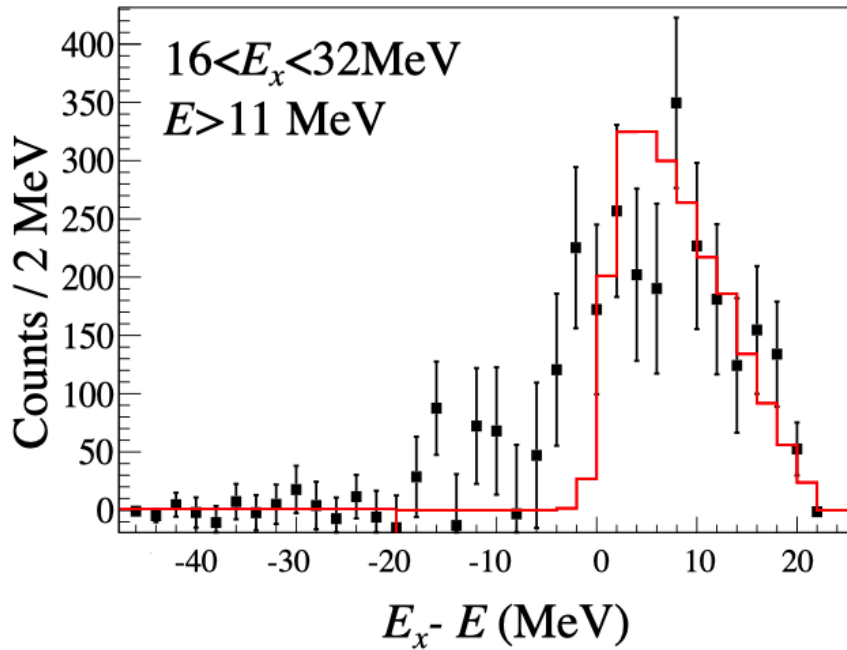


Fig. 4.11  $E_x - E$  spectrum (black) after background subtraction and scaled  $E_x - E$  response (red) simulated for the giant resonance energy region of  $^{12}\text{C}$  with  $E > 11$  MeV .

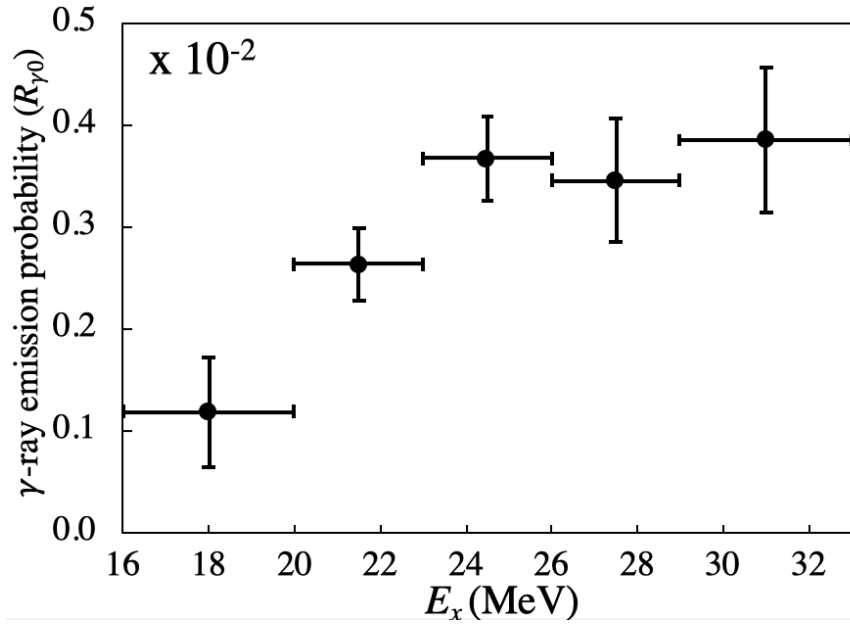


Fig. 4.12 Direct  $\gamma$ -ray emission probability from the giant resonances of  $^{12}\text{C}$ .

#### 4.2.4 $E1$ transition calculation

The measured direct  $\gamma$ -ray emission probability is also compared with  $E1$  transition calculations.

As previously mentioned in Eq. (1.29), the ground state  $\gamma$  decay width for a state at energy  $E$  decaying via  $E1$  transition can be given as

$$\Gamma_{\gamma 0} = \frac{16}{9(\hbar c)^2} E^3 B(E1). \quad (4.19)$$

The decay width can also be written in terms of total photo-nuclear cross section [15, 16] as

$$\frac{d\Gamma_{\gamma 0}}{dE} = \frac{16}{9(\hbar c)^2} E^3 \frac{dB(E1)}{dE}, \quad (4.20)$$

where

$$\frac{dB(E1)}{dE} \equiv b_{E1}(E) = \frac{9}{16\pi^3\alpha} \frac{\sigma_{PN}}{E} \quad \text{e}^2\text{fm}^2/\text{MeV} \quad (4.21)$$

Hence,

$$\frac{d\Gamma_{\gamma 0}}{dE} = \frac{E^2}{\pi^2(\hbar c)^2} \sigma_{PN}, \quad (4.22)$$

where  $\sigma_{PN}$  is taken from Ref. [17]. Figure 4.13 shows the comparison of the measured  $\gamma$ -ray emission probability with the calculations (scaled by factor 1.7). The calculations are in qualitative agreement with the data.

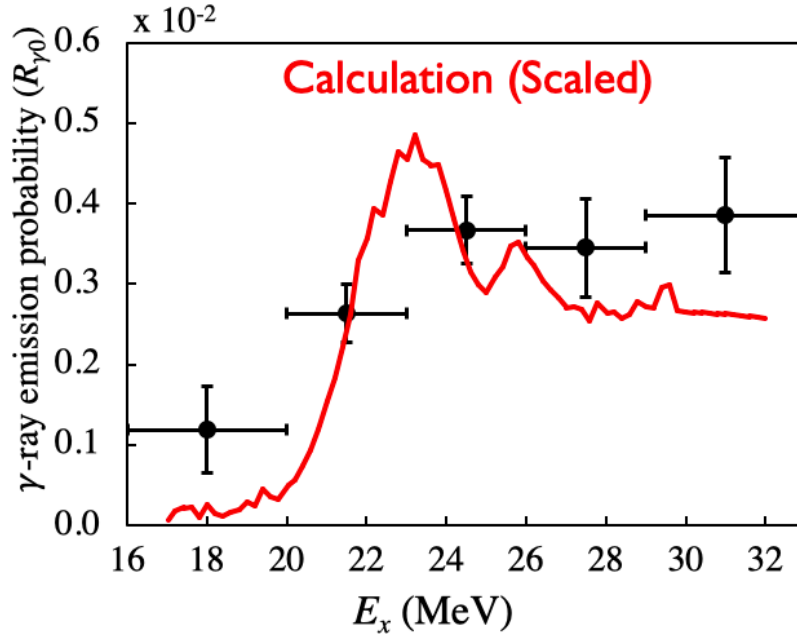


Fig. 4.13 Comparison with  $E1$  transition calculations (scaled).

Furthermore, the averaged  $\gamma$  decay width for the  $E1$  transition can be written as

$$R_{\gamma_0} \propto \Gamma_{\gamma_0} \propto \langle E_{GR} \rangle^2 \int_{GR} \sigma_{PN} dE, \quad (4.23)$$

where  $E$  (Mean energy of  $1^-$  giant resonance) and  $\int_{GR} \sigma_{PN} dE$  are described in Table 4.10.

	$E_{GR}$ (MeV)	$\int_{GR} \sigma_{PN} dE$ (mb MeV)
$^{12}\text{C}$	22.6	116 [17]
$^{208}\text{Pb}$	12.1	2646 [51]

Table 4.10 Mean energy of the  $1^-$  giant resonance and integrated total photo-nuclear cross section for  $^{12}\text{C}$  and  $^{208}\text{Pb}$ .

Figure 4.14 shows the comparison of averaged direct  $\gamma$ -ray emission probability measured from the giant resonances of  $^{12}\text{C}$  and  $^{208}\text{Pb}$  with the  $E1$  transition calculations (normalized with  $^{12}\text{C}$  data). The larger value of the direct  $\gamma$ -ray emission probability of  $^{208}\text{Pb}$  can be explained by  $E1$  transition calculations. As  $^{208}\text{Pb}$  has a larger photo-nuclear cross section (*i.e.* coupling to the photon) than  $^{12}\text{C}$ , the direct  $\gamma$ -ray emission probability is also larger (about 5 times).

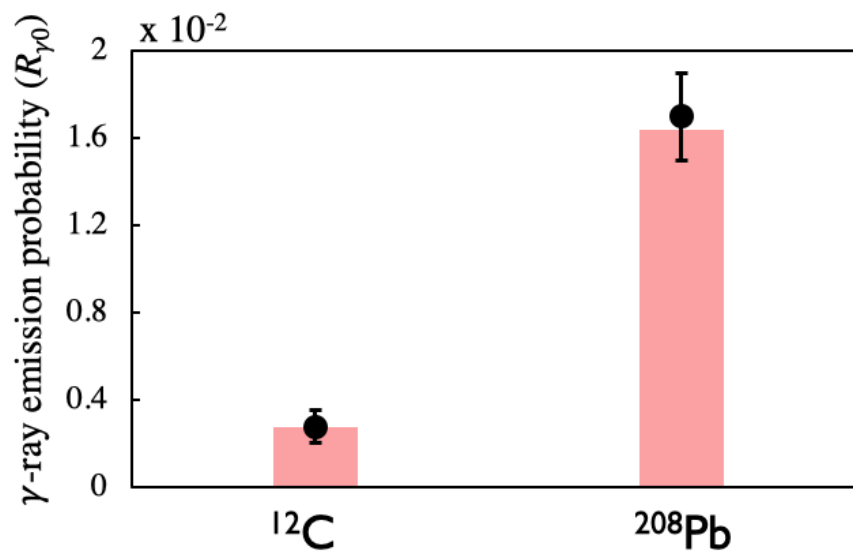


Fig. 4.14 Direct  $\gamma$ -ray emission probability from the giant resonances of  $^{12}\text{C}$  and  $^{208}\text{Pb}$  and comparison with  $E1$  transition calculations (normalized with  $^{12}\text{C}$ ).



# Chapter 5

## Estimation of supernova neutrinos

The expected number of events from a core-collapse supernova to be detected at large scale neutrino detectors can be given as

$$N = n_{tar.} \int_0^{E_v^{max}} dE_v \frac{d\Phi}{dE_v}(E_v) \left[ \int_{E_x} dE_x \frac{d\sigma(E_x, E_v)}{dE_x} \right] \quad (5.1)$$

where  $n_{tar.}$  is the appropriate number of targets,  $d\Phi/dE_v$  ( $\text{cm}^{-2}\text{MeV}^{-1}$ ) is the differential neutrino flux and  $d\sigma/dE_x$  ( $\text{cm}^2\text{MeV}^{-1}$ ) is the differential cross section. The number of targets,  $^{12}\text{C}$ , and protons in 1-kton liquid scintillator detector (KamLAND) are  $4.30 \times 10^{31}$  and  $8.60 \times 10^{31}$ , respectively [20].

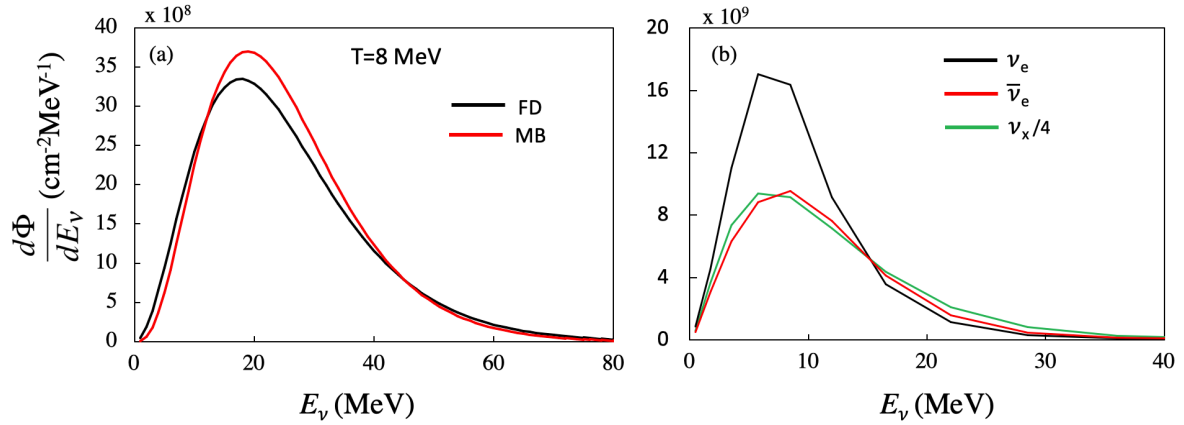


Fig. 5.1 (a) Supernova neutrino spectrum folded by Fermi-Dirac and Maxwell-Boltzmann distribution at  $T=8$  MeV. (b) Supernova neutrino spectrum obtained using Nakazato et. al. for different neutrino species.

## 5.1 Supernova Neutrino Spectra

For the estimation of supernova neutrino spectra, we first use the analytic expressions and then as the next step, we adopt numerical models. We assume that the total energy carried away by neutrinos during the core-collapse supernova is  $3 \times 10^{53}$  ergs and is equally divided between all the six flavors of neutrinos and anti-neutrinos. The time-integrated flux for the single neutrino flavor is given as

$$\frac{d\Phi}{dE_\nu} = \frac{1}{4\pi d^2} \frac{E_\nu^{tot}}{\langle E_\nu \rangle} f(E_\nu), \quad (5.2)$$

where  $E_\nu^{tot} = 0.5 \times 10^{53}$  is the total energy carried away by one flavor,  $\langle E_\nu \rangle$  is the average energy carried by a single neutrino and  $d$  is the distance to the supernova. The average energy is related to the equilibrium temperature ( $T$ ) of the neutrino by  $\langle E_\nu \rangle = 3.15 \times T$  [52]. The  $\nu_\mu$  and  $\nu_\tau$  neutrinos and their anti-neutrinos are collectively called  $\nu_x$  neutrinos and have an equilibrium temperature of 8 MeV (or  $\langle E_{\nu_x} \rangle \approx 25$  MeV). The  $\nu_e$  and  $\bar{\nu}_e$  leave with temperature 3.5 MeV (or  $\langle E_{\nu_e} \rangle \approx 11$  MeV) and 5 MeV (or  $\langle E_{\bar{\nu}_e} \rangle \approx 16$  MeV), respectively. The function  $f(E_\nu)$  is the energy distribution of supernova neutrinos and can be described using Maxwell-Boltzmann (MB) [21] form given as

$$f_{MB}(E_\nu) = 0.43 \frac{E_\nu^3}{T^4} \exp\left(-\frac{1.27E_\nu}{T}\right), \quad (5.3)$$

and Fermi-Dirac (FD) form

$$f_{FD}(E_\nu) = 0.55 \frac{E_\nu^2}{T^3} \frac{1}{1 + \exp(E_\nu/T)} \quad (5.4)$$

The comparison between supernova neutrino spectra using these two different forms at  $T=8$  MeV is shown in Fig. 5.1(a).

Supernova $\nu$ flux	$\langle E_{\nu_e} \rangle$ (MeV)	$\langle E_{\bar{\nu}_e} \rangle$ (MeV)	$\langle E_{\nu_x} \rangle$ (MeV)
F.D.	11.0	16.0	25.0
Nakazato	7.7	8.8	9.1

Table 5.1 Mean energies of the neutrinos from supernova explosion.

We also used supernova neutrino spectrum obtained from numerical models, which we took from the Supernova Neutrino Database [19]. In this database, several spectral models with different values of the progenitor mass ( $M$ ) and metallicity ( $Z$ ) are given, we adopt two sets:

1. NK1:  $(M, Z) = (20M_{\odot}, 0.02)$  and shock revival time = 200 ms
2. NK2:  $(M, Z) = (13M_{\odot}, 0.004)$  and shock revival time = 100 ms

The time-integrated neutrino spectra for different neutrino species obtained from the NK1 model are shown in Fig. 5.1(b).

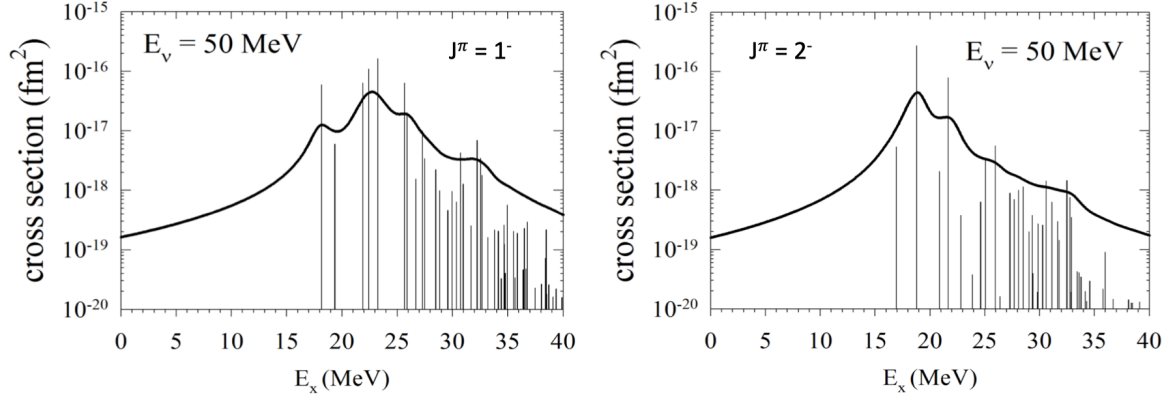


Fig. 5.2 The inelastic cross sections as a function of excitation energy at  $E_{\nu} = 50$  MeV for (a)  $^{12}\text{C}(\nu, \nu')^{12}\text{C}^*(1^-)$  reaction (b)  $^{12}\text{C}(\nu, \nu')^{12}\text{C}^*(2^-)$  reaction

## 5.2 Inelastic scattering cross section and events estimation

The NC 15.1 MeV events can be given as

$$N_{15.1}^{NC} = n_{tar.} \int_0^{E_{\nu}^{max}} dE_{\nu} \frac{d\Phi}{dE_{\nu}}(E_{\nu}) \sigma(E_x = 15.1 \text{ MeV}, E_{\nu}) \times 0.96. \quad (5.5)$$

NC inelastic cross sections for  $^{12}\text{C}$  as a function of excitation energy at different neutrino energies (Fig. 5.2) were obtained from shell model calculations based on the SFO-tls Hamiltonian [13]. The excitation energy range covered  $E_x = 15 - 40$  MeV. The cross section for the  $^{12}\text{C}(\nu, \nu')^{12}\text{C}^*(15.1 \text{ MeV}, 1^+, T = 1)$  reaction as a function of neutrino energy ( $E_{\nu}$ ) is also shown in Fig. 5.4. The excited  $^{12}\text{C}$  further decays by  $\gamma$ -ray emissions with 96% of  $\gamma$ -ray emission probability.

The NC signals from the decay of giant resonances of  $^{12}\text{C}$  can be given as

$$N_{\gamma}^{NC} = n_{tar.} \int_0^{E_{\nu}^{max}} dE_{\nu} \frac{d\Phi}{dE_{\nu}}(E_{\nu}) \left[ \int_{E_x=16 \text{ MeV}}^{E_x=32 \text{ MeV}} dE_x \frac{d\sigma(E_x, E_{\nu})}{dE_x} \times R_{\gamma}(E_x) \right], \quad (5.6)$$

where  $R_{\gamma}(E_x)$  is the measured  $\gamma$ -ray emission probability. The estimated events for KamLAND (1 kton) from the core-collapse supernova at 10 kpc are tabulated in Table 5.3. It

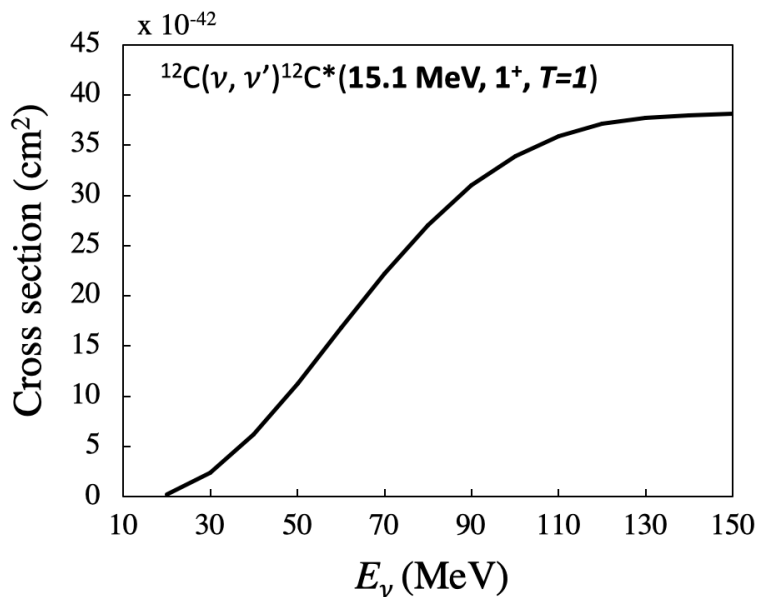


Fig. 5.3 The inelastic cross section for the  $^{12}\text{C}(\nu, \nu')^{12}\text{C}^*(15.1 \text{ MeV}, 1^+, T=1)$  reaction as function of neutrino energy ( $E_\nu$ ).

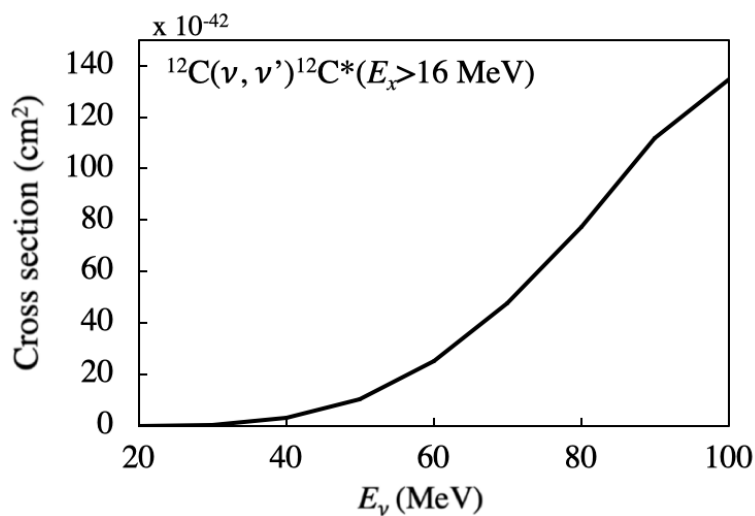


Fig. 5.4 The inelastic cross section for the  $^{12}\text{C}(\nu, \nu')^{12}\text{C}^*(E_x > 16 \text{ MeV})$  reaction as function of neutrino energy ( $E_\nu$ ).

should be noted that these numbers were calculated for the detector volume of 1kton. For future projects like JUNO (inner volume of 20 kton), RENO-50 (inner volume of 10 kton) etc., we would observe about twenty times greater NC signals.

Reaction	Present work				Previous work (FD) (KamLAND collab.)
	MB	FD	NK1	NK2	
$p(\bar{\nu}_e, e^+)n$	303	301	129	116	330
$^{12}\text{C}(\nu, \nu')^{12}\text{C}^*(15.1 \text{ MeV})$	45	47	15	14	58
$^{12}\text{C}(\nu, \nu')^{12}\text{C}^*(E_x > 16 \text{ MeV})$	7	9	1.1	1.2	-

Table 5.2 Expected number of neutrino events from a core-collapse supernova at 10 kpc to be detected at KamLAND (1kton).

Reaction	Present work				Laha <i>et al.</i> (MB) (JUNO collab.)
	MB	FD	NK1	NK2	
$p(\bar{\nu}_e, e^+)n$	4933	5378	2194	1974	4857
$^{12}\text{C}(\nu, \nu')^{12}\text{C}^*(15.1 \text{ MeV})$	382	426	169	161	398
$^{12}\text{C}(\nu, \nu')^{12}\text{C}^*(E_x > 16 \text{ MeV})$	144	180	21	20	-

Table 5.3 Expected number of neutrino events from a core-collapse supernova at 10 kpc to be detected at JUNO(20 kton).



# Chapter 6

## ANNRI Analysis

Although the main focus of this thesis is to study the decay of giant resonances, I also estimated the efficiency of the germanium spectrometer of the Accurate Neutron-Nucleus Reaction Measurement Instrument (ANNRI) at the Material and Life Science Experimental Facility (MLF) of the Japan Proton Accelerator Research Complex (J-PARC) at early stage of my Ph.D. The fourteen Ge detectors measure  $\gamma$  rays from the Gd target ( $\text{Gd}_2\text{O}_3$  powder), which is a scattered source. Hence, it was necessary to determine the effect of the target position on the efficiency of each detector. I studied this effect using the  $\gamma$  ray measurements taken with  $^{22}\text{Na}$  and  $^{60}\text{Co}$  at different target positions and optimized the corresponding parameters in our Monte Carlo. These contributions were fundamental for further analysis and building of the ANNRI-Gd model ( $\text{Gd}(n, \gamma)$  reaction). The results were published in the PTEP journal. The details of my contributions are described as follows.

### 6.1 Efficiency estimation

For radioactive sources that can emit more than one  $\gamma$  ray per decay ( $^{60}\text{Co}$ ,  $^{152}\text{Eu}$  and  $^{36}\text{Cl}$ ), a reduction of the photopeak efficiency due to the trigger/veto condition has to be taken into account: If one or more secondary  $\gamma$  rays are emitted along with the primary  $\gamma$  ray of energy  $E_\gamma$ , there is a chance that one of the secondary  $\gamma$  rays vetoes the primary  $\gamma$  ray hit by directly going into the BGO shield of the corresponding Ge cluster. This effectively reduces the photopeak efficiency compared to the case where solely the primary  $\gamma$  ray would be emitted.

The  $\gamma$  rays from the thermal  $^{35}\text{Cl}(n, \gamma)$  reaction do not allow the determination of absolute efficiency values since the number of emitted  $\gamma$  rays is unknown. Therefore, we computed efficiency values relative to the photopeak efficiency of the most intense line at 7414 keV among our selected lines. The normalization of the reference efficiency was obtained from our MC simulation.

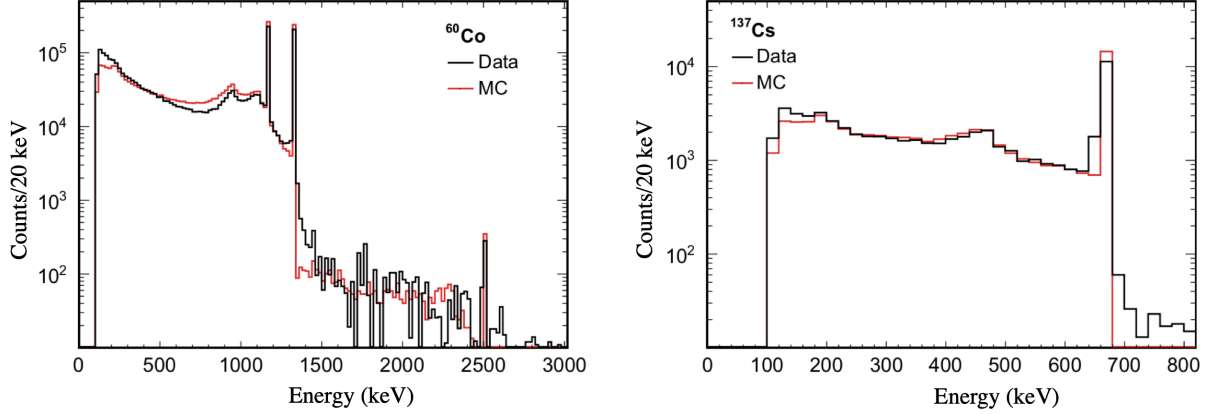


Fig. 6.1 Energy spectra observed by peripheral crystal 6 of the upper cluster in our data (black) and our MC (red) for the calibration sources  $^{60}\text{Co}$  (left) and  $^{137}\text{Cs}$  (right).

We corrected the single photopeak efficiency for this trigger effect differently for  $^{36}\text{Cl}$  /  $^{152}\text{Eu}$  and  $^{60}\text{Co}$ . From the complex decay and deexcitation schemes of  $^{36}\text{Cl}$  and  $^{152}\text{Eu}$  we only selected  $\gamma$  rays for the efficiency determination that are dominantly emitted alone or with just one additional  $\gamma$  ray in their particular decay channel: 5517 keV, 7414 keV, 7790 keV and 8579 keV for  $^{36}\text{Cl}$ ; 344 keV, 779 keV, 1112 keV and 1408 keV for  $^{152}\text{Eu}$ . Relevant branching ratios can be found in Ref. [53, 54]. This selection allowed for an easier estimation of the above described inefficiency in the two  $\gamma$ -ray cases by multiplying the raw photopeak efficiency value for a crystal with the correction

$$C_i = \frac{\varepsilon_i^{\text{MC}}(E_\gamma)}{\varepsilon_{i,2\gamma}^{\text{MC}}(E_\gamma; E_{\gamma 2})} \quad (6.1)$$

coming from our Geant4 MC simulation. It is calculated from the single photopeak MC efficiency  $\varepsilon_i^{\text{MC}}(E_\gamma)$  for the  $\gamma$  ray of interest with energy  $E_\gamma$  and the corresponding single photopeak MC efficiency  $\varepsilon_{i,2\gamma}^{\text{MC}}(E_\gamma; E_{\gamma 2})$  obtained when the second  $\gamma$  ray with  $E_{\gamma 2}$  is simultaneously propagated through the detector.

For the  $^{60}\text{Co}$  source, which essentially always emits two  $\gamma$  rays ( $E_1 = 1173$  keV and  $E_2 = 1332$  keV) [55], we determined the corrected single photopeak efficiency directly through a fit: We look at a pair of crystals ( $i, j$ ),  $i \neq j$ , where each crystal is on a separate cluster of ANNRI. The number of observed M1H1 events where  $E_k$  ( $k = 1, 2$ ) is deposited in crystal ( $i$ ) is  $N_{ik}$  with its error  $\sigma_{ik}$ . One expects this value to be  $\bar{N}_{ik} = \beta T r_{L,i} \varepsilon_{ik} (1 - C_i)$  with  $\varepsilon_{ik} \equiv \varepsilon_i(E_k)$ , the absolute elapsed time  $T$  and the dead time correction factor  $r_{L,i}$ . The efficiency correction  $(1 - C_i)$  is due to the inefficiency described above. For a given pair of crystals and the two  $\gamma$  rays this yields four combinations of crystal and  $\gamma$  ray. Moreover, we look at the coinciding

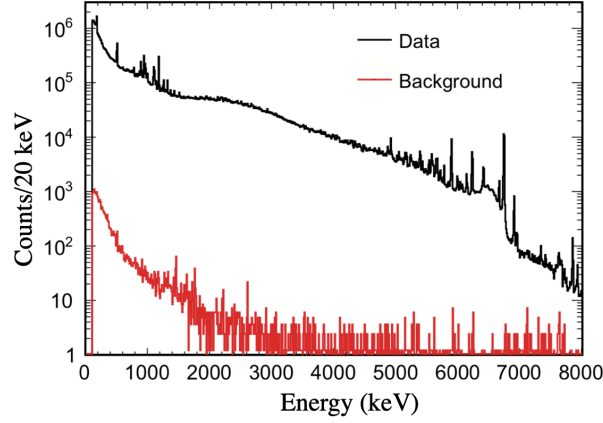


Fig. 6.2 Energy spectra observed by crystal 6 in the background measurement with an empty target holder (red) and the measurement with the enriched  $^{157}\text{Gd}$  sample (black; before background subtraction). The background spectrum was scaled to match the dead-time-corrected live time of the gadolinium measurement.

detection of both  $\gamma$  rays in M2H2 events by the crystals  $(i, j)$ . With  $E_l \neq E_k$  being the second  $\gamma$  ray, the observed number of coincidence events where  $E_k$  ( $E_l$ ) is detected in crystal  $i$  ( $j$ ) is  $N_{ikjl}$ . Its error is  $\sigma_{ikjl}$ . The expected value is  $\bar{N}_{ikjl} = \beta T r_{L,ij} \epsilon_{ik} \epsilon_{jl} W(\theta_{ij})$ . Here,  $r_{L,ij}$  is the dead time correction factor for the crystal pair  $(i, j)$ , which typically is on the order of 90%. The factor  $W(\theta_{ij})$  accounts for the predicted angular correlation [56] of the  $\gamma$  rays from  $^{60}\text{Co}$  with angle  $\theta_{ij}$ , which is given by the angle of the detector pair  $(i, j)$ . A second combination,  $N_{iljk}$ , simply follows from permuting the  $\gamma$  ray energies. With the in total six observables we minimized the expression

$$\chi_{ij}^2 = \left( \frac{N_{ik} - \bar{N}_{ik}}{\sigma_{ik}} \right)^2 + \left( \frac{N_{il} - \bar{N}_{il}}{\sigma_{il}} \right)^2 + \left( \frac{N_{jk} - \bar{N}_{jk}}{\sigma_{jk}} \right)^2 + \left( \frac{N_{jl} - \bar{N}_{jl}}{\sigma_{jl}} \right)^2 + \left( \frac{N_{ikjl} - \bar{N}_{ikjl}}{\sigma_{ikjl}} \right)^2 + \left( \frac{N_{iljk} - \bar{N}_{iljk}}{\sigma_{iljk}} \right)^2 \quad (6.2)$$

for 48 crystal pairs  $(i, j)$ , one was excluded, to fit the four uncorrected single photopeak efficiencies,  $\epsilon_{ik}$ ,  $\epsilon_{il}$ ,  $\epsilon_{jk}$  and  $\epsilon_{jl}$ , and  $\beta T$  for different but fixed values of the constant  $C$ . The best agreement between the mean of the fitted values of  $\beta T$  and the nominal value was obtained for  $C = 0.225$ . Using this constant, we took the averages of the efficiency values per crystal and energy as final results. With this method, we obtained a single photopeak efficiency of  $(1.3 \pm 0.1)\%$  at 1.3 MeV for all 14 Ge crystals combined.

Fig. 6.3 depicts the ratios of the single photopeak efficiencies from data and from MC at the single  $\gamma$  ray energies averaged over all 14 crystals (left) and for all 14 crystals averaged

over the 11 data points (right). On both plots, one can see that the weighted mean values of the ratios deviate by less than 10% from the perfect agreement and maximum deviations are about 20%. The weighted sample standard deviation of the ratios for all crystals and data points is about 6%. From this study, we conclude that we understand the photopeak efficiency of each crystal not only over the energy range from 344 keV to 8579 keV but also uniformly over the entire solid angle of the detector and that we can reproduce the response of each crystal very well by our Geant4 detector simulation.

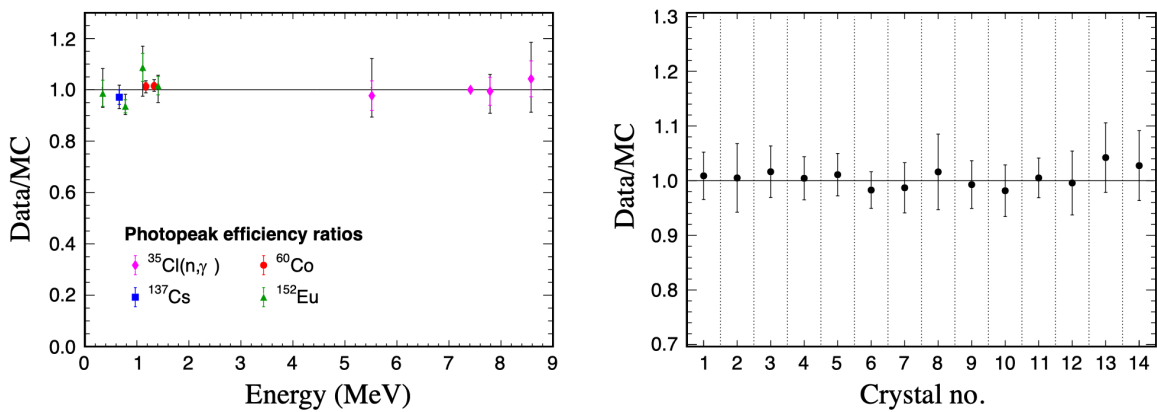


Fig. 6.3 Ratios of the single photopeak efficiencies from data to single photopeak efficiencies from MC averaged over the 14 crystals at the fixed  $\gamma$ -ray energies (left) and averaged over the 11 data points for the single crystals (right). Linear interpolation between the points from the simulation was used to determine the MC efficiency at intermediate energy. The calculations of the weighted mean values and the weighted sample standard deviations (error bars) take the errors of the data points into account. Outer error bars indicate the extreme values of the ratios in the respective samples. The  $^{35}\text{Cl}(n,\gamma)$  data point at 7414 keV is the reference for the normalization of the other data points of this reaction. It perfectly agrees with a ratio of one since it was normalized with the MC simulation.

# Chapter 7

## Summary and Conclusion

The complete understanding of the decay mechanism of the giant resonances can be achieved by measuring the  $\gamma$  rays from their decay. The decays emitting  $\gamma$  rays with energy  $E_\gamma < 11$  MeV correspond to hadronic decays and the decays emitting  $\gamma$  rays with energy  $16 < E_\gamma < 32$  MeV correspond to electromagnetic decays. An experiment (E398) to measure these  $\gamma$  rays from the giant resonances of  $^{12}\text{C}$  was carried out at RCNP (Osaka University) with the following objectives.

1. Excitation of  $^{12}\text{C}$  to its giant resonances using a proton beam.
2. Measurement  $\gamma$  rays from hadronic decays ( $E_\gamma < 11$  MeV) and as well as electromagnetic decays ( $16 < E_\gamma < 32$  MeV).
3. Study of the hadronic and electromagnetic decay mechanisms of the giant resonances.
4. Comparison of measurements with statistical model calculation.
5. Estimation of NC events at large scale scintillator-based detectors from core-collapse supernova using our measurements.

We measured the double differential cross section ( $\sigma_{p,p'} \equiv d^2\sigma/dE_x d\Omega$ ) for the  $^{12}\text{C}(p,p')$  inelastic reaction at 392 MeV and  $0^\circ$  for the energy range  $E_x = 7-32$  MeV. Furthermore, the cross section was decomposed into spin-flip ( $\Delta S = 1$ ) and non-spin-flip components ( $\Delta S = 0$ ) using polarization transfer (PT) observables measured previously at the same beam energy [2]. The spin-flip cross section was observed to be dominated by isovector resonances and the non-spin-flip cross section was dominated by  $1^-$  resonances and agreed well with recent calculations of Coulomb excitations [40]. The differential cross sections ( $d\sigma/d\Omega$ ) as a function of scattering angle was also measured for various  $E_x$  regions. The observed angular distributions were consistent with DWBA calculations.

For the measurements of  $\gamma$  rays from the giant resonances, the absolute values of the  $\gamma$ -ray emission probability ( $R_\gamma(E_x)$ ) and the response functions were verified using in-situ  $\gamma$  rays (15.1 and 6.9 MeV) with an accuracy of  $\pm 5\%$  during the experiment. This calibration procedure made it possible to measure the  $\gamma$ -ray emission probability ( $R_\gamma(E_x)$ ) reliably as a function of the excitation energy of  $^{12}\text{C}$  in the energy range  $E_x = 16\text{-}32$  MeV. For the high energy  $\gamma$ -ray analysis, the pulse height linearity and the resolution of the  $\gamma$ -ray detector were checked up to 33.3 MeV.

The study of the decay of giant resonances in  $^{12}\text{C}$  by  $(p, p'\gamma)$  reaction is concluded as follows:

1. The  $\gamma$ -ray energy spectra and  $\gamma$ -ray emission probability ( $R_\gamma(E_x) = \sigma_{p, p'\gamma} / \sigma_{p, p'}$ ) was measured for the first time as a function of excitation energy for the energy range  $E_x = 16\text{-}32$  MeV.
2. The  $\gamma$ -ray spectra ( $E_\gamma < 11$  MeV) clearly show that the  $\gamma$  rays are emitted from the excited states of daughter nuclei after the particle emission. This is the first observation of  $\gamma$  rays from the hadronic decays of giant resonances in  $^{12}\text{C}$ .
3. The overall features of the  $\gamma$ -ray spectra agreed qualitatively with a theoretical prediction based on the hadronic decays of giant resonances [24].
4. It was found that the measured value of ( $R_\gamma(E_x)$ ) for hadronic decay mode starts from zero at  $E_x = 16$  MeV (the threshold for  $p + ^{11}\text{B}$  decay) and increases to  $47.9 \pm 0.5 \pm 3.5\%$  at  $E_x = 27$  MeV and then decreases.
5. The measurements were also compared with the statistical model calculation and smaller  $\gamma$ -ray emission probability by 30-40% was observed than predicted by the calculation.
6. From electromagnetic decay mode ( $16 < E_\gamma < 32$  MeV),  $R_\gamma(E_x)$  increases with excitation energy and reaches the maximum value of  $(0.37 \pm 0.04 \pm 0.04) \times 10^{-2}$  at  $E_x = 24$  MeV. This is the first measurement of  $\gamma$ -ray emission probability from the electromagnetic decays of the giant resonances in  $^{12}\text{C}$ .
7. The trend observed can be explained by  $E1$  transition calculation done using photo-nuclear absorption cross section of  $^{12}\text{C}$ .
8. The  $\gamma$ -ray emission probability was also measured as a function of scattering angle, but no strong angular dependence was observed.

9. Using the measured value of  $(R_\gamma(E_x))$ , the expected number of NC events at large-scale scintillator-based detectors (e.g. KamLAND and JUNO) from the core-collapse supernova were also calculated.

The present results are very important for understanding the  $\gamma$ -ray emission probability of the giant resonances of a typical light nucleus ( $^{12}\text{C}$ ) and for the neutrino detection in liquid scintillator detectors through neutral-current interactions. A similar analysis of the  $^{16}\text{O}(p,p')$  reaction is also ongoing. An experiment using a Germanium detector such as that of the CAGRA spectrometer at RCNP [39] will significantly improve the current understanding of the  $\gamma$ -ray emission and decay of giant resonances by separating  $\gamma$  rays emitted from the daughter nuclei after proton and neutron decays.



# References

- [1] M. Fujiwara, H. Akimune, I. Daito, H. Fujimura, Y. Fujita, K. Hatanaka, H. Ikegami, I. Katayama, K. Nagayama, N. Matsuoka, S. Morinobu, T. Noro, M. Yoshimura, H. Sakaguchi, Y. Sakemi, A. Tamii, and M. Yosoi. Magnetic spectrometer grand raiden. *Nuclear Instruments and Methods in Physics Research Section A: Accelerators, Spectrometers, Detectors and Associated Equipment*, 422(1):484 – 488, 1999.
- [2] A. Tamii, H. Akimune, I. Daito, Y. Fujita, M. Fujiwara, K. Hatanaka, K. Hosono, F. Ihara, T. Inomata, T. Ishikawa, M. Itoh, M. Kawabata, T. Kawabata, M. Nakamura, T. Noro, E. Obayashi, H. Sakaguchi, H. Takeda, T. Taki, H. Toyokawa, H.P. Yoshida, M. Yoshimura, and M. Yosoi. Polarization transfer observables for proton inelastic scattering from  $^{12}\text{C}$  at  $0^\circ$ . *Physics Letters B*, 459(1):61 – 66, 1999.
- [3] T. Kawabata, T. Ishikawa, M. Itoh, M. Nakamura, H. Sakaguchi, H. Takeda, T. Taki, M. Uchida, Y. Yasuda, M. Yosoi, H. Akimune, K. Yamasaki, G. P. A. Berg, H. Fujimura, K. Hara, K. Hatanaka, J. Kamiya, T. Noro, E. Obayashi, T. Wakasa, H. P. Yoshida, B. A. Brown, H. Fujita, Y. Fujita, Y. Shimbara, H. Ueno, M. Fujiwara, K. Hosono, A. Tamii, and H. Toyokawa. Polarization transfer in the  $^{16}\text{O}(p, p')$  reaction at forward angles and structure of the spin-dipole resonances. *Phys. Rev. C*, 65:064316, Jun 2002.
- [4] M. Dozono, T. Wakasa, E. Ihara, S. Asaji, K. Fujita, K. Hatanaka, T. Ishida, T. Kaneda, H. Matsubara, Y. Nagasue, T. Noro, Y. Sakemi, Y. Shimizu, H. Takeda, Y. Tameshige, A. Tamii, and Y. Yamada. Complete set of polarization transfer observables for the  $^{12}\text{C}(p, n)$  reaction at 296 MeV and  $0^\circ$ . *J. Phys. Soc. Jpn.*, 77:014201, jan 2008.
- [5] M. A. Franey and W. G. Love. Nucleon-nucleon t-matrix interaction for scattering at intermediate energies. *Phys. Rev. C*, 31:488–498, Feb 1985.
- [6] F. Petrovich and W.G. Love. The scattering of elementary probes from nuclei at medium energy: A new look at the nucleus. *Nuclear Physics A*, 354(1):499 – 534, 1981.

- [7] J.H. Kelley, J.E. Purcell, and C.G. Sheu. Energy levels of light nuclei  $A = 12$ . *Nuclear Physics A*, 968:71 – 253, 2017.
- [8] K. W. Jones, C. Glashausser, R. de Swiniarski, F. T. Baker, T. A. Carey, J. R. Comfort, W. Cornelius, J. L. Escudié, M. Gazzaly, A. Green, M. Haji-Saeid, N. Hintz, G. Igo, J. B. McClelland, J. M. Moss, S. Nanda, and C. A. Whitten. Energy dependence of the  $^{12}\text{C}(p, p')^{12}\text{C}^*$  reaction from 200 to 800 MeV. *Phys. Rev. C*, 50:1982–1990, Oct 1994.
- [9] G. J. F. Legge and I. F. Bubb. *Nucl. Phys*, 26:626, 1961.
- [10] J. K. Bair, C. M. Jones, and H. B. Willard. *Nucl. Phys*, 53:209, 1964.
- [11] B. N. Johnson, M. Morlet, C. Djalali, F. T. Baker, L. Bimbot, C. Glashausser, J. Guillot, H. Langevin-Joliot, N. Marty, L. Rosier, E. Tomasi-Gustafsson, J. Van de Wiele, and A. Willis. Isoscalar spin strength in  $^{12}\text{C}$  measured in 400 MeV deuteron inelastic scattering. *Phys. Rev. C*, 51:1726–1735, Apr 1995.
- [12] T. Suzuki. Spin modes in nuclei and astrophysical processes based on new shell-model hamiltonians. *Journal of Physics: Conference Series*, 321(1):012041, 2011.
- [13] T. Yoshida, T. Suzuki, S. Chiba, T. Kajino, H. Yokomakura, K. Kimura, A. Takamura, and D. H. Hartmann. Neutrino-nucleus reaction cross sections for light element synthesis in supernova explosions. *The Astrophysical Journal*, 686(1):448, 2008.
- [14] A. Bohr and B.R. Mottelson. *Nuclear Structure I*. W.A. Benjamin, Inc., Reading, MA, 1975.
- [15] J. R. Beene, F. E. Bertrand, M. L. Halbert, R. L. Auble, D. C. Hensley, D. J. Horen, R. L. Robinson, R. O. Sayer, and T. P. Sjoreen. Heavy-ion excitation and photon decay of giant resonances in  $^{208}\text{Pb}$ . *Phys. Rev. C*, 39:1307–1319, Apr 1989.
- [16] J. R. Beene, F. E. Bertrand, D. J. Horen, R. L. Auble, B. L. Burks, J. Gomez del Campo, M. L. Halbert, R. O. Sayer, W. Mittig, Y. Schutz, J. Barrette, N. Alamanos, F. Auger, B. Fernandez, A. Gillibert, B. Haas, and J. P. Vivien. Heavy-ion coulomb excitation and photon decay of the giant dipole resonance in  $^{208}\text{Pb}$ . *Phys. Rev. C*, 41:920–932, Mar 1990.
- [17] E. G. Fuller. Photonuclear reaction cross sections for  $^{12}\text{C}$ ,  $^{14}\text{N}$  and  $^{16}\text{O}$ . *Phys. Rep.*, 127:185–231, October 1985.
- [18] M. Fukugita and A. Suzuki. *Physics and Astrophysics of Neutrinos*. Springer-Verlag Tokyo, 1994.

- [19] K. Nakazato, K. Sumiyoshi, H. Suzuki, T. Totani, H. Umeda, and S. Yamada. Supernova neutrino light curves and spectra for various progenitor stars: From core collapse to proto-neutron star cooling. *The Astrophysical Journal Supplement Series*, 205(1):2, 2013.
- [20] S. Abe, K. Furuno, A. Gando, Y. Gando, K. Ichimura, H. Ikeda, K. Inoue, Y. Kibe, W. Kimura, Y. Kishimoto, M. Koga, Y. Minekawa, T. Mitsui, T. Morikawa, N. Nagai, K. Nakajima, K. Nakamura, M. Nakamura, K. Narita, I. Shimizu, Y. Shimizu, J. Shirai, F. Suekane, A. Suzuki, H. Takahashi, N. Takahashi, Y. Takemoto, K. Tamae, H. Watanabe, B. D. Xu, H. Yabumoto, E. Yonezawa, H. Yoshida, S. Yoshida, S. Enomoto, A. Kozlov, H. Murayama, C. Grant, G. Keefer, D. McKee, A. Piepke, T. I. Banks, T. Bloxham, J. A. Detwiler, S. J. Freedman, B. K. Fujikawa, K. Han, R. Kadel, T. O'Donnell, H. M. Steiner, L. A. Winslow, D. A. Dwyer, C. Auger, R. D. McKeown, C. Zhang, B. E. Berger, C. E. Lane, J. Maricic, T. Miletic, M. Batygov, J. G. Learned, S. Matsuno, S. Pakvasa, M. Sakai, G. A. Horton-Smith, A. Tang, K. E. Downum, G. Gratta, K. Tolich, Y. Efremenko, Y. Kamyshev, O. Perevozchikov, H. J. Karwowski, D. M. Markoff, W. Tornow, K. M. Heeger, F. Piquemal, J. S. Ricol, and M.P. Decowski. Measurement of the  $^8\text{B}$  solar neutrino flux with the KamLAND liquid scintillator detector. *Phys. Rev. C*, 84:035804, Sep 2011.
- [21] Beacom J. F. Laha, R. and S.K.. Agarwalla. Mass signature of supernova  $\nu_\mu$  and  $\nu_\tau$  neutrinos in superkamiokande. *arXiv:1412.8425 [hep-ph]*.
- [22] B. Bodmann, N.E. Booth, F. Burtak, A. Dodd, G. Drexlin, V. Eberhard, J.A. Edgington, E. Finckh, H. Gemmeke, G. Giorginis, A. Glombik, T. Gorringer, W. Grandegger, T. Hanika, M. Kleifges, J. Kleinfeller, W. Kretschmer, A. Malik, R. Maschuw, R. Meyer, P. Plischke, F. Raupp, F. Schilling, B. Seligmann, J. Wochele, J. Wolf, S. Wölfle, and B. Zeitnitz. First observation of the neutral current nuclear excitation  $^{12}\text{C}(\nu, \nu')^{12}\text{C}^*(1^+, 1)$ . *Physics Letters B*, 267(3):321 – 324, 1991.
- [23] C. M. Baglin R. B. Firestone and S. Y. F. Chu. Table of isotopes, 8th ed. *Wiley, New York*, 1999.
- [24] K. Langanke, P. Vogel, and E. Kolbe. *Phys. Rev. Lett.*, 76:2629–2632, Apr 1996.
- [25] H. Feshbach. *Theoretical Nuclear Physics- Nuclear reactions*. John Wiley and Sons, Inc., 1991.

- [26] T. Rauscher, F.-K. Thielemann, and K.-L. Kratz. Nuclear level density and the determination of thermonuclear rates for astrophysics. *Phys. Rev. C*, 56:1613–1625, Sep 1997.
- [27] F. Pühlhofer. On the interpretation of evaporation residue mass distributions in heavy-ion induced fusion reactions. *Nuclear Physics A*, 280(1):267 – 284, 1977.
- [28] J. Rapaport, V. Kulkarni, and R. W. Finlay. A global optical-model analysis of neutron elastic scattering data. *Nucl. Phys.*, A330:15–28, 1979.
- [29] F. D. Becchetti and G. W. Greenlees. Nucleon-nucleus optical-model parameters,  $A > 40$ ,  $E < 50$  MeV. *Phys. Rev.*, 182:1190–1209, Jun 1969.
- [30] G.R. Satchler. Analysis of the scattering of 28 MeV alpha particles. *Nuclear Physics*, 70(1):177 – 195, 1965.
- [31] G. Perrin, Nguyen Van Sen, J. Arvieux, R. Darves-Blanc, J. L. Durand, A. Fiore, J. C. Gondrand, F. Merchez, and C. Perrin. A systematic study of elastic scattering of polarized deuterons around 30 MeV by complex nuclei. *Nucl. Phys.*, A282:221–242, 1977.
- [32] K.H.N Murthy, S.K. Gupta, and A Chatterjee. Transmission coefficients for light particles. *Z Phys. A*, 305:73 – 79, 1982.
- [33] S. M. Grimes, J. D. Anderson, A. K. Kerman, and C. Wong. Role of isospin in statistical processes. *Phys. Rev. C*, 5:85–94, Jan 1972.
- [34] M.N. Harakeh, D.H. Dowell, G. Feldman, E.F. Garman, R. Loveman, J.L. Osborne, and K.A. Snover. Role of isospin in the statistical decay of the giant dipole resonance built on excited states. *Physics Letters B*, 176(3):297 – 301, 1986.
- [35] P. Ludwig, R. Geller, and G. Melin. The 10 GHz neomafios upgraded electron cyclotron resonance ion source. *Review of Scientific Instruments*, 63(4):2892–2893, 1992.
- [36] A. Tamii, H. Akimune, I. Daito, Y. Fujita, M. Fujiwara, K. Hatanaka, K. Hosono, F. Ihara, T. Inomata, T. Ishikawa, M. Itoh, M. Kawabata, T. Kawabata, M. Nakamura, T. Noro, E. Obayashi, H. Sakaguchi, H. Takeda, T. Taki, H. Toyokawa, H.P. Yoshida, M. Yoshimura, and M. Yosoi. Polarization transfer observables for proton inelastic scattering from  $^{12}\text{C}$  at  $0^\circ$ . *Physics Letters B*, 459(1):61 – 66, 1999.
- [37] A. Tamii et al. *IEEE Trans. Nucl. Sci.*, 43:2488, 1996.

- [38] B. D. Anderson, L. A. C. Garcia, D. J. Millener, D. M. Manley, A. R. Baldwin, A. Fazely, R. Madey, N. Tamimi, J. W. Watson, and C. C. Foster.  $^{12}\text{C}(p,n)^{12}\text{N}$  reaction at 135 MeV. *Phys. Rev. C*, 54:237–253, Jul 1996.
- [39] C. Sullivan, R. G. T. Zegers, S. Noji, Sam M. Austin, J. Schmitt, N. Aoi, D. Bazin, M. Carpenter, J. J. Carroll, H. Fujita, U. Garg, G. Gey, C. J. Guess, T. H. Hoang, M. N. Harakeh, E. Hudson, N. Ichige, E. Ideguchi, A. Inoue, J. Isaak, C. Iwamoto, C. Kacir, T. Koike, N. Kobayashi, S. Lipschutz, M. Liu, P. von Neumann-Cosel, H. J. Ong, J. Pereira, M. Kumar Raju, A. Tamii, R. Titus, V. Werner, Y. Yamamoto, Y. D. Fang, J. C. Zamora, S. Zhu, and X. Zhou. The ( $^6\text{Li}, ^6\text{Li}^*[3.56\text{ MeV}]$ ) reaction at 100 MeV/u as a probe of gamow-teller transition strengths in the inelastic scattering channel. *Phys. Rev. C*, 98:015804, Jul 2018.
- [40] C.A. Bertulani and A.M. Nathan. Excitation and photon decay of giant resonances from high-energy collisions of heavy ions. *Nuclear Physics A*, 554(1):158 – 172, 1993.
- [41] T. Ishikawa and et al. Study of giant monopole resonance in  $^{58}\text{Ni}$  via the ( $p, p'$ ) reaction at  $0^\circ$ . *Nucl. Phys.*, A687:58–63, 2001.
- [42] M. Itoh, H. Akimune, M. Fujiwara, U. Garg, H. Hashimoto, T. Kawabata, K. Kawase, S. Kishi, T. Murakami, K. Nakanishi, Y. Nakatsugawa, B.K. Nayak, S. Okumura, H. Sakaguchi, H. Takeda, S. Terashima, M. Uchida, Y. Yasuda, M. Yosoi, and J. Zenihiro. Study of the cluster state at  $ex = 10.3\text{ MeV}$  in  $^{12}\text{C}$ . *Nuclear Physics A*, 738:268 – 272, 2004. Proceedings of the 8th International Conference on Clustering Aspects of Nuclear Structure and Dynamics.
- [43] A. Kiss, C. Mayer-Borricke, M. Rogge, P. Turek, and S. Wiktor. Inelastic scattering of 172.5 MeV  $\alpha$  particles by  $^{12}\text{C}$ . *Journal of Physics G: Nuclear Physics*, 13(8):1067, 1987.
- [44] A. Erell, J. Alster, J. Lichtenstadt, M. A. Moinester, J. D. Bowman, M. D. Cooper, F. Irom, H. S. Matis, E. Piassetzky, and U. Sennhauser. Measurements on isovector giant resonances in pion charge exchange. *Phys. Rev. C*, 34:1822–1844, Nov 1986.
- [45] J. Raynal. *Progma code "DWBA07"*, NEA-1209/08.
- [46] J. B. Flanz, R. S. Hicks, R. A. Lindgren, G. A. Peterson, A. Hotta, B. Parker, and R. C. York. Convection currents and spin magnetization in  $E2$  transitions of  $^{12}\text{C}$ . *Phys. Rev. Lett.*, 41:1642–1645, Dec 1978.

- [47] J. R. Comfort and B. C. Karp. Scattering and reaction dynamics for the  $^{12}\text{C}+p$  system. *Phys. Rev. C*, 21:2162–2176, Jun 1980.
- [48] L. Lapikás, G. van der Steenhoven, L. Frankfurt, M. Strikman, and M. Zhalov. Transparency of  $^{12}\text{C}$  for protons. *Phys. Rev. C*, 61:064325, May 2000.
- [49] G. Van Der Steenhoven, H.P. Blok, E. Jans, M. De Jong, L. Lapikás, E.N.M. Quint, and P.K.A. De Witt Huberts. Knockout of 1p protons from  $^{12}\text{C}$  induced by the  $(e, e'p)$  reaction. *Nuclear Physics A*, 480(3):547 – 572, 1988.
- [50] T. Inomata, H. Akimune, I. Daito, H. Ejiri, H. Fujimura, Y. Fujita, M. Fujiwara, M. N. Harakeh, K. Ishibashi, H. Kohri, N. Matsuoka, S. Nakayama, A. Tamii, M. Tanaka, H. Toyokawa, M. Yoshimura, and M. Yosoi. Particle decays from  $^{12}\text{B}$  and  $^{12}\text{N}$  mirror nuclei. *Phys. Rev. C*, 57:3153–3166, Jun 1998.
- [51] B. L. Berman and S. C. Fultz. Measurements of the giant dipole resonance with monoenergetic photons. *Rev. Mod. Phys.*, 47:713–761, Jul 1975.
- [52] J. F. Beacom and P. Vogel. Mass signature of supernova  $\nu_\mu$  and  $\nu_\tau$  neutrinos in superkamiokande. *Phys. Rev. D*, 58:053010, Aug 1998.
- [53] J. Cameron, J. Chen, B. Singh, and N. Nica. Nuclear Data Sheets for  $A = 37$ . *Nucl. Data Sheets*, 113(2):365–514, 2012.
- [54] M.J. Martin. Nuclear Data Sheets for  $A = 152$ . *Nucl. Data Sheets*, 114(11):1497–1847, 2013.
- [55] E. Browne and J.K. Tuli. Nuclear Data Sheets for  $A = 60$ . *Nucl. Data Sheets*, 114(12):1849–2022, 2013.
- [56] J.T. Larsen, W.C. Schick, W.L. Talbert, and D.I. Haddad. A seven-detector system for  $\gamma$ - $\gamma$  angular correlations. *Nucl. Instrum. Meth.*, 69(2):229–239, 1969.

## **Acknowledgements**

First of all, I would like to thank my supervisor, Prof. Makoto Sakuda, for the patient guidance, encouragement and advice he has provided throughout my time as his student. I have been privileged to have a supervisor who cared a lot about my work, and who responded to my questions and queries so promptly. I would also like to thank Dr. A. Tamii (RCNP) for his constructive suggestions and continuous support in my research work.

I would also like to show my gratitude towards my co-supervisors, Dr. H. Ishino and Y. Koshio for their valuable suggestions. I would like to offer special thanks to Dr. Rohit Dhir for helping me in pursuing the doctor course at Okayama University and in adjusting to the foreign lifestyle.

I also owe a great amount of gratitude to Mr. T. Sudo, my colleague and friend, for his huge contribution in analysis. I am also thankful to Dr. I. Ou for his huge contribution in spectrometer analysis. I would also like to thank my other colleagues especially Dr. Pretam Das, Dr. A. Ali and Mr. K. Hagiwara for making my research life more joyful and interesting.

This work was supported by JSPS Grant-in-Aid for Scientific Research on Innovative Areas (Research in a proposed research area) No. 26104006.

Finally, I would like to thank my family for their unconditional support, love and encouragement, without which I would not have come this far.

